Ternary $XInS_2$ Nanocrystals for Optoelectronics

Inji Yeom
St Edmund Hall

A thesis submitted in fulfilment of requirement for the degree of
DPhil in Materials at the **University of Oxford**

Abstract

The primary focus of this thesis is to develop new synthesis routes for core-shell copper indium di-sulphide ($CuInS_2$)–zinc sulphide (ZnS), and core-only silver indium di-sulphide ($AgInS_2$) nanocrystals with enhanced photoluminescence quantum yield (PLQY) and study their application in luminescent concentrators.

$CuInS_2$-ZnS nanocrystal photoluminescence (PL) properties were investigated using different synthesis conditions. Through a combination of PL, absorption (Abs), and transmission electron microscopy (TEM), the importance of relative stoichiometry between the two cations (copper and indium) are understood. To further study this effect, different injection temperatures and precursor ratios were employed. It was determined that with increasing indium (In) content, the PL blue shifted while increased PLQY was noted. Optimal synthesis conditions for monodispersed nanocrystals was found to be at an injection temperature of 30°C with a 1:4 Cu:In ratio, which achieved a PLQY of 40%. By using various halide precursor combinations of fluoride, chloride, bromide, and iodide, 16 combinations were evaluated in the control of the reactivity of the two cation precursors. Overall, this study demonstrated that the reactivity of Cu and In can be regulated to a certain extent. Additionally, the halide precursor counter ions potentially provided surface passivation, which enhanced PLQY by up to 60%.

The synthesis method established was repeated with replacement of the easily oxidised Cu with more stable Ag to form $AgInS_2$ nanocrystals. It was shown that by-products of Ag and Ag_2S nanocrystals were observed, which reduced the overall PLQY. With *in-situ* PL, synthesis dynamics were examined. Ag_2S nanocrystals were formed from the Ag nanocrystals formed prior to sulfur injection. Through changes in reduction temperature

and halide precursor combinations, the by-product quantity was reduced and a high PLQY of 89% was achieved.

Using $AgInS_2$, the first ternary nanocrystal luminescent concentrator for visible light communication (VLC) was fabricated. Modifying the polymer and nanocrystal concentrations resulted in changes in transmittance and reflectance properties. It was determined that the best combination used was ethyl cellulose 8wt% with 9mg/ml $AgInS_2$ (AIS) nanocrystals. With the addition of a mirror and a low refractive polymer layer, the gain, when compared to a single photodiode (PD), was seven times higher.

Acknowledgements

I would like to thank both my supervisor Professor Andrew Watt and Professor Hazel Assender for being a wonderful supporter throughout 4 years of my DPhil. During my second year when I decided to change my topic to a completely new field, come to think of it now, it was a tremendous challenge. Without your guidance and support I wouldn't be where I am now. I will miss our weekly meetings and discussions. Thank you once again for everything.

To everyone who was part of Andrew Watt's group, thank you and I will miss each one of you. Thank you Natasha Hjerrald and Darren Neo for being a fun and enthusiastic lab mate. I am thankful that we started our study together, going through all the difficult course works and GSO forms. I give thanks to Nina for always being so organized and happily having small talks with me. Thank you Yujiro Tazawa, Zhanet Zaharieva, Nanlin Zhang, and Wing Chung Liu for bearing my continuous Disney songs in the lab. Especially Yujiro thank you for taking the role of doing the lab orderings on my behalf. Without you I wouldn't have able to finish the experiments on time!

Last but not least my Assia Kasdi. Thank you for all the valuable chemistry knowledge and thank you for always making my life at Begbroke exciting, even on Saturdays! The saddest part of finishing my DPhil is that we can no longer have our discussion in the 'office'. I hope you will always be part of my life. Thank you again and I will miss you very much.

I would like to thank my friends outside the lab who have made my Friday evenings entertaining and fun. Hana Oh, Minho Lee, and Jong Min Lim. I would like to add special

thanks to my best friend Sangwon Seo. Thank you for always being a good friend to talk to. Please don't change and stay the same Sangwon that I know.

To my one and only sister Inhee Yeom. You have always been my greatest role model and motivation. Although I was never the best person at expressing my feelings towards you. But I still hope you know that I love you so much and thank God that he has given you to me as my sister. Hopefully not to long till we go on our next sisters holiday.

I would like to thank my parents for being a wonderful supporter throughout my 9 years of study in the UK. You are the greatest parent that anyone can ask for. 언제나 한결같이 제가 하고 싶은 것을 하게 해주시고 응원해주셔서 감사합니다. 정말 그 누구보다도 무한한 사랑으로 키워주셔서 감사합니다. 엄마 아빠가 제 부모님이라서 너무 행복하고 감사합니다. 저에게 주셨던 사랑, 다 갚지 못하겠지만 평생 효도하면서 살게요. 많이 사랑합니다.

Lastly, I would to thank Hyunwoong David Do for being there for me throughout my studies. I think you are the only person in the world who can make me laugh and cry at the same time. Thank you for being caring, loving, and fun boyfriend. 사랑하는 도현웅님, 언제 한결같이 옆에 있어줘서 감사해요. 그대를 만나서 배려와 진정한 사랑이 무엇인지 배워요. 아무리 일이 바빠도 새벽에 퇴근하면서 30 분씩 통화해주는 그대 정말 너무 멋진 사람입니다. 앞으로도 지금처럼 즐겁게 잘 지냅시다.

Declaration of originality

This thesis is an account of work carried out by the author in the Department of Materials, the University of Oxford under the supervision of Professor Andrew Watt and Professor Hazel Assender. Any work of others that has been utilised, directly or indirectly, is duly acknowledged in the text, and a list of references is presented at the end of each chapter. No part of this thesis has been submitted towards the completion of another degree at the University of Oxford or elsewhere. Parts of the thesis have been submitted to or published in the following conference presentations and patent:

Inji Yeom, Assender H.E., Watt A.A.R., **Ternary colloidal quantum dot for electroluminescent device**. Nanocrystal Zing Conference, Dominican Republic, 2014. (Poster presentation)

Inji Yeom, Assender H.E., Watt A.A.R., **Interface and surface engineering of colloidal quantum dots for photovoltaic applications.** Rank Prize Fund conference 2015-Symposium on Electroluminescent and Photovoltaic Effects in Nanocrystal Quantum Dots. (Oral presentation)

Oxford University Innovation Limited, **Fibre-based optical concentrator.** Patent application number 1612737.5, Filled 22 July 2016

Signed…… Date……..

Table of Contents

List of Tables

List of Figures

List of Abbreviations

AIS	AgInS2
Al	Aluminum
CB	Conduction band
CIS	Copper Indium di-Sulphide
Cu	Copper
DAP	Donor-Acceptor-Pair
DDT	1-Dodecanethiol
EPCF	Effective photon concentrating factor
FWHM	Full-width-half-maximum
HR-TEM	High resolution transmission electron microscopy
HSAB	Hard Soft Acid Base
HSAB theory	Hard-soft-acid-base theory
In	Indium
In_{Cu}	Indium substituted in copper vacancy
LED	Light Emitting Diode
LSC	Luminescing solar concentrator
OA	Oleic acid
ODE	1-octadecene
OLA	Oleylamine
PD	Photodiode
PLQY	Photoluminescence quantum yield
PV	Photovoltaic
QD	Quantum dot
RI	Refractive index
TIR	Total internal reflectance
TMSS	Hexamethyldisilathiane
VB	Valence band
V_{Cu}	Copper vacancy
VLC	Visible light communication
V_S	Sulfur vacancy
Zn	Zinc
ZnS	Zinc Sulphide

Chapter 1 –Introduction

1.1 $CuInS_2$ and $AgInS_2$ nanocrystals for communication application

The concept of 'nano' dates back to sixth century BC when nanotechnology was used in the Attic region (Greece) to decorate vases using black magnetite nanoparticles [1].

Nanoscale materials are of a great interest as their physical and chemical properties change from their bulk state. For instance, in semiconductor nanocrystals, if the nanocrystals are smaller than the material's Bohr exciton radius, the electronic bands are confined to discrete quantised energy levels. Optical, electronic, and thermal properties become dependent on the nanocrystal size and shape if the size of the nanocrystals fall below the Bohr radius These nanocrystals are referred to as quantum dots (QDs) [2].

By using a solution-based synthesis route to build nanostructures from the 'bottom up', development in a variety of shapes and sizes, such as nanocrystals, nanorods, and nanosheets, has accelerated [3,4]. Among the semiconductor nanocrystals, group III-V or II-VI elements have shown interesting properties, and luminescence with a high quantum yield (up to 80%) has been observed. In addition, changing a nanocrystal's shape and size has allowed for PL wavelength modification [5].

In the past two decades, researchers have tried to broaden the work to I-III-VI copper based ternary and quaternary nanocrystals [6]. They have shown unique property where the band gap can be changed through compositional tuning [7]. Furthermore, modification through the addition of a shell or by doping has been shown to enhance photoluminescence characteristics. With the advancement of property control through nanocrystal synthesis, applications in biological imaging and optoelectronic devices have

been growing. However, many significant challenges remain for the synthesis of nanocrystals and understanding the relationship between their physical and chemical properties.

The technological advancement of mobile devices has led to exponential growth of mobile data use. According to the research by Cisco, data traffic reached 7.2 exabytes per month at the end of 2016, and it is predicted to grow to 49 exabytes by 2021[8]. However, available radio frequencies are limited. Therefore, visible light, with a larger available spectrum, has been receiving attention as an alternative solution to the radio frequency congestion.

Visible light communication (VLC) refers to an optical wireless communication method that uses visible light (380nm to 750nm). The concept emerged with the development of high power light emitting diodes (LEDs). In a VLC, a light source (e.g., an LED) will act as the transmitter, and photodiode or image sensor will act as the receiver. The main advantage of using a VLC is that it does not require a new infrastructure, since any LED can act as a transmitter source. Additionally, visible light, when compared with radio frequencies, are known to be confined by opaque walls. Therefore, it can be used for confidential data transfer.

However, the use of VLC is limited by line of sight. For instance, when the detector is not perfectly aligned with the transmitter, the intensity of light detected will decrease. This will restrict the amount of data received, as the amount of data transferred is proportional to the amount of light detected. This limitation cannot be resolved by simply increasing the size of the detectors as the detectors' (photodiodes) size needs to be kept

small in order to maximise its bandwidth. Increase in detector size will increase the capacitance which will lower the bandwidth. To overcome the issue, a luminescent concentrator (LC) can be used to amplify the detection of light. The LC is a plate-like device that consists of layers of transparent polymers and luminescing materials on a glass substrate. Its role is to absorb light from a large area and concentrate the light at the edges of the substrate to directly couple to the photodetector.

The concept of a LC has already been demonstrated in photovoltaic applications as a luminescing solar concentrator (LSC) to concentrate light onto solar cells. The application has shown to increase the geometrical concentration factor by 10 when compared to a solar cell on its own [9].

In this thesis, a LC will be used as a light antenna for visible light communication (VLC) [10]. The main material properties required for a VLC concentrator are high PLQY (near unity), photo-stability, and large Stokes shift [11]. From the limited literature available, one of the materials used was an organic dye [12], Coumarin 6 [13], due to its high PLQY. However, organic dyes suffer from low photo-stability and large reabsorption (low Stokes shift). As an alternative, Cd-based nanocrystals have been considered, but due to their toxic nature, and the consequent strict regulation of cadmium in Europe [14], they face limitations for large scale applications in consumer products.

As an alternative to Cd nanocrystals, less toxic ternary nanocrystals of Copper-Indium-di-Sulphide (CIS) and Silver-Indium-di-Sulphide (AIS) were considered. CIS has already been used for LSC due to its high molar absorption coefficient [15], large Stok'e shift (~120nm) [16], and its air stability [10]. With similar properties as CIS, the AIS synthesised in

Chapter 5 has been shown to reach a high PLQY of >80%. Thus, in this thesis, AIS nanocrystals have been chosen as a concentrator material.

For light to be concentrated and transferred to the edge for the detector to absorb the maximum light, total internal reflectance (TIR) needs to occur, where the light is trapped in the concentrator layer. This occurs when the light is transmitted from a large to a small refractive index (RI) material, where the angle of incidence is greater than the critical angle (defined by Snell's Law). As a result, near-perfect reflection occurs. Therefore, the concentrator structure will be glass (substrate) – Low RI (n= ∼1.3) – Polymer with nanocrystals (n >1.5) - Air (n= ∼1).

1.2 AIM of thesis

Ternary nanocrystals have the advantage over current binary luminescing nanocrystals, as they do not contain toxic elements such as cadmium or lead. However, they face limitations in synthesis, as controlling the reactivity of the two cation precursors is challenging. Therefore, the two major goal of this thesis are first, to find a new synthesis route for $CuInS_2$ and $AgInS_2$, while studying properties that affect photoluminescence properties. Secondly, fabricate the first ever $AgInS_2$ visible light communication (VLC) concentrator. In order to achieve this, the following questions are addressed;

I. Can low injection temperature synthesis produce luminescing $CuInS_2$ nanocrystals? What are the effects of changing the injection temperature and precursor ratio on the PL properties?

II. By using halide precursors, can we control the reactivity of the precursors? Would halide precursor have the advantage of enhancing photoluminescence quantum yield through halide passivation?

III. Using the same synthesis method as for $CuInS_2$, could $AgInS_2$ be synthesised? Are there any differences in the results? How can we produce a highly luminescing $AgInS_2$?

IV. Could $AgInS_2$ nanocrystals be used as concentrator material for light visible communication (VLC)? What are the effects of the host polymer? What are the differences in gain with different device structures?

1.3 Structure of thesis

Chapter 2, provides a literature review on the current synthesis procedure for ternary nanocrystals. The theories and mechanisms related to PL emission are reviewed in detail, with the addition of current applications in the field. Chapter 3, provides the experimental methodology of synthesis and characterisation techniques. Chapter 4, studies $CuInS_2$-ZnS synthesis, where the effects of modifying injection temperature and precursor ratio are studied. Using halide precursors the relative cation reactivity is predicted, and improvements in PL are discussed. Chapter 5, based on the study from Chapter 4, shows development of a new synthesis of $AgInS_2$. Using an *in-situ* PL study, the reaction dynamics are studied. Chapter 6, fabrication of visible light communication application using $AgInS_2$ nanocrystals. Lastly, Chapter 7 concludes the thesis with the summary of the findings and future work that may be carried out.

Chapter 2 -Literature Review

2.1 History of luminescent nanocrystals

In 1981, semiconductor nanocrystals, known as quantum dots, were discovered by the Russian solid state physicist, Alexey Ekimov, who was studying crystals of semiconductors embedded in glass [17,18]. Later, in 1985, the relationship between the size and band gap of semiconductor nanocrystals was defined by Louis Brus [19,20]. From this point onwards, the development of nanocrystals was accelerated.

In 1993, notable progress was made when Murry *et al*. successfully synthesized CdX (X = S, Se, Te) nanocrystals sized between 1.2 and 11.5 nm [21]. CdX was a popular choice of material because of its robust optical and electrochemical properties. However, using Cd-based nanocrystals for applications faced limitations as a result of its toxic nature [5,22].

To reduce non-radiative recombination due to surface defects in photoluminescence applications, a core-shell structure was used [23]. Initially, CdS was used as a shell material on CdSe to improve PLQY, but for biological applications, in order to reduce Cd exposure, ZnS was utilised instead [22,24]. The single-shell structure further progressed to a double shell to enhance PLQY further, e.g., CdTe, CdS and ZnS [25].

The synthesis methods for Cd-based nanocrystals can be divided into two main approaches - physical and chemical. The physical approach is through epitaxial growth or nanoscale patterning with high-resolution electron beam lithography and a post-etching process. The drawbacks with this method are the random sizing and strained interface, as well as damage to the bulk crystal. The chemical approach overcomes these problems, where the size and composition can be more easily controlled, which keeps

the size variation within 5–10%. The process involves decomposition of an organometallic precursor at a high temperature of ~300 °C, which is assisted by a long-chain organic ligand, such as tri-n-octylphosphine oxide (TOPO) to regulate growth and stability. This is then followed by an injection of a chalcogen precursor at a lower temperature of ~180 °C [21,26].

Cd-based nanocrystals are generally hydrophobic due to the use of hydrophobic organic ligands during the synthesis process. For biological applications within *in vitro* and *in vivo* environments, nanocrystals need to be water-soluble. This can be achieved by either ligand exchange [27,28], encapsulation by amphiphilic diblock [29] or triblock copolymers [30], silica coating [31], or phospholipid micelles [32]. Further progress has been made with hydrophilic ligands during the synthesis process, such as 3-mercaptopropionic acid (MPA) [33], thioglycolic acid (TGA) [34], and L-cysteine [35].

With these improvements over the past two decades, near-unity PLQY has been reported with Cd-based nanocrystals [36,37]. However, removal of hydrophobic organic ligands produces a decrease in PLQY. Bawendi's group has shown that PLQY of CdSe/CdS was ~96%, but it was further reduced to ~70% with ligand exchange of hydrophilic thiols [36]. The PLQY was later recovered by increasing shell thickness from 7 monolayers to 10 monolayers [38]. As CdSe/CdS is a type 1 core-shell structure, where the core conduction and valence band edge lies within the band gap of the shell, by increasing the shell thickness, electrons and holes were confined within the core, therefore enhancing the overall PL [39].

A ZnS shell was demonstrated to somewhat passivate the Cd core. However, for cellular or *in vivo* studies, it has been suggested that there is a constant leak of Cd ions, which can lead to cytotoxicity [40]. Hence, there has been a consistent effort to find an alternative material to replace Cd nanocrystals.

2.2 Ternary copper and silver chalcogenides

One of the alternatives for Cd-based nanocrystals is I–III–VI ternary nanocrystals as they are less toxic than Cd. Many different types of ternary nanocrystals can be formed from different combinations of elements from each group, for example, group I (Cu, Ag), group III (Al, Ga, In, Ti), and group VI (S, Se, Te). The bulk properties of several ternary and quaternary nanocrystals, such as band gap, crystal structure, and lattice parameters, are summarised in Table 1. Among the many ternary nanocrystals, two types specifically, $CuInS_2$ and $AgInS_2$, are discussed in depth in this thesis.

Table 1–Summary of the band gap, crystal structure, and lattice parameter values for some bulk ternary and quaternary nanocrystals.

Material	**Band gap at 300 K (eV)**	**Crystal structure**	**Lattice parameters (Å)**
$CuInS_2$	1.53	Chalcopyrite	a = 5.52, c = 11.12
$CuInSe_2$	1.05	Chalcopyrite	a = 5.61, c = 11.02
$CuFeS_2$	0.60	Chalcopyrite	a = 5.28, c = 10.41
$AgInS_2$	1.98	Orthorhombic	a = 7.00, b = 8.28, c = 6.70
Cu_2ZnSnS_4	1.5	Kesterite	a = 5.45, c = 10.86
$Cu_2ZnSnSe_4$	1.02	Kesterite	a = 5.61, c = 11.20

Figure 1 depicts how binary, ternary, and, finally, quaternary nanocrystals are related. Ternary nanocrystals are derived from groups II–VI, where two divalent cations are replaced with one monovalent and one trivalent cation. Furthermore, quaternary nanocrystals are derived from ternary nanocrystals by substituting one trivalent cation with one divalent and one tetravalent cation [12].

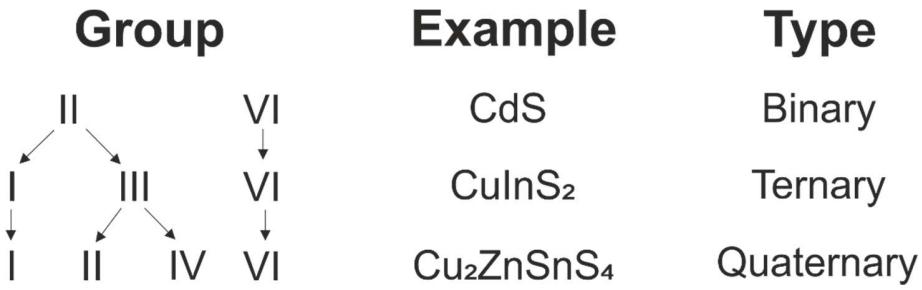

Figure 1-Schematic of binary–ternary–quaternary relationship. Schematic adapted from reference [12].

2.2.1 General properties of binary and ternary nanocrystals

The general properties of binary and ternary nanocrystals are compared in Table 2. In this study, it is noted that compared to the binary nanocrystals, ternary nanocrystals have larger Stokes shifts and longer PL lifetimes because of a different recombination pathway. The large full-width-half-maximum (FWHM) is mainly caused by the defect nature of ternary nanocrystals. Their defects result in donor–acceptor pair (DAP) recombination, which is known to be the main recombination pathway (explained in detail in Section 2.2.3) [6].

Table 2–Summary of the properties comparing between binary and ternary nanocrystals [41].

Properties	**Binary nanocrystals**	**Ternary nanocrystals**
Spectral tunable window	UV–Visible and NIR	UV–Visible and NIR
PLQY	Hydrophobic, >50%	Hydrophobic, >50%
	Hydrophilic, >30%	Hydrophilic, 20–50%
FWHM	25–35 nm	80–120 nm
Stokes shifts	<100 meV	200–300 meV
PL lifetime	~20 ns	100–350 ns

2.2.2 Crystal structure

$CuInS_2$ crystal structure

There are three main crystal structures for $CuInS_2$ (CIS): chalcopyrite (CP), zinc blende (ZB), and wurtzite (WZ), as shown in Figure 2.

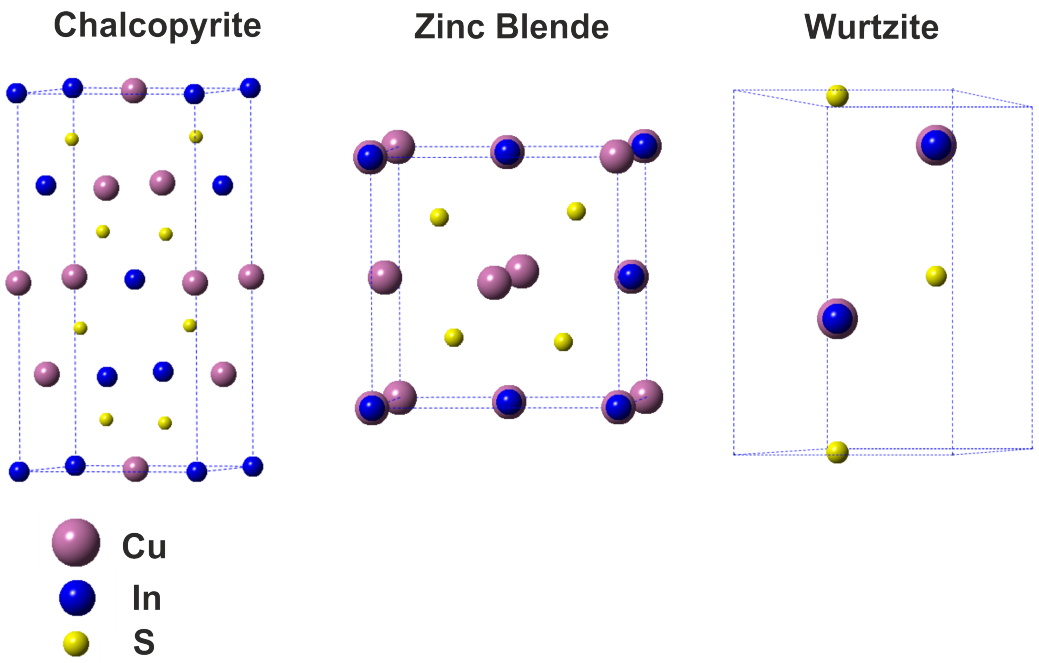

Figure 2–Schematic of the chalcopyrite, zinc blende, and wurtzite crystal structures produced using Crystal maker software.

Chalcopyrite (CP) is the most common CIS structure, a cation-ordered structure with each sulfur atom bonded to two In or Cu cations. The bond lengths between the cations and anions are different, $R_{Cu-S} \neq R_{In-S}$, where In–S is 5% larger than the Cu–S bond [42]. This leads to an anion displacement of a close-packed arrangement, which leads to a distortion of the crystal lattice. The strain effect becomes greater with an increased Cu/In ratio because the tetragonal strain parameter (η), is defined by $\eta = \frac{c}{2a}$, where a and c are the unit-cell parameters. Thus, with increasing Cu/In ratios, the a and c unit-cell parameters

decrease and increase, respectively. In addition, because CP is a cation-ordered structure, the changes in Cu and In content lead to an internal defect structure. From the band-edge calculation, the direct band gap was 1.24eV, which is similar to the experimental value of 1.55eV [43].

The zinc blende (ZB) structure is a cubic cell that is analogous to CP, but is a cation-disordered structure. This leads to flexibility in composition as cations can exchange with one another rather than forming defects as in the case of CP. There have been reports of various compositions, such as $Cu_3InS_{3.1}$ to $CuIn_{2.2}S_{3.8}$ [44]. This flexibility provides control of n- or p-type optical tuneability [45]. For instance, increasing Cu content would be doping with a lesser valence electron, creating a greater number of hole concentrations, thus becoming a p-type CIS. Meanwhile, an increase in In content will enhance electron concentration, hence becoming a n-type CIS. Achieving a ZB structure in a synthesis is difficult and the by-products of other crystal structures may form as well. ZB and CP have a similar lattice spacing of 0.32 nm. Therefore, it is difficult to distinguish one from another using HR-TEM. However, since ZB and CP have a slightly different diffraction pattern, the two structures can be distinguished by using X-ray diffraction (XRD)

The wurtzite (WZ) structure has sulfur ions closely packed hexagonally, and In and Cu are randomly placed within the tetrahedral interstices of the sulfur framework while balancing the charge. WZ allows random cation distribution, where stoichiometric flexibility is possible [46]. Furthermore, compared with the CP and ZB structures, the lattice spacing is 0.34 nm and the XRD diffraction patterns are distinguishable. Therefore, WZ can be easily distinguished from the other structures.

Different structures can be accomplished by varying the ligand species [44], pH [46], and reaction temperatures [47]. For example, bulk CIS and CP are stable at room temperature, whereas ZB and WZ are stable at high temperatures as random cation ordering occurs. In addition, ZB and WZ can be grown using Cu_2S as a template [12]. Xie *et al.* demonstrated that by raising pH, CIS gradually changes from CP to WZ [46]. Sodium hydroxide (NaOH) was employed to elevate the pH from 1.27 to 5.3 while thioglycolic acid (TGA) as a reducing agent. According to the hard-soft–acid-base (HSAB) theory, TGA is a soft base and will bond more strongly to Cu, a soft acid, rather than a hard acid In. At a low pH, TGA reduces the Cu ions slowly while In has enough time to be reduced, and when sulfur is added, because of a well-balanced composition, the CP CIS is formed. In contrast, at high pH, NaOH constantly dissociates the CIS complex and releases Cu^+. Therefore, when sulfur is added, Cu_2S is initially formed, which has a hexagonal structure and with the addition of In, nanocrystal grows into a WZ CIS.

$AgInS_2$ crystal structure

Similarly, AIS has three crystal structures, CP, ZB, and WZ [48]. Among them, the two most common crystal structures observed are CP and WZ. It has been observed that at high temperature (>620°C), WZ is stable, whereas at low temperature (<620°), CP is stable [49]. AIS–CP structures are known to have an optical band gap of 1.87 eV, while for AIS–WZ, it is 1.98 eV [50].

Recently, interest in the synthesis of WZ has increased as it has been shown to achieve a higher PLQY than ZB. As discussed for the CIS crystal structure, ZB features a cation-

disordered structure, though WZ is a cation-ordered structure. Therefore, WZ may contain more defects, which enhances the DAP recombination pathway [50].

2.2.3 Defect structure

Defects are an important part of ternary nanocrystal properties as they bestow unique features that are not observed in binary nanocrystals. They play a significant role in radiative recombination pathways by changing the band gap and influencing optical properties. For example, from the original chemical formula of $CuInS_2$, defects can be formed by altering the Cu/In ratio [51]. CIS can be formed of either the n-type with In in excess or the p-type with excess S. A study by Tapley *et al*[52]., demonstrated using X-ray absorption near-edge structures (XANES) that, similar to CIS, $CuInSe_2$ when Cu vacancy concentrations are increased and n-type characteristics are promoted. Therefore, controlling stoichiometry can affect both PLQY and PL emission wavelength.

Based on theoretical investigations, it is known that defect structures are easier to form in ternary nanocrystals than in analogous binary nanocrystals. Each ternary nanocrystal is derived from a binary nanocrystal. For example, ZnX is a binary analogue of $CuGaX_2$ (X = S, Se, and Te) whereas $Zn_{0.5}Cd_{0.5}X$ is the binary analogue of $CuInX_2$.

Cu, being monovalent, has a weaker Cu–S covalent bond compared to divalent Zn. Therefore, it is much easier to generate a Cu vacancy. Zhang *et al.* showed that the formation energy of a defect pair, such as ($2V_{Cu}^{-} + In_{Cu}^{2+}$) or ($Cu_{In}^{2-} + In_{Cu}^{2+}$), is low and the formation process is exothermic (–1.46 eV). Hence, defect formation is energetically favourable [51].

The main conduction pathway for II–VI binary semiconductor nanocrystals is by valence band (VB) and conduction band (CB) processes, where the states are produced by p orbitals from group VI anions and s orbitals from group II cations. For CIS, the VB is comprised of Cu 3d orbitals hybridized with p orbitals from group VI anions, and CB from Cu 4s orbitals mixed with the p character from the anion [53]. For AIS, it has been reported that the VB consists of 3p orbitals of S and 4d orbitals of Ag, while CB is composed of 5s5p orbitals of In and 3p orbitals of S. Therefore, for CIS, the optical band gap is influenced primarily by Cu content, and for AIS, depending on the Ag content, the VB can be shifted [54]. This is a starting point that has led to various theories for ternary nanocrystal recombination pathways.

As introduced in the previous Section 2.2.2, there are three common CIS crystal structures, CP, ZB, and WZ. Most of the defect studies published in the literature are based on the CP structure as it is a cation-ordered structure, thus changes in cation ratios are accepted as defects. In contrast, ZB is a cation-disordered system, wherein Cu and In cations are easily exchanged. Therefore, various stoichiometry can exist. Nevertheless, there has been a report stating that defect-related emissions have been observed with ZB CIS [55]. However, further study is required to verify this case. WZ has similar properties to CP; a broad PL emission (FWHM = 200 nm) and a large Stokes shift (~200 meV) [56]. However, little research has been carried out on the WZ structure. Thus, in this section, defect recombination theories based on studies with the CP structure are discussed.

There are currently three different theories suggested for the radiative recombination of CIS and AIS. The first is DAP recombination, which is regarded as the main theory in the

field. There are also alternative theories where both quantised states and defects play a role in recombination. This ultimately led to the second theory, donor state-to-VB, and the third theory, the CB-to-acceptor state. Figure 3 outlines the different theories on recombination, along with a relatively new theory that suggests point defects can also act as donor and acceptor states. However, there is no overall agreement to date on the nature of the recombination process.

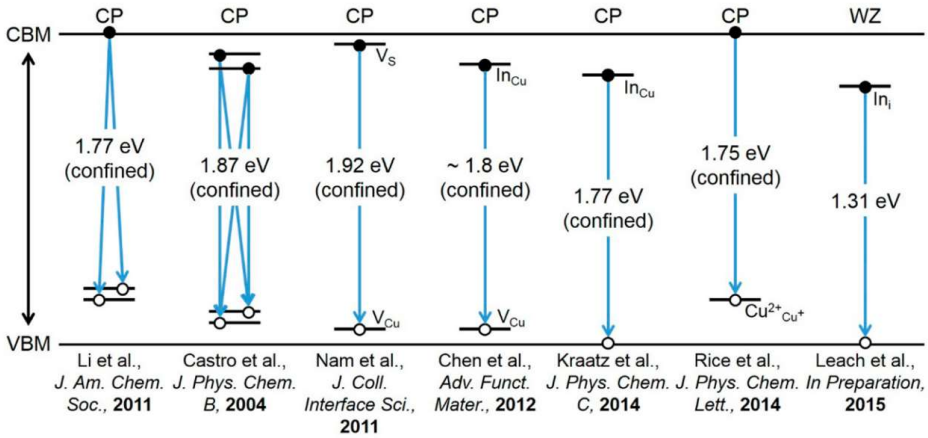

Figure 3–The three different recombination theories are summarised in the schematic. Showing DAP theory supported by Castro, Nam, and Chen, CP to acceptor supported by Li and Rice, lastly donor to VB supported by Kraatz and Leach. Image reproduced from reference [15].

Donor–acceptor pair recombination

One of the most often used models for ternary nanocrystal radiative recombination is DAP recombination. Here, the main defect pairs involved for CIS are Cu vacancy + In replaced Cu site [$2V_{Cu}^{-}$ + In_{Cu}^{2+}] [57], and for AIS, Ag vacancy + In replaced Ag site [$2V_{Ag}^{-}$ + In_{Ag}^{2+}].

Castro *et al*. [58] and others [42,59,60] have shown for CIS that the main emissive recombination is solely from DAP recombination, and the band gap is said to be 1.87 eV. This model was

used to explain the band-gap shift to shorter wavelengths with a decrease in the Cu/In ratio [42].

From time-resolved photoluminescence (TRPL) spectra for CIS, it was determined that PL lifetimes are long, between 100 and 300 ns [7], compared with CdSe at 10–30 ns. In addition, PL decays were not single-exponential but double or triple. Zhong *et al*. observed PL lifetimes of 4–12, 28–60, and 140–300 ns [7], originating from band exciton, surface related, and DAP recombination, respectively. If CIS nanocrystals were over-coated with a ZnS shell, only the long PL lifetime was evident [56]. This indicated that surface defect recombination was suppressed and DAP recombination was the dominant luminescence mechanism. For AIS, similar observations were seen as stated earlier [61].

Donor state to valence band

Omata *et al*. [62] and others [63] have suggested that there is a transition between a localized state and the VB as a recombination pathway. The argument is based on the fact that it fills the missing gap and explains the size-tuneable PL emission. If the nanocrystal size changes, VB shifts, thereby causing an overall PL shift. However, later, it was contended by DAP supporters that if the trap state was positioned close to the VB or CB edge, a perturbation in the band energy (e.g., confinement) could cause a change in band gap [59].

This was again backed by supporters of donor state-to-VB theory through ultrafast spectroscopy studies, which demonstrated that radiative transitions occurred from or to a level within the energy bands [63,64]. In 2014, Kraatz *et al.* provided evidence that ultrafast radiative recombination occurred using an excitation laser, stating that non-radiative

recombination occurs from CB. However, the long-lived radiative recombination was from the donor state to VB [63].

Conduction band to acceptor state

Li *et al*. [56] performed luminescence decay measurements, observing that two different energy bands at 670 nm and 700 nm existed. However, by over-coating with a ZnS shell, the low-energy component decreased and the overall PL lifetime increased, showing that the luminescence transition was from the CB to a localised intragap state.

Point defects

In 2012, Chen *et al.,* [65] used density functional theory to calculate the transition energies of various point defects in CIS. From this viewpoint, the most common defects were found to be In_{Cu} (In replaced Cu), V_{Cu} (Cu vacancy), or V_S (S vacancy), which aligned with the experimental findings. However, Rice *et al.* [66] used magnetic circular dichroism to identify the presence of impure atoms, such as Cu^{2+}, within CIS. On the contrary, Chen *et al*. ignored the possibility that interstitial atoms may play a role in such luminescence. However, further studies must be conducted to calculate the defect energy more precisely.

Similarly, in the case of AIS, Krustok *et al*. found point defects as V_S (S vacancy), V_{Ag} (Ag vacancy), S_i (S interstitial), and Ag_i (Ag interstitial) when thin films were annealed in different atmospheres [67]. In addition, Hamanaka *et al*. and Mao *et al*. also suggested that Ag and S interstitials can act as donor and acceptor sites [68,69]. However, up to this point further studies are required to fully understand point defects and their impact.

2.2.4 Photoluminescence

Photoluminescence mechanism and rationale for DAP recombination theory

Photoluminescence occurs when an excited photon relaxes and emits its energy as light. In the case of binary nanocrystals, photoluminescence occurs when an electron from the CB recombines with a hole from VB. By contrast, the photoluminescence mechanism of ternary nanocrystals is more complex and not fully understood. As mentioned in Section 2.2.3, the 3 main theories for the mechanism of the recombination pathway are: 1) CB to acceptor, 2) donor to VB and 3) DAP. Although there is no single theory that provides a conclusive explanation, all agree that either donor, acceptor or a combination of the two play a crucial role in the recombination process.

Berends *et al*. [70] and Kraatz *et al.* [63] have studied theory 1 (CB to acceptor) and theory 2 (donor to VB), respectively. Both studies used transient absorption (TA) spectroscopy and showed similar observations, but the interpretations were different. For instance, a change in the absorption spectrum as a function of time and wavelength was observed. Berends *et al.* referred to this phenomenon as a band edge bleach, whereas Kraatz *et al*. explained this phenomenon as a ground state bleach, i.e., that the recombining electron originates in the CB or the donor state, respectively. However, both agreed that the time lag between absorption and emission spectra was the result of either a donor or an acceptor.

It is important to note that the time taken for an electron to fall to the donor state is in the pico-second range. However, Berends *et al*. used equipment that could not measure electron trapping on a subpicosecond time scale. Therefore, they neglected the possibility of electron transfer to the donor state. In comparison, Kraatz *et al.* performed TA

measurements at 772nm excitation wavelength in a subpicosecond time scale. The 772nm excitation wavelength is known to be energetically insufficient for direct absorption by the CB. Despite this, the wavelength has shown that stimulated emission was still present, which suggests that the electron is present in the donor state. However, Kraatz *et al*. simply states that for the recombination site, the PL maximum reached by the nanocrystal is 693 nm (1.79 eV), thus it corresponds to the 'donor to VB band' recombination. It is noteworthy that the PL maximum can be easily affected by composition or nanocrystal size. Therefore, whether the recombination occurs at the VB or the acceptor site still remains.

In addition to the ambiguous experimental interpretation that supports theory 1 and 2, both studies miss a critical point of the compositional effects on the photoluminescence behaviour, which is a unique property of the ternary nanocrystal.

The optical properties observed in ternary nanocrystals include, (a) a large Stokes shift ($E_{abs} - E_{PL}$), (b) long PL lifetime, (c) changes to PL emission wavelength with composition, and (d) enhancement of PLQY associated with an increase of indium concentration. While theory 1 and 2 can somewhat explain observations (a) and (b), the experimental data (c) and (d) cannot be explained. In comparison, theory 3 (DAP) can be used to explain all four properties (a)-(d). Chevallier *et al*., [71] studied $AgInS_2$-ZnS with XPS. They detected signals of In $3d_{5/2}$ and Ag $3d_{5/2}$, which is 1eV higher in energy. This implies that there are indium substitutions (donor) and silver vacancies (acceptor). He also observed a change in the intensity of the XPS signals with a change in the ratio of Ag/In. Furthermore, various compositions were studied to investigate the role of defects in the

photoluminescence process. The results showed that the amount of radiative recombination followed the same trend as the total concentration of the defects detected by XPS. Therefore, this result clearly shows that the recombination pathway was due to DAP.

DAP recombination theory can be used to explain the four optical observations of ternary nanocrystals mentioned above.

1) A large Stokes shift is observed as there is an energy difference between the absorption (CB to VB) to emission (donor to acceptor). The band gap between donor and acceptor is smaller than CB to VB, which explains the red shift of the PL emission [72,73]. According to the DAP characteristics observed by Li *et al*. a low energy tail in the PL band can extend beyond the bulk CIS band edge [56].

2) Two PL lifetimes are observed in the absorption spectra of AIS nanocrystals. The short PL lifetime (~25ns) was from non-radiative surface defect recombination, while the long PL lifetime (~200ns) was due to DAP recombination [74]. The DAP recombination has a long PL lifetime as a delay time occurs for an electron to fall from the conduction band to the donor state [75].

3) The change in wavelength of the PL emission according to composition can be explained by DAP. The CB and VB are affected by changes in the Cu content as reviewed in the previous Section 2.2.3. The valence band of copper-based chalcogenides is composed of Cu 3d orbitals hybridised with the p orbital of the group 5 element. Meanwhile, the CB is formed by Cu 4s orbital with some p character of the chalcogen

atom. Thus, if the Cu content increases, the VB will shift upwards, thereby decreasing the overall band gap [76].

4) The PLQY of the ternary nanocrystal can be improved by changing nanocrystal composition due to the DAP properties (reviewed in Section 2.4.1). Jara *et al*. have demonstrated that, regardless of the nanocrystal size, changing the composition can enhance the PLQY due an increase in the number of donor/acceptor pairs [77] .

When considering the relationship between nanocrystal size and PL emission wavelength, many observations suggest that CIS emission has a slight red-shift that is associated with the growth of nanocrystal [42] . The AIS PL wavelength has also been shown to be affected by the nanocrystal size [73]. If the V_S and V_{Cu} defect states lie ~35meV below the CB and ~100meV above the VB, which is close to both CB and VB, the position of the sub-band gap will be affected accordingly based on the change in size of the nanocrystal [59].

Photoluminescence dependence of temperature

For CIS, PL emission has shown to decrease in intensity and red-shift (lower energy) as the temperature increases, as shown in Figure 4. This is a natural observation seen in bulk and nanocrystal semiconductors. As the temperature rises, the trapped electrons and holes become free and play a role in the non-radiative recombination. Furthermore, thermal ionisation of carriers occurs, where carriers bind to acceptors and donors [78, 79]. Thus, a peak shift to a lower energy with increase in temperature occurs as the band gap reduces.

The recombination energy of pair separation is characterised by the equation.

$$hv(r) = E_g - (E_D + E_A) + E(r),$$

E_g is the band gap energy, E_D is the ionisation energy of the donor, and E_A ionisation energy of the acceptor. The function $E(r) = e^2/\varepsilon r$ represents the coulomb interaction energy, where r is the distance between donor and acceptor and ε is the dielectric constant. When the temperature increases, the distance between the pair increases. This is due to an increase in thermal ionisation of carriers to the donor and acceptor increases. This leads to an overall E(r) decrease, which will reduce the overall band gap [80].

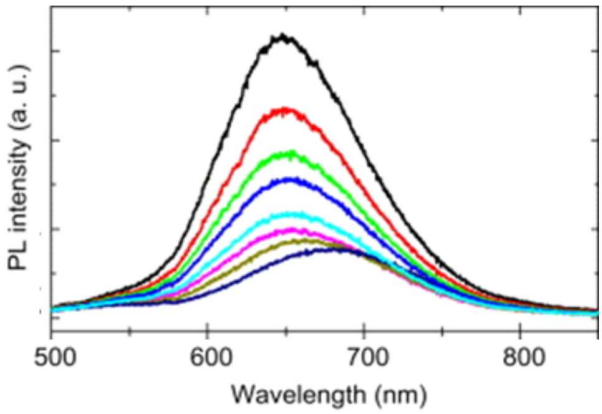

Figure 4- PL spectra of $CuInS_2$ core at temperatures 92, 115, 138, 185, 205, 287K measured at excitation 488nm [81].

2.3 Synthesis methods

2.3.1 Nucleation and growth

The goal for nanocrystal synthesis is to achieve a narrow size distribution. As described by La Mer, there are two important steps during nanocrystal synthesis, i.e., rapid nucleation followed by slow growth [82]. The rate of nucleation is controlled by temperature, interfacial tension, and the supersaturation of monomer concentration [83]. Nucleation takes place when the temperature is increased and the precursors are reduced in concentration, resulting in the formation of a large number of nuclei [84]. When the concentration of nuclei reaches supersaturation, nucleation occurs. Nucleation is terminated when supersaturation is lowered below a critical level. Following nucleation, growth takes place (Figure 5).

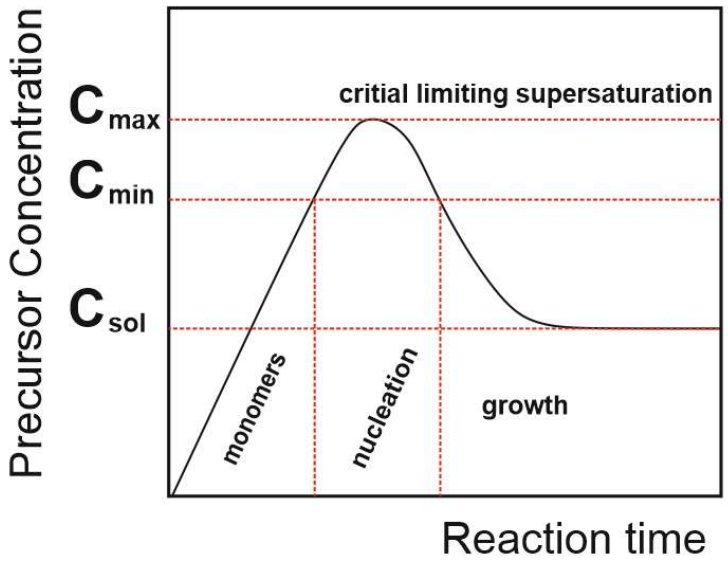

Figure 5–Schematic illustrating the nucleation and growth process of nanocrystals.

There are two main types of growth and they can be described by specific models - focusing and defocusing. The focusing model [85] describes diffusion-controlled growth, where nanocrystals grow with the addition of remaining unreacted precursor during nucleation. The growth rate is inversely proportional to the radius of the nanocrystals, where large particles grow slower than smaller particles [86]. This kind of growth narrows the overall size distribution. The defocusing model [85] is similar to Ostwald ripening, where nanocrystals grow from large particles on behalf of small particles re-dissolving [87]. When the particle is above the critical radius, Ostwald ripening becomes the dominating growth mechanism. It is favourable as interfacial energy decreases with the increase of size. This growth process also increases polydispersity, and as such, growth by the focusing model is preferred for obtaining narrow size distribution.

2.3.2 Synthesis procedures

Compared with binary II–V nanocrystals, synthesis of ternary nanocrystals is challenging as nucleation and growth rates are difficult to control because more than two precursors are involved. For CIS and AIS, the ionic radii of Cu^{+} (77 pm), Ag^{+} (114 pm), and In^{3+} (92 pm) are similar in size [88], but the reactivity of the two cation precursors are different as described by the hard soft-acid base (HSAB) theory, where Cu and Ag are soft and In is a hard Lewis acid. If the reactivity of the two cations are not balanced, it may result in production of unwanted by-products and high polydispersity. At present, the exact growth mechanisms of ternary Cu and Ag chalcogenides are still under debate. However, the most common methods used to control the reactions are through changes in reaction temperature and ligand combinations.

Ligands are important for controlling the monomer concentration and reaction rate [89]. Two cation reactivity of Cu (or Ag) and In are balanced with different ligands depending on their Lewis strengths according to HSAB theory. For example, thiol (soft base) reacts better with Cu (or Ag) (soft acid) [90]. Therefore, they suppress and control reactivity, whereas, In (hard acid) is well-matched with hard base ligands, such as fatty acids [91].

Ligands also play a role in stabilising nanocrystals during and after synthesis. They help passivate and protect the surface, and also prevent aggregation. There are three types of ligand groups: L-type, X-type, and Z-type [92]. L-type and X-type ligands donate one and two electrons to the metal, respectively, whereas Z-type accepts two electrons from a metal. Examples of L-type ligands are amines or phosphines [93] which have dynamic adsorption/desorption equilibria. X-type ligands are carboxylates or phosphates [94], where the net charge of the nanocrystals' stoichiometry is balanced by the X-type ligands and excess metal cations. Lastly, examples of Z-type ligands are Lewis acids or electron acceptors, e.g., boranes [95].

The commonly used groups of ligands for CIS and AIS nanocrystal synthesis are the L- and X-types. Compared with X-type ligands, L-type ligands can be easily removed through cleaning processes. As X-type ligands are two-electron donating bonding, they bond more tightly. As ligands play a crucial role in controlling reactions and nanocrystal stabilization, an ideal balance of ligand mixtures is important.

Ternary nanocrystal synthesis originates from II–VI binary nanocrystal synthesis, where there are two main types of synthesis procedures, as seen in

Figure 6, hot-injection or non-injection methods. Hot-injection synthesis is based on the injection of a precursor at a high temperature, where nucleation occurs rapidly. With non-injection synthesis, all of the precursors are added from the beginning, or a single-source precursor is used. The added reagents are decomposed at a high temperature, and nucleation takes place slowly as the process reaches supersaturation.

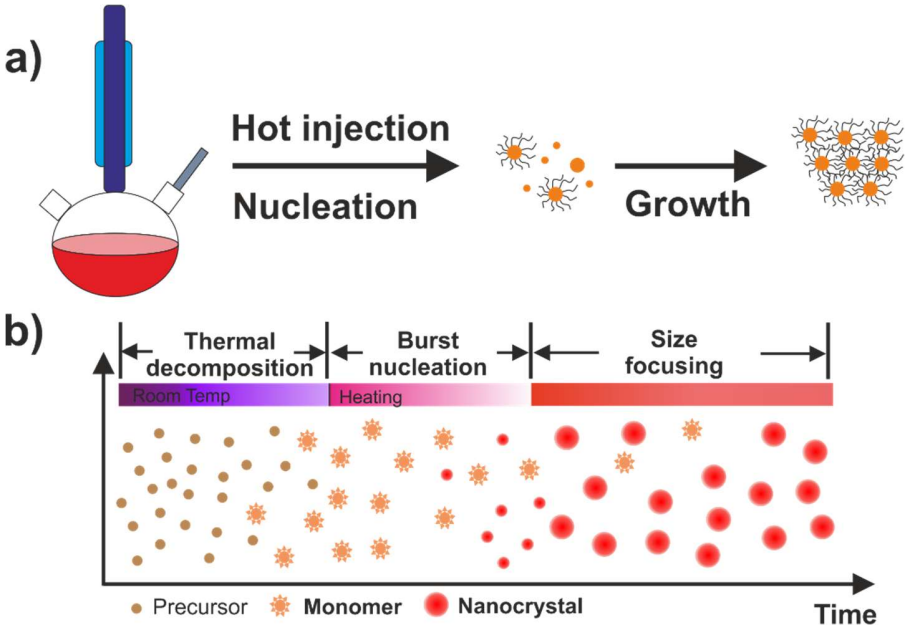

Figure 6–(a) Schematic of the hot-injection synthesis method. (b) Non-injection method where all precursors are present from the beginning of the reaction. Image adapted from ref [96].

The hot-injection method was first introduced by Murray *et al.* in 1993 [21], where size-controllable high-quality nanocrystals were synthesised. In 2008, Bawendi's group published the first hot-injection synthesis for a ternary nanocrystal, CISe [97], where they employed CuCl or CuI for the Cu precursor, InI_3 or $InCl_3$ for the In precursors, and bis(trimethylsilyl)selenide [$(TMS)_2Se$] for the Se precursor. Trioctylphosphine (TOP) and oleylamine (OLA) were utilised as both the ligand and solvent. Through this process, they

produced various stoichiometry of CISe that were used to tune the PL emission wavelength from red to the NIR region (640 nm to 975 nm). However, as $[(TMS)_2Se]$ is known to be a hazardous compound, others worked on a non-injection synthesis method to avoid this.

Cassette *et al.* [98] synthesized CISe by a non-injection method, using the precursors CuI, $InCl_3$, and selenourea with TOP, OLA, and dodecanethiol (DDT) as the ligand. Other non-injection methods used single-source precursors. The general formulae of the two compounds commonly used are $[(LR_3)_2M^1M^2(ER')_4]$ (L = P, As; E = S, Se; M^1 = Cu, Ag; M^2 = In, Ga; R = aryl, alkyl; and R′ = alkyl) and $M^1M^2[S_2CN(C_2H_5)_2]_4$ [41]. The single-source precursor synthesis requires a pre-synthesis of the two compounds, which are complicated and involves use of toxic chemicals. Hence, another type of non-injection synthesis was developed. This involved heating a metal precursor with a sulfur source for many hours.

Based on the study of CISe, CIS synthesis method was developed. In 2009, Xie *et al.* [90] synthesized CIS through a hot-injection method using CuOAc, $In(OAc)_3$, TOP, oleic acid (OA), octadecene (ODE), and n-dodecylthiol, which were all added to a three-neck flask and heated to 80 °C. Later, sulfur dissolved in OLA or ODE was injected to the solution at 180 °C. In this case, the CIS PLQY was 3%, but when a ZnS shell was grown, the PLQY increased to ~30%.

For non-injection CIS synthesis, the most common synthesis protocol uses DDT [41,7], where a mixture of CuI (or CuOAc), $In(OAc)_3$, and DDT was heated until the desired

nanocrystal size was observed. This synthesis method is popular as DDT serves as the sulfur source, stabilizing ligand, and solvent. Therefore, a well-controlled CIS synthesis is possible [7]. The other advantages are being scalable, reproducible, having low cost, and capable of producing high-quality CIS nanocrystals. Although the hot-injection method yields high-quality nanocrystals, the non-injection method is preferred as it is more convenient to be used on an industrial scale.

In 2011, instead of using a ZnS shell, ZCIS quaternary nanocrystals were synthesised [99] with CuOAc, $In(OAc)_3$, $Zn(OAc)_2$, sulfur powder, DDT, ODE, and OLA. From the synthesis, a high PLQY of over 70% was accomplished. Different heating temperatures were used to control the size of the nanocrystals. In addition, the author showed PL emission peak control with the Cu/Zn ratio, where Cu-deficient nanocrystals were blue shifted.

Similar to CIS, the hot-injection method for AIS synthesis involves injecting sulfur dissolved in OLA [100]. Precursors, AgOAc and $In(OAc)_3$ with octadecene, were added and degassed at 200 °C under vacuum. After sulfur injection, the solution was left for two hours heating and stirring.

For AIS non-injection method, thermal decomposition was used with a single-source precursor to synthesize 3–4 nm sized nanocrystals, reaching a PLQY of 40%. The single-source precursor was prepared using Ag nitrate and indium(III) nitrate with a sodium *N*,*N*-diethyldithiocarbamate trihydrate ($NaS_2CN(C_2H_5)_2$) mixture. Finally, by adding a ZnS shell layer, the maximum PLQY reached was 70% [101].

2.4 Improvements in PL

The main task for ternary nanocrystals is to enhance and modify emission wavelength. As shown in Figure 7, the optical properties of ternary nanocrystals are governed by three methods - size tuning, composition tuning, and surface tuning.

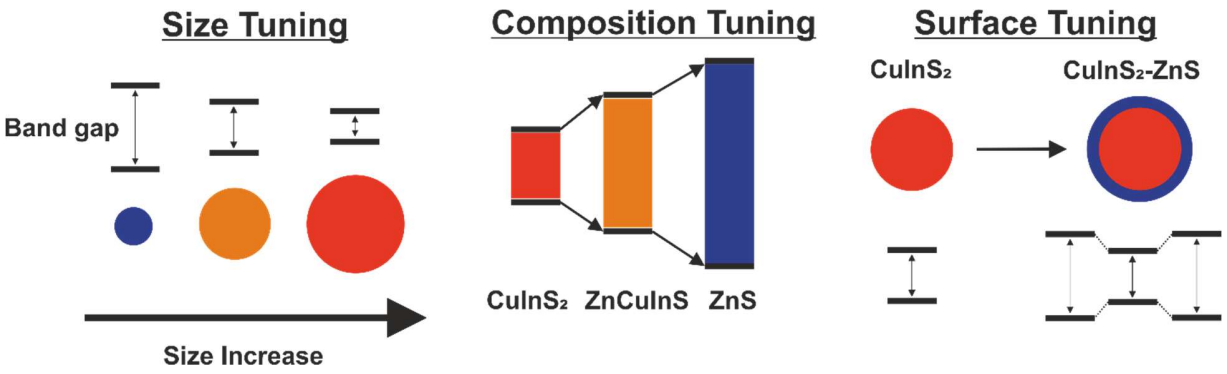

Figure 7–Schematic showing three methods where ternary nanocrystals' PL emission can be controlled. First, is size tuning, where the band gap decreases with increase in nanocrystal size. Second, composition tuning, with the addition of Zn. Third, is surface tuning, where nanocrystal PL increases and increase in band gap with the addition of shell with bigger band gap than the core. Image adapted from reference [41].

Semiconductor nanocrystals are well-known for their band-gap tuning by controlling the size of the nanocrystals; this is also noted for ternary nanocrystals. The band gap of CIS nanocrystals with a CP structure was predicted by Omata *et al*. using finite-depth-well effective-mass approximation. It was shown that the band gap can be tuned between 3.3 and 1.7 eV, with sizes in the range 1–6 nm [102]. In addition, Xie *et al*. also showed that the absorption band can be tuned from 450–900 nm with nanocrystal sizes between 2 and 20 nm (Figure 8) [90].

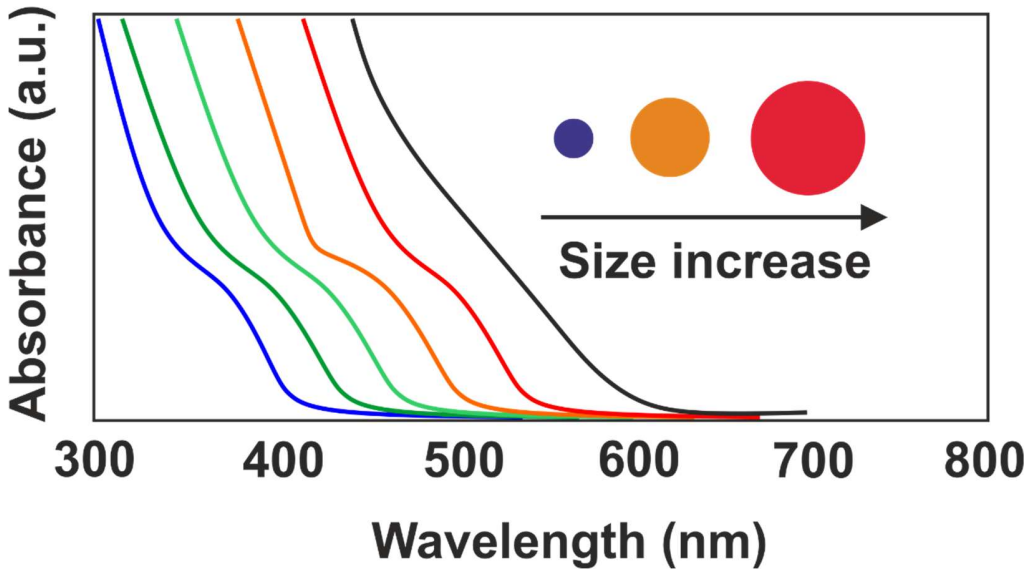

Figure 8–Shift of absorption spectra to higher wavelength with an increase in CIS nanocrystals size. Image adapted from reference [90].

Next, ternary nanocrystal composition affects the optical band gap. By changing the composition of two cation precursors, Cu and In, this affects DAP recombination, whereby the emission wavelength and PLQY can be tuned [42]. This will be further discussed in the next section.

Finally, enhanced PL emission and a blue shift in the emission spectrum are observed by over-coating the core with a larger band-gap shell (ZnS shell). The surface defects can be reduced, decreasing the non-radiative pathways. In addition, the emission can be quantised within the core by using a shell with a larger band gap. Therefore, overall PL emission increases. Furthermore, changes in core size and composition with cation exchange of Zn may affect the PL emission wavelength [103,104].

2.4.1 Effect of defects on the emission wavelength and PLQY

Defects have been shown to affect the band gap of nanocrystals (Section 2.2.3), where the emission wavelength can be controlled to increase overall PLQY. In numerous studies, it has been observed that Cu-rich species are non-emissive while In-rich species are emissive. Chen *et al.* [42] studied eight different molar concentrations of Cu/In by changing the total amount of precursor added. As portrayed in Figure 9, they observed no obvious PL emission for ratios of Cu/In at 2.9, 2.5, and 1.6, while In-rich ratios of Cu/In of 1.3, 0.8, 0.7, 0.4, and 0.3 exhibited red emission. Using PL and absorption, these samples were further examined and it was found that PLQY increased with reduced Cu/In mole ratios. The authors suggested that this was because of an increase in DAP recombination with a rise in defect concentration. However, in the Cu/In range of 0.4 to 0.3, PLQY decreased from 10.1% to 5.4%. From this observation, the authors added that there was a maximum defect concentration, where CIS can have one defect pair [$2V_{Cu}^{-}$ + In_{Cu}^{2+}] per three units of CIS (Figure 9).

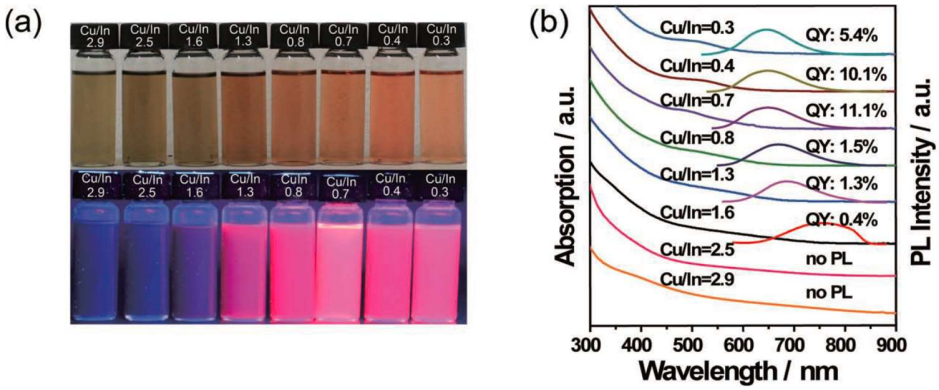

Figure 9–(a) Picture of CIS samples with different mole ratios of Cu/In under room light and UV light, (b) the graphs corresponding to the samples in (a), showing the absorption and PL emission with PLQY calculated using rhodamine B as a reference sample. Figure is reproduced from reference [42].

Similarly, Dai *et al*. investigated the effects of In/Ag ratio on the PLQY of AIS nanocrystals. As depicted in Figure 10a and Figure 10b, from absorption and PL emissions, a blue shift was noted with an increase in In content. This is explained by the band gap broadening with decreasing Ag content, as described via DAP recombination in Section 2.2.3. In addition, from viewing Figure 10c, it is seen that PL emissions increase with decreasing Ag content. With Ag/In = 0.1, PLQY was demonstrated to reach 40% PLQY without a shell or post-treatment as observed previously with CIS nanocrystals.

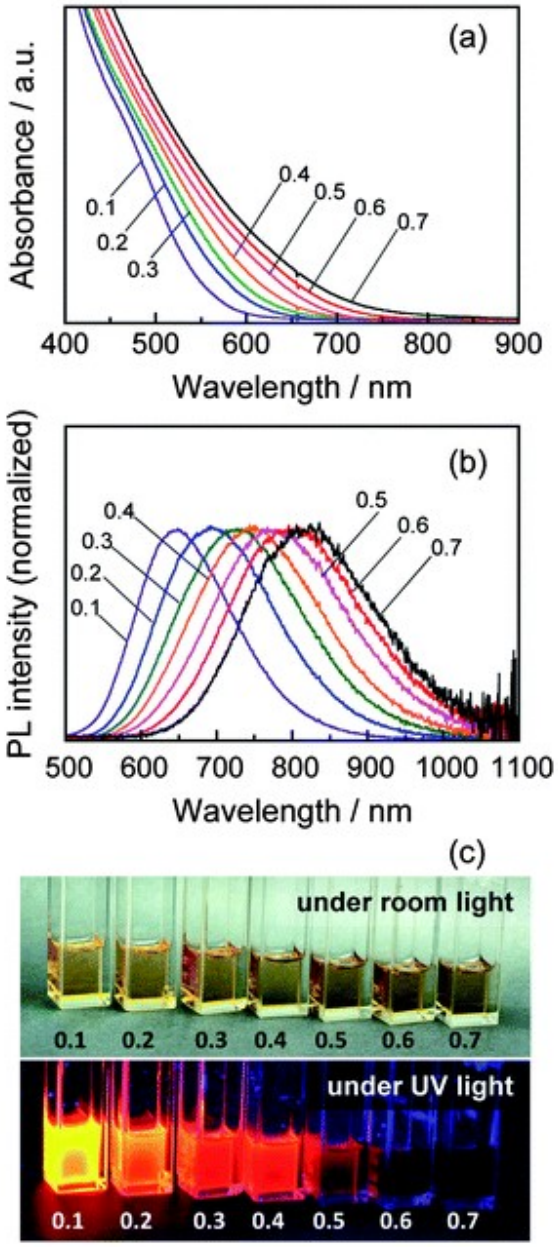

Figure 10–(a) and (b) show absorption and PL emission with different Ag/In ratios, respectively. (c) Picture of the corresponding aliquot samples under room light and UV light. As the Ag/In ratio decreases, the absorption and PL peak shifts to blue wavelength and from the picture, it shows that PL emission also decreases with increasing relative Ag content. Image reproduced from reference[101].

2.4.2 Common core–shell structure of ternary nanocrystals and the optical property effects

PL is enhanced by over-coating with a shell material that has a wider band gap than the core. This passivates the surface defects and confines the photo-excited carriers to the core. Additionally, it protects the nanocrystals from oxidation and other unwanted radiative relaxation pathways [105].

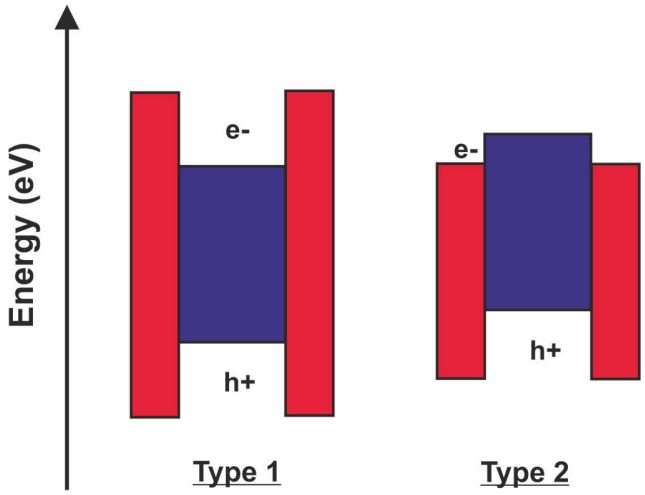

Figure 11–Schematic of two different core–shell structures. Type 1 is a shell with a bigger band gap than the core. Type 2 is a shell with a smaller band gap than the core.

Depending on the core- or shell-lattice parameters as well as band gap, there are Type 1 and Type 2 core–shell structures (Figure 11). Type 1 is usually used to passivate the surface, and improves its optical properties by confining electrons and holes to the core. In contrast, type 2 creates a staggered-band alignment, where the valence and conduction band of the core lies either higher or lower than the band edge of the shell. The shell has a smaller band gap than the core, and the electrons are confined to the shell, while holes are confined within the core, causing a significant red shift [106].

A type 1 structure is mainly employed for CIS and AIS nanocrystals. Using type 1 core–shell structure, for example for CdSe–ZnS, a red shift was observed. Yet, in the case of a CIS–ZnS shell, a blue shift minimum of 10–25 nm to 130 nm [103] has been observed.

There are two theories that explain this contrast. First, there may be a decrease in the size of the nanocrystal core through cation exchange [107], where a proportion of the outer-layer Cu and In is replaced by Zn [108]. Therefore, the CIS core size decreases and a blue shift is observed. However, the blue shift may not be simply explained by size change, as the change in absorption may [103,104] or may not [109] shift as compared with PL emission changes [60].

Second, we should consider the lattice strain on the core [78]. The lattice mismatch between the core and shell is around 3.1% for CIS-ZnS, giving rise to a compressive strain on the core, causing the band gap to increase. In the case of CdS, which has larger lattice parameters than CIS, there is a tensile stress on the core so a red shift is observed [56].

In a number of studies, it has been confirmed that PL emission is enhanced upon ZnS shell formation, and it depends on the preparation technique of just adding Zn or both Zn and S. Debate continues surrounding what actually is 'shell formation' - whether it is an actual shell formation [108] or just a cation exchange where an alloy of ZCIS is formed [110], or potentially a combination of both [60]. The analysis is challenging as the nanocrystal size is only 2–5 nm and CIS has a CP and ZnS has a ZB crystal structure, where the lattice spacing is similar, so the XRD peak positions are nearly the same.

2.4.3 Post-synthesis treatment

Torimoto *et al.* used post-synthesis heat treatment on AIS–ZnS to increase PLQY. The procedure is as follows: after the cleaning step, the nanocrystals were re-dispersed in OLA and heated to 180 °C for 30 min in a N_2 atmosphere. Various temperatures, ranging from 100 to 300 °C, were tested [111]. Figure 12 shows the absorption taken from different temperatures. It was observed that the spectra became sharper with an excitonic peak appearing, which was because of the decrease in the number of structural defects. Interestingly, the PL peak decreased at 100 °C and 120 °C. This was attributed to crystal growth on the surface of the nanocrystals at low temperatures, creating more surface defects. Temperatures of 150 °C and 180 °C removed defect sites, whereas above 180 °C, the PL peak diminished. The author explained that this phenomenon was based on the reduction of too many of the defects required for DAP recombination. From this study, it was determined that 180 °C was the optimum temperature to reach the highest PLQY, being 80%.

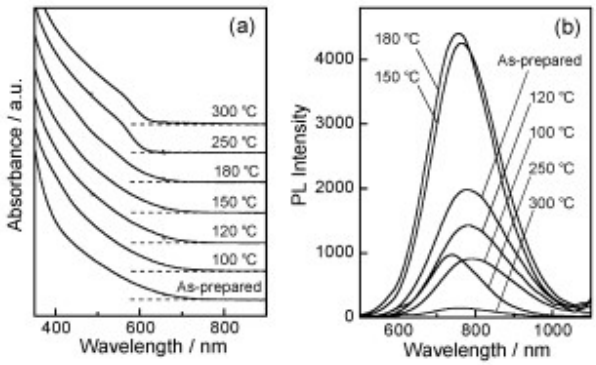

Figure 12–(a) Absorption, (b) PL emission at different heat-treatment temperatures. It shows that at 180 °C the PL value reaches the highest emission intensity, whereas the peak decreases when the temperature is further increased to 250 °C and 300 °C. Image reproduced from reference [111].

2.4.4 Halide treatment

Aside from shell passivation, another surface passivation method is carried out using halides. As compared with the bulky organic ligands that are vulnerable to oxidation and thermal degradation, halide passivation is thought to reduce surface traps without affecting nanocrystal structure [112]. This technique was first presented by Cademartiri *et al*. [113], where they used $PbCl_2$ on PbS nanocrystals. Even after several cleaning steps, through XPS analysis, there was detection of chloride ions.

Among the halide candidates, chloride, bromide, and iodide, chloride have been used experimentally the most, as it is known to be resistant against oxidative attacks [114]. Halides are also known to have a strong affinity for cations, so they can easily be exchanged and attached to the nanocrystal surface at room temperature. There are several techniques through which halide passivation is achieved. The first is using a halide precursor, such as $CdCl_2$ [115]. The second, is through utilising direct halide gas exposure [112]. Finally, using tetrabutylammonium iodide (TBAI) salts [116]. As shown in Figure 13, where Sargent's group used halide treatment, from absorption and PL, a slight red shift was observed. This may have been because of slight growth in nanocrystal size as the halide layer was built. Most importantly, they showed that there is an enhancement of the PL peak, and by using an integrating sphere, it was calculated that there was an 8% PLQY increase. In addition to this, it replaced the long-chain organic ligands. Therefore, for device applications, this would help form a compact film with better charge transport as the nanocrystal-to-nanocrystal distance decreases [117].

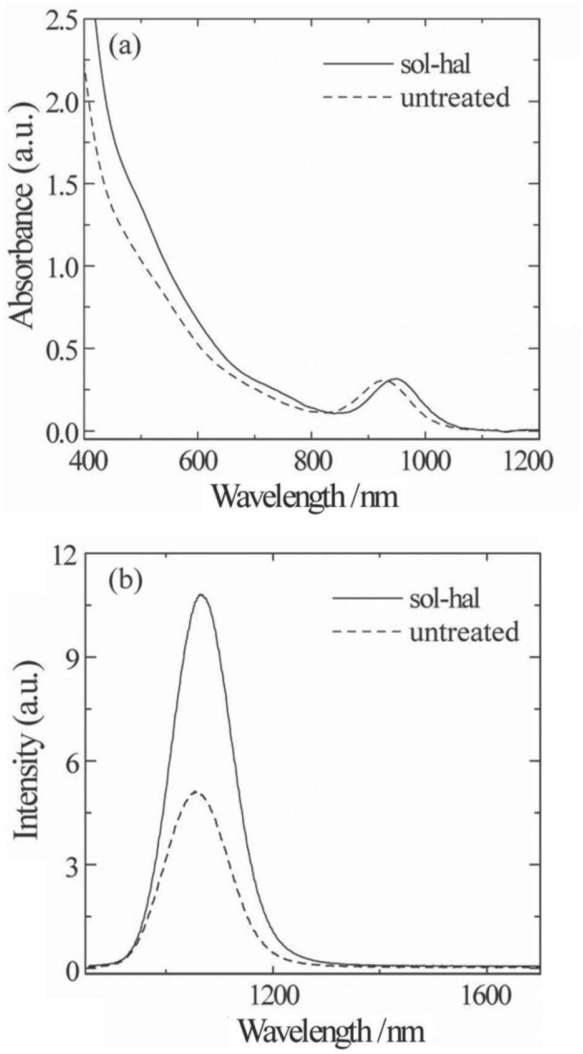

Figure 13–(a) Absorption, (b) PL; untreated nanocrystals are dotted lines. Solid lines indicate solution-phase halide treated nanocrystals. They show that PL is enhanced by 1.7 times with halide treatment. Image reproduced from reference [116].

2.5 General applications

A few of the common applications for CIS and AIS will be discussed in this section. Current applications include photovoltaics, light-emitting diodes (LEDs), and bio-imaging applications. Depending on the application, certain properties of the CIS and AIS must be enhanced. For example, with LED and bio-imaging applications, a high PLQY and low reabsorption is required. This can be attained by enhancing DAP recombination through an increase in internal defects, or using shell passivation to reduce non-radiative recombination [56]. On the other hand, for photovoltaic applications, good charge transport is necessary. Therefore, the formation of defects is avoided, and ligand exchange for shorter ligands is vital to avoiding charge insulation from occurring [90].

2.5.1 Photovoltaics

CIS–ZnS and AIS–ZnS are potential candidates for photovoltaic applications based on their tuneability of their wide band gaps of 1.52 eV [6] and 1.87–2.03 eV [118], respectively. However, there has been significant difficulty in using ternary nanocrystals for solid-state solar cells due to their poor charge transport, which is inhibited by long-chain organic ligands. Such ligands are used during synthesis for stabilisation of the solution [119]. There have been attempts to exchange these with the shorter ligand, 1,2-ethanediothiol, where mobility was improved on the order of roughly two orders of magnitude [119].

ZCIS nanocrystals have been utilised to make a quantum-dot-sensitized solar cell (QDSC). Pan *et al.* put forth promising results, where they reached the highest power conversion

efficiency (PCE) of 7.04% with Zn–Cu–In–S. The structure was a mesoporous TiO_2–ZCIS with a ZnS coating and a polysulfide as electrolyte, and Cu_2S as a counter electrode (Figure 14) [103].

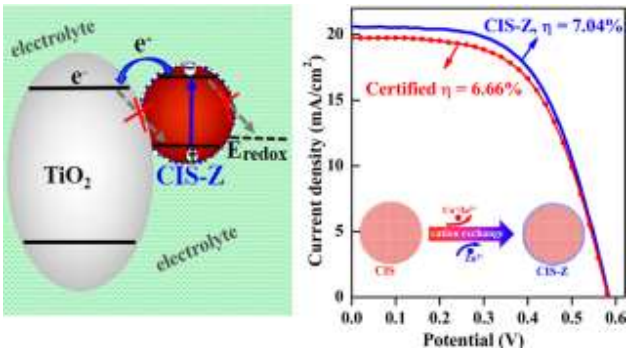

Figure 14–Quantum dot (QD) sensitized solar cell using ZCIS with an efficiency of 7.04% (certified as 6.66%). Image reproduced from reference [103].

Yao *et al.* showed the importance of ligand exchange on CIS for a dye-sensitised solar cell (DSSC). By replacing long-carbon ligands with $(NH_4)_2S$, the efficiency was improved from 1.78% to 5.78% [120].

For AIS nanocrystals, recently, Han *et al.* built a solid-state hybrid solar cell on ZnO nanotubes, reaching the highest PCE value of 2.11% with this structure. ZnO nanotubes were coated with a ZnS buffer layer, and AIS was used as a sensitizer coated on the outer layer of ZnS [121].

There have also been attempts of applications for sensitized solar cells of AIS nanocrystals. Nag *et al.,* used AIS nanocrystals for a photoanode, reaching a PCE of 0.8% [74]. In this case, the authors highlighted the importance of reducing defects for solar cell

applications. The overall short-circuit current and efficiency were both increased depending on the reduction of defects by post-synthesis annealing.

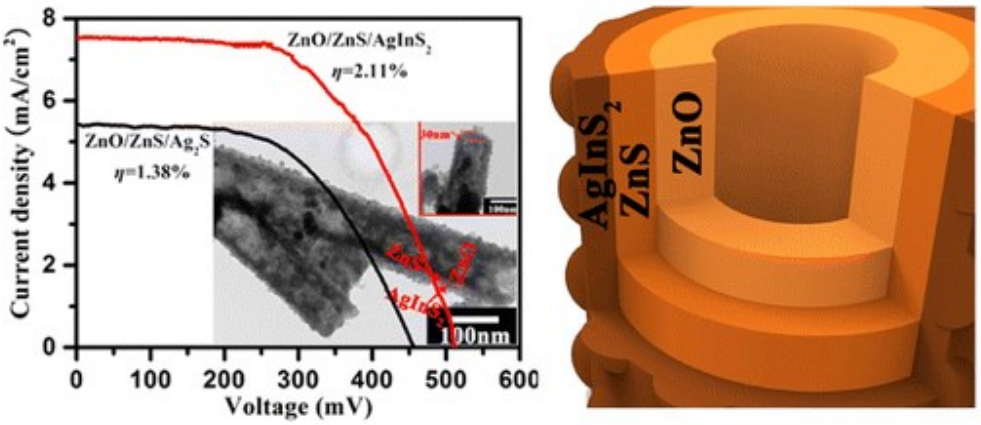

Figure 15–(a) Showing J–V curve of ZnO/ZnS/Ag_2S and ZnO/ZnS/$AgInS_2$ reaching PCE of 1.38% and 2.11%, respectively, under simulated AM 1.5 sunlight. Image reproduced from reference [121].

Jagadeeswararao *et al.* [122] have applied Ag_2S-$AgInS_2$ heterodimer nanocrystals to solar cell applications and obtained a PCE of 1.3%. The heterodimer was synthesised using a single molecular precursor by first nucleating Ag_2S and forming $AgInS_2$. From cyclic voltammetry (CV) measurements, the band alignment was of type 1, however, despite the band alignment observation of long PL lifetime, 13μS was seen. The authors believed that defects played a role in charge separation across the interface. Regardless of the band alignment, this showed that AIS nanocrystal defects affected the overall recombination pathway.

2.5.2 Light-emitting diodes (LEDs)

Semiconductor nanocrystals have generated much interest as an alternative material to fabricate LEDs for lighting and display technology as nanocrystal emission wavelengths

can be tuned and solution processed, while having a high PLQY [123]. Over the past 20 years, QD–LED has improved from less than 0.01% EQE to 18% [124]. By using nanocrystals as spectral converters, the emission from blue LEDs can be converted into other spectral colours. Through this mechanism, recently a commercial QD–LED television [124] was produced. Currently, the main semiconductor nanocrystals used are Cd-based, where there are challenges related to the toxicity of the material. Therefore, although CIS and AIS have lower colour purity than Cd-based devices, this is still a potential future material as it does not contain toxic Cd and has a large Stokes shift, which lowers reabsorption.

AIS and CIS have been especially employed for applications that include white LED [125] and flat electroluminescence (EL) devices [126,127]. EL devices with the colours green to deep red were created by ZnCuInS/ZnSe/ZnS structures or $CuInSe_2$/ZnS nanocrystals sandwiched between ITO and an aluminium electrode with organic electron and hole transport layers. The results featured a maximum luminance of 2100 cd/m^2 for yellow and 1700 cd/m^2 for red, which are still much lower than Cd-based nanocrystals.

By mixing ZnCuInS/ZnS (red) with a blue-green emissive polymer, a white LED was built with a colour rendering index (CRI, R_a) of ~92 [128]. Alternatively, a blue-emitting chip was coated with red and green CIS nanocrystals to create white light, where a CRI of 72–75 and a luminous efficiency up to ~60 lm/W was yielded [125,129].

2.5.3 Bioimaging application

As of this moment, the most popular materials for *in vitro* and *in vivo* bioimaging are Cd-based nanocrystals or organic dyes as they possess a high PLQY [130]. Cd nanocrystals have

become more desirable over organic dyes owing to their broad absorption spectrum, narrow PL emission, high PLQY ~90% [131], and stability under light irradiation [6]. This leads to higher sensitivity and multiplexed detection, where different PL colours can be observed with a single excitation [132]. CIS and AIS have similar properties but with additional unique advantages, such as long PL lifetime, which can be used to increase the delay time between photoexcitation and detection. Therefore, they could reduce background autofluorescence [133].

The challenge faced for *in vitro* and *in vivo* imaging is that nanocrystals need to be hydrophilic. However, most nanocrystals are hydrophobic because of the hydrophobic organic ligands used during synthesis. Therefore, new synthesis methods utilising hydrophilic ligands [134] or post-synthesis ligand exchange [135] have been reported. Although CIS and AIS are less toxic for humans as they do not contain Cd for bio-labelling, there are still the remaining elements, such as Ag, Cu, In, and S, that are toxic to human physiology. Therefore, encapsulating the nanocrystals is crucial. However, it has been observed that through ligand exchange and encapsulation, the overall PLQY efficiency is decreased because the process may form defects on the surface.

The most prevalent encapsulation methods make use of polyethylene glycol (PEG) [136], dihydrolipoic acid (DHLA) [137], DNA passivation [138], or a combination of several different polymers. Aside from protection from toxic elements, encapsulation prevents nanocrystal aggregation, enhances stability, and protects the nanocrystals themselves from chemical attack within an *in vivo* environment.

Reiss *et al*. used DHLA to cap CIS/ZnS [107]. Pons and his group employed DHLA–PEG and micelle encapsulation to coat CIS/ZnS to further reduce toxic contact [135]. Others have made use of PEGylated phospholipid-encapsulation instead, such as Prasad and co-workers [139], for CIS/ZnS and Searson's group [140] did so for Cu–In–Se/ZnS nanocrystals.

2.6 Luminescent Concentrator

2.6.1 What is a luminescent solar concentrator and visible light communication?

Luminescent solar concentrator (LSC)

With the long-term increase in fossil fuel prices and environmental concerns, the need for renewable energy has increased. However, solar energy falls behind as an energy source in terms of cost and efficiency. In the late 1970s, luminescent solar concentrators (LSC) were proposed as a method to decrease the size of PV cells by capturing light from a large area and channelling it to an edge[141,142,143]. The first generation of LSC used a fluorophore or semiconducting nanocrystals embedded in a transparent polymer substrate with a PV cell attached at the side, as shown in Figure 16.

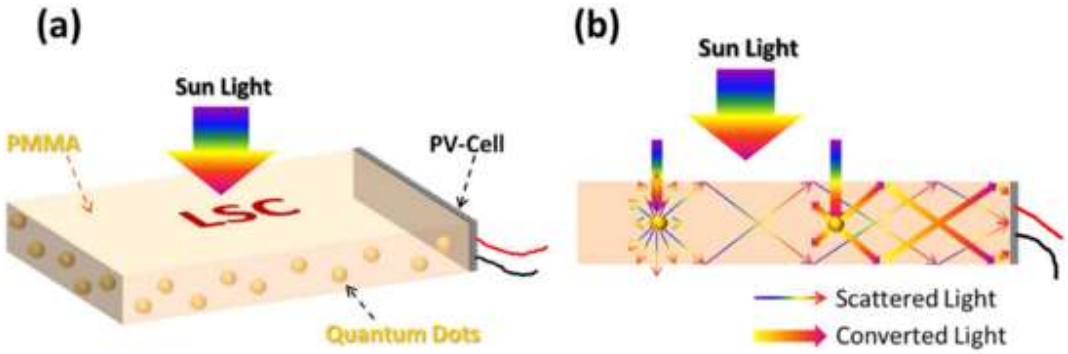

Figure 16-(a) Schematic of a flat QDs LSC (b) Showing how light passes through the LSC and reaching the edge where there is a PV cell. Image reproduced from ref [10].

The incoming light is absorbed by a fluorophore and emitted at a longer wavelength where it's guided to an edge where a photovoltaic cell is attached. For optimum performance, the fluorophore is chosen to have a high photoluminescence quantum yield and a large Stokes shift to minimize reabsorption. By tuning the fluorophore emission

wavelength, the LSC can be optimised to ensure that the PV cell has the highest external quantum efficiency [144].

Early LSC used organic dyes and reached an average panel efficiency of 7.1% and a geometrical gain of 10 (short circuit current was increased by 26%) [145]. Liu *et al*. improved this result by using multiple organic dyes to enhance absorption across the solar spectrum, reaching an efficiency up to 16.7% [146]. Use of quantum dots instead of organic dyes has the advantage of a larger absorption range, tuneable emission with size, longer photo-stability, and larger Stoke-shifts. Meinardi *et al*. demonstrated the first use of a core/shell CdSe/CdS QD-based LSC, which reduced the reabsorption effects [147]. Wilton *et al*. used PbSe QDs and lowered re-absorption further by utilising Förster resonance energy transfer between two different QDs sizes [148]. These efforts have contributed to making a viable QD LSC, but Cd- or Pb- based QDs are toxic. Thus, there is a need to find safer alternatives. Li *et al*. showed a toxic-free LSC using $CuInS_2$/ZnS, which reached a PCE of 8.71% attached to a c-Si PV cell [10].

Förster resonance energy transfer (FRET) is a method that can be used to enhance the efficiency of LSC. FRET is a non-radiative energy transfer, whereby light absorbed by a donor fluorophore is transferred to an acceptor fluorophore. However, FRET is sensitive to distance, as the energy transfer is inversely proportional to the sixth power of distance between donor and acceptor. Therefore, this method is only useful if the fluorophores are in close proximity, i.e. less than few nanometres apart. FRET has been applied in LSC where donor and acceptor fluorophores are coated next to each other [149, 150].

Visible light communication (VLC) concentrator

The increase in electronic devices, such as smartphones and tablets, has increased the need for high-speed data communication pathways. However, there is only a limited range of radio frequency available. To solve this problem, researchers have started considering next-generation communication technology such as visible light communication (VLC). VLC works by encoding data into a modulated light source, such as an LED, and uses a photodetector as the receiver [151].

Tanaka *et al*. first saw the potential of VLC as an alternative route for data transfer by using the unexplored visible spectrum [152]. The main advantage of VLC over RF communication is the availability of a larger bandwidth range. The VLC bands between 400,000 GHz to 750,000 GHz provide more accessibility than the radio frequency bandwidth, which is 3 kHz to 300 GHz [153].

Figure 17, compares how data is transferred in conventional RF and VLC. VLC is a much more secure method of data transfer. This is due to the physical characteristics of light wavelengths, which cannot propagate through a wall. In addition, light sources are abundant so any sources of light such as traffic lights or home lights could be a source of data.

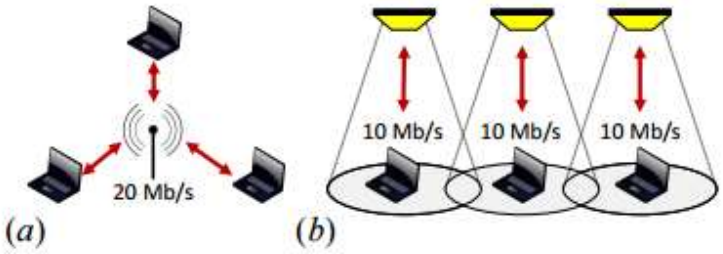

Figure 17- Image showing a comparison of (a) conventional data transfer method and (b) VLC method. This image presents the limitation of VLC technology. Where VLC is restricted to the area where light is shined. On the contrary shows the advantage, where light constraint to an area can be a safe method for data transfer. In addition, any source of light, such as room light, can be used to transfer data, increasing its feasibility. Reproduced from Rahaim et al. [154].

The efficiency of a VLC is limited by the size of the photodiode and directionality of the light signal. Typically, near-commercial systems have used large photodiodes to maximise the efficiency of signal detection. However, large photodiodes have the disadvantage of inducing a high capacitance, which would result in a large signal-to-noise-ratio (SNR) and lower the overall bandwidth (speed of data transfer) [155]. Therefore, to keep a high bandwidth, a smaller photodiode is preferable, but this would then decrease detection efficiency. A solution to this problem is to use a luminescent concentrator, as shown in Figure 18. The concentrator will absorb light from a large area while concentrating the light emitted at the edges. Thus, the photodiode can be kept small.

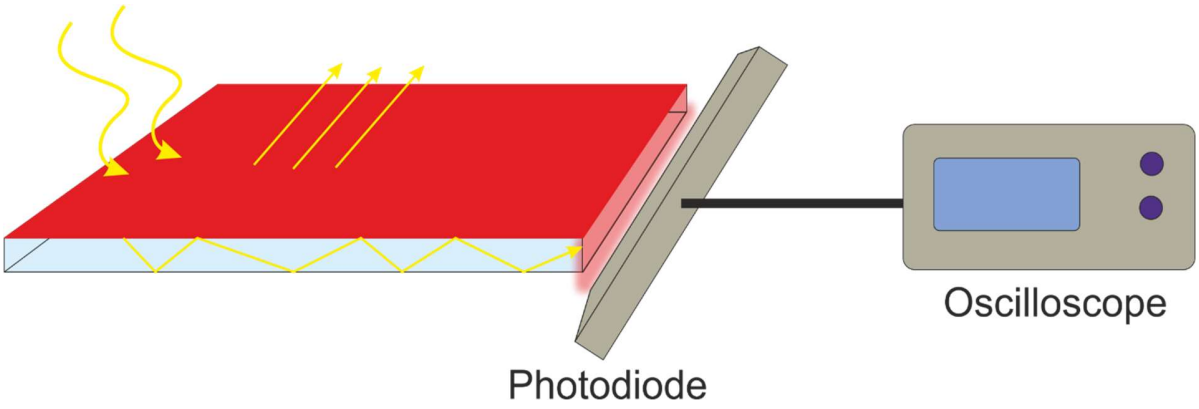

Figure 18- Simple schematic of a concentrator connected to a photodiode. Light is absorbed in the large concentrator area and transmitted to the edges where the photodiode detects the signals. Some light is lost through reflection and scattering.

The concept of a luminescent concentrator (LC) for VLC was developed in Oxford by Profs Collins, O'Brien, and Watt [156]. Recently, Collins *et al*. used Coumarin 6 as the fluorophore mixed with epoxy placed between two glass substrates, and has shown a 10-fold effective photon concentrating factor (EPCF) [13]. Based on the literature review, to our knowledge, there has not been a concentrator for VLC using semiconductor nanocrystals published.

2.6.2 The mechanism of luminescent concentrator

A luminescent concentrator (LC) is a planar waveguide that has the following structure: substrate, layer of luminescing material and a layer polymer for protection. Three stages are important to the LC include absorption, trapping, and emission. The incident light is absorbed by a luminescing material, and is trapped by total internal reflectance (TIR), and finally emitted to the edges. The performance of a LC is known as the gain, and it is calculated by the detection of light emitted at the edge (of the concentrator) to a single photodiode. (Section 6.2.3 gain measurement).

When light hits the surface of the concentrator, it will react as shown in Figure 19; Rayleigh scatter, Mie scatter, transmit, reflect, or be absorbed by nanocrystals and re-

emit. The light that is detected at the edge of a concentrator is either light that has been re-emitted and undergoes TIR, or the light that is scattered by a luminescing nanoparticle close to the edge.

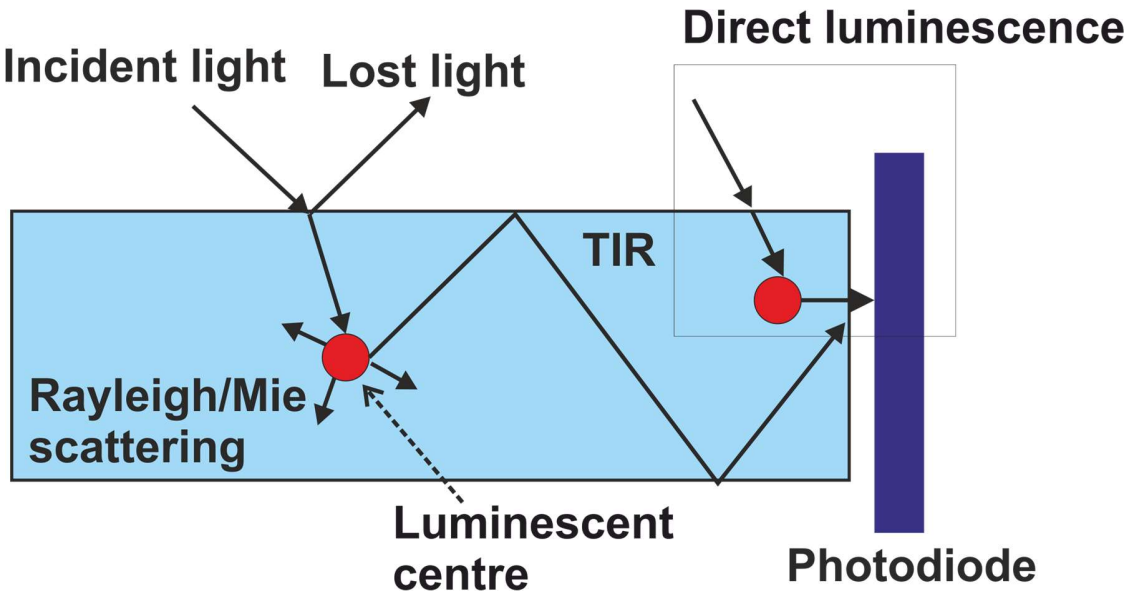

Figure 19- Schematic showing the mechanism of a concentrator. Incident light is transferred to the edge of the concentrator by emitted light from the nanocrystal, directly, or by total internal reflectance. Remaining light is regarded as being lost.

Emission and re-absorption

The luminescing layer (nanocrystals) will absorb light and then emit. The emission intensity depends on the PLQY of the nanocrystals, while the emission wavelength will depend on the optical characteristics of the nanocrystals. In order to achieve a high gain (luminescence at the edge), a high concentration of nanocrystals is favourable. If the emitted light has sufficient energy, this may lead to re-absorption by the neighbouring AIS nanocrystals. To avoid this type of re-absorption, using a nanocrystal with large Stoke shift is beneficial.

Total internal reflectance (TIR)

When incident light is absorbed and emitted by the nanocrystals, it is retained in the concentrator layer and further carried on to the edge by total internal reflection (TIR). TIR occurs when an incident light at the interface is at an angle larger than the critical angle with respect to the normal direction from the surface. By rearranging Snell's law, the critical angle equation is,

$$\theta_{critical} = \sin^{-1}\frac{n_r}{n_i},$$

where, n_i and n_r are the refractive indices of the incident medium and refractive medium, respectively. TIR occurs when incident light travels from an area of high refractive index to one of low refractive index; thus, n_r/n_i <1. The higher the refractive index of the luminescing layer is, the lower the critical angle; hence, the higher the probability of the light to be a TIR. Using a base polymer with refractive index greater than 1.5 will be sufficient for TIR, since adding a luminescing particle further increases the refractive index. The change in refractive index of a polymer with luminescing material can be measured using a refractometer.

Rayleigh & Mie scattering

Light is scattered within the concentrator layer due to Rayleigh scattering. It is an elastic scattering of light or electromagnetic radiation by spherical particles in a medium much smaller than the wavelength of radiation. The conditions for Rayleigh scattering are determined by the expression,

$$x = \frac{2\pi r}{\lambda},$$

, where r is the radius of the spherical particle, and λ is the wavelength of the incoming light. If $x << 1$, then Rayleigh scattering occurs [157]. The incident and re-emitted radiation has the same property, but the direction of propagation is altered.

Light can also be scattered by Mie scattering, which is due to particles similar to or larger than the wavelength of the incoming radiation. Mie scattering is also an elastic scattering which originates from the difference in refractive index between the particle and the medium. Therefore, scattering can be controlled by the particle's size, shape, and density. Here Mie scattering will not cause a significant effect as the particles are much smaller than the wavelength of the incoming radiation [158].

2.6.3 Material criteria for VLC concentrator

The concept of luminescent concentration for solar and communication purposes is quite similar in the sense that they both need a fluorescing material that guides light to the edges, but the requirements for each application are slightly different. LSC requires broad solar spectral absorption while VLC concentrator needs to rapidly absorb a modulating light source and transfer it to a detector at a single wavelength. Therefore, a narrow absorption wavelength is acceptable for VLC as it can be made to detect a specific wavelength depending on the LED source. Key requirements for LSC and VLC are summarised in the table below (Table 3).

Table 3- Summary of material characteristics required for LSC and VLC

Luminescent solar concentrator	**Visible light communication**
1. Large absorption wavelength (200nm – 600nm)	1. Short PL lifetime (<100ns)
2. Large Stoke shift (>100nm)	2. Large Stoke shift (>100nm)
3. Photostability	3. High PLQY

Organic dyes are a popular choice for VLCs due to their high PLQY and short PL lifetime [159]. AIS nanocrystals have PL lifetimes two orders of magnitude longer than dyes but have much better photostability and optical linearity in different solvents [159]. Most importantly, AIS nanocrystals have larger Stoke shifts, therefore reabsorption is minimal. For example, Coumarin 6 has been used in a prototype VLC concentrator and has an 80% PLQY in ethanol [160] and PL lifetimes of 3.5ns. However, the Stoke shift is only 50nm [161], which leads to considerable re-absorption. AIS nanocrystals, on the other hand, have an average Stoke shift of 150nm, but have PL lifetime of 350ns [69]. The long PL lifetime of AIS is a result of DAP recombination. However, there is still an opportunity here to reduce the PL lifetime by controlling the amount and nature of internal defects while maintaining the PLQY value by using methods such as shell or post-treatments with halides or ligands [148].

The AIS nanocrystals used here are from Chapter 5, which have long-term PL stability under ambient conditions of 89%. An average Stoke shift of 130nm and PL lifetime of 320ns was measured.

2.7 Conclusion

This chapter reviewed the literature on the two ternary nanocrystals, CIS and AIS. Both ternary nanocrystals have similar general properties and crystal structures. The main properties highlighted were large Stokes shift, wavelength tuning from NIR to visible, and stoichiometry control of PL wavelength and PLQY.

The synthesis of CIS was developed from binary nanocrystal synthesis and further improved to formulate AIS synthesis methods. However, unlike binary synthesis, ternary nanocrystals involve two cation precursors with different Lewis acid characteristics, thus control of reactivity was challenging. As a solution to this, the use of different combinations of ligands from X and L groups at different reaction temperatures offered an encouraging route.

The recombination pathway for ternary nanocrystals is complicated compared with the binary nanocrystal recombination pathway of CB to VB. Three main theories have been considered in the literature. The most recognised theory would be DAP recombination, which involves donor and acceptor defect states. However, through PL lifetime studies, others suggested that CB and VB also play a role with the inter-defect state. Although extensive research has been conducted by several groups, the debate continues surrounding the mechanism behind the recombination pathway.

Whether or not the mechanism is DAP recombination or if other band states play a role in recombination, ternary nanocrystals have shown that changes in stoichiometry affect the PL emission wavelength and the overall PLQY. It has been observed for both CIS and AIS that an increase in In content affects the blue shift in PL and increases the PLQY.

Other methods to increase PLQY are over-coating the nanocrystals with a shell layer or the use of halides. The most frequently used shell material is ZnS with a higher band gap than CIS and AIS. By overcoating with a shell, the surface defects are reduced and the electron combination is confined within the core, resulting in an increase in the PLQY. Similar effects have been observed with halides. In particular, chloride ions were the most effective of the halides. Halides have an additional advantage of acting as a ligand exchange mechanism, which has been demonstrated to form a more compact film.

Finally, various applications that have made specific use of CIS and AIS were discussed, primarily photovoltaics, LEDs for lighting and displays, bioimaging, and LC. Although the PLQY may be lower than Cd-based nanocrystals, ternary nanocrystals have the benefit (over Cd nanocrystals) that they are less toxic and have a large Stokes shift. To emphasise, ternary nanocrystals have been investigated for less than two decades. Considering the short period, they have shown a very promising future. Moreover, there is still much room for improvement and greater understanding.

Chapter 3 -Experimental methods

3.1 Introduction

This chapter focuses on providing supporting elements for Chapter 4 and 5 results and discussion section. Here, the general synthesis procedure for CIS and AIS nanocrystals are explained and characterisation methods used throughout the two chapters are summarised.

3.2 Synthesis techniques

All the synthesis procedures were conducted using a three-neck-flask connected to a Schlenk line. The synthesis procedure used within the thesis is similar to a hot-injection method that was introduced in Chapter 2. The main difference however, was the use of a low injection temperature. As the quantities and precursors vary throughout the chapters, for simplicity, details are included in each chapter.

3.2.1 Materials

All chemicals were used without purification. The precursors used are as follows: Cu(Ac) (Aldrich 97%), CuF_2 (Aldrich 98%), CuCl (Aldrich ≥ 99.995%), CuBr (Aldrich 98%), CuI (Aldrich 98%), $In(Ac)_3$ (Aldrich 99.99%), InF_3 (Aldrich ≥ 99.9%), $InCl_3$ (Aldrich 98%), In Br_3 (Aldrich 99%), InI_3 (Aldrich 99.998%), AgCl (Aldrich 99.999%), AgBr (Aldrich 99%), and ZnSt (Aldrich) . Other reagents used are Bis(trimethylsilyl) sulphide, TMSS (Aldrich) and 1-octadecene, ODE (Aldrich 90%) and Oleylamine, OLA (Fishers 80-90%).

3.2.2 Nanocrystal synthesis (CIS and AIS)

The reagent quantity used are summarised in Table 4. First, Cu/Ag and In precursors, with ODE, OLA, and OA were prepared in a three-neck flask. Figure 20, shows the main

steps of the synthesis. Step one, the precursors, ligands, and solvents were degassed at 100°C, to remove any impurities such as water. Step two, the temperature was increased to 180°C, to reduce all the precursors. Step three, the solution was cooled to the injection temperature, afterwards TMSS was injected. Upon injection, the solution turned black. Finally, the temperature was raised to 130°C. As the temperature increased, the solution turned red. When 130°C was reached, the solution was left for 5 mins, then heating was switched off and left to cool at room temperature for 30 mins.

Table 4- Summary of the reagent quantity used.

Reagents	**Quantity (mmol)**	**Quantity (g)**
Copper/Silver	Varies throughout experiment	
	0.25	0.03
Indium	Varies throughout experiment	
	1.00	0.29
Oleylamine	10.00	5.35
Oleic acid	5.00	1.41
1-Octadecene	30.00	7.54
Bis(trimethylsilyl) sulphide (TMSS)	1.50	0.29

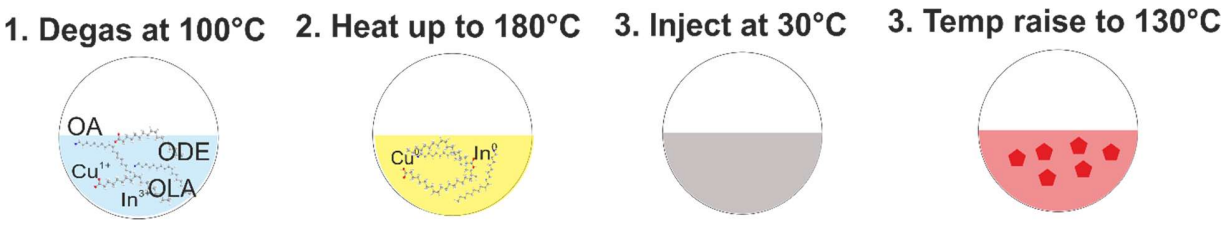

Figure 20- Schematic summarsing the full synthesis steps

3.2.3 Nanocrystal cleaning

After cooling the solution, it was transferred to 50ml centrifuge tubes. 30ml of ethanol was added and mixed to precipitate the nanocrystals. The mixture was centrifuged at 3000 rpm for 10 mins. This procedure separated the nanocrystals and excess solvent/unreacted precursors. The supernatant solution was poured away, and 5ml of hexane was added to re-disperse the nanocrystals. This cleaning step was repeated twice (based on the observations whilst preforming TEM imaging) to fully remove the excess ligands. When an additional cleaning step was taken, it was observed that the nanocrystals do not fully re-disperse when a non-polar solvent was added. This implied that too many ligands were removed. The final solution was transferred to a glass vial.

3.2.4 CuInS2-ZnS synthesis

After the final cleaning step of CIS nanocrystals, for precipitation, 30ml of ethanol was added. The supernatant was removed, and the remaining nanocrystals were dried in air for 30mins. This procedure was to remove any remaining solvents. Afterwards, Zinc stearate, OLA, OA, and ODE were added (in quantities as summarised in Table 5) and shaken, then transferred to the three-neck-flask.

The solution was degassed under vacuum at 100°C for one hour, to evaporate remaining solvents, such as hexane and ethanol. The flask was purged with argon, and TMSS was injected, and the temperature was raised to 180°C and left for two hours. During the two hours, the argon gas flow was controlled to a minimum level to avoid any OLA, OA, and ODE from evaporation. The solution colour changed brighter over the course of time, indicating a successful zinc shell formation. Finally, the solution was cooled to room temperature and, the nanocrystals were cleaned as described in Section 3.2.3.

Table 5- Summary of the reagents and quantity used in moles

Reagents	**Quantity (mmol)**
Zinc stearate	2.00
Oleylamine	10.00
Oleic acid	5.00
1-Octadecene	30.00
Bis(trimethylsilyl) sulphide (TMSS)	1.50

3.3 Characterization

3.3.1 Transmission Electron Microscope (TEM)

Using the JEOL-2200MCO FEGTEM, an aberration-corrected microscope, high-resolution TEM images with clear lattice planes were imaged at 80KV at high magnification >1Mx. The size distribution was measured at low magnification. For TEM sample preparation, nanocrystals were diluted in hexane to achieve a well-dispersed formation on the TEM grid. The samples were prepared by slowly dipping the graphene oxide (GO) support film on a lacey carbon Cu grid (from Agar scientific) into the nanocrystal solution. The grids were heat treated overnight under vacuum at 150°C to remove any excess organic material.

3.3.2 Scanning Transmission Electron Microscopy (STEM)- Energy Dispersive X-ray Spectroscopy (EDS/EDX)

STEM-EDX was used to analyse the composition of the nanocrystals. By bombarding high energy electrons, the atoms are excited to a higher energy level, and upon relaxation, X-rays are emitted. The detected radiation has specific energy values that correspond to a certain element. EDX will measure the elements present within the TEM grid, and the

composition of the nanocrystal sample can be predicted by using the count ratio after removing the background artefacts. Longer the count time, it helps decrease the statistical scatter of the background radiation. Also, INCA software used for EDX measurement has a filtering method that helps identify the energy peaks while reducing the background.

Using JEOL-2100 with LAB_6 source, STEM dark field imaging was carried out and EDX analysis of both mapping and point measurement was conducted. Nanocrystal solutions were prepared as depicted in Section 3.3.1. The grid used here was carbon film on 300 mesh gold grids (from Agar scientific), since CIS nanocrystals contained copper, graphene oxide (GO) could not be used. Also, a beryllium double tilt holder was used to avoid any copper detection from the holder.

3.3.3 X-Ray Diffraction (XRD)

XRD analysis studies the phase of the nanocrystals by using diffracted X-rays. It can be used to identify unit cell dimensions and crystal structure. Using the Scherr equation, an approximate size of the nanocrystals sample can be calculated. XRD was performed by Philips PW1820 system with PW1727 X-ray generator using Cu Kα radiation (λ = 1.5418 Å). XRD samples were prepared by drop casting a concentrated solution of nanocrystals onto a cleaned cut glass of size $5cm^2$. Thick film layer was important to avoid any interference from the underlying glass substrate.

3.3.4 Photoluminescence (Quantum Yield measurement)

Photoluminescence is a technique that detects light emission of a sample excited by a laser/LED. The light source should be within the absorption wavelength range of the

material. In the case of CIS and AIS, due to its broad absorption, the wavelength of the LED used was dependent on the reference sample peak excitation wavelength for photoluminescence quantum yield (PLQY) measurement. Here, LED of 530nm (green) from Thorlab (Fiber coupled Led, 1000mA, 4.0mW) was used. Detection was done USB4000-FL spectrometer coupled with fibres. (As shown in Figure 21.)

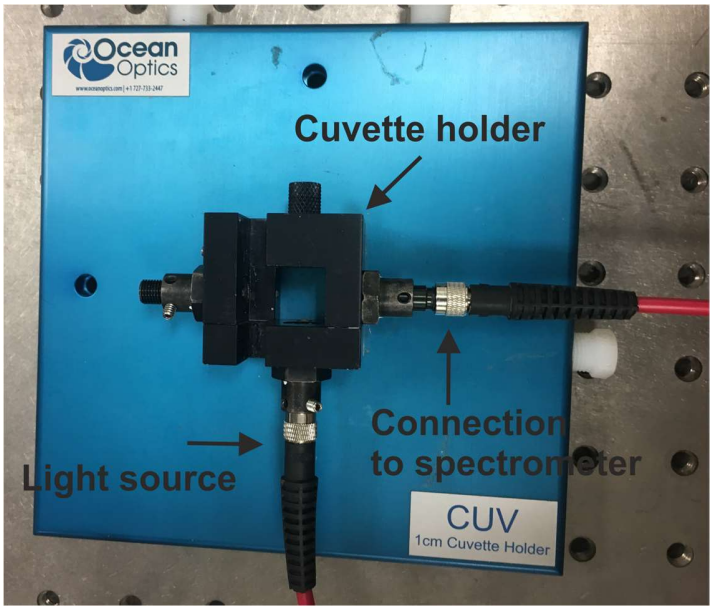

Figure 21- Picture showing the set-up for photoluminescence measurement

PLQY quantifies the ratio of photons absorbed to photons emitted. A comparative method developed by William *et al.* [162] was used which involved the use of a standard reference sample with a known PLQY value. Therefore, the result was independent of the wavelength used, as the reference sample PLQY was adjusted accordingly based on the change in ratio of the peak emission wavelength to the wavelength used for measurement. However, a standard reference sample should be selected with absorption spectrum within the absorption range of the sample being tested. Here, Rhodamine 101 (Aldrich) was used which has an excitation wavelength of 265~563nm, and emission at ~588nm

in methanol, and it reaches maximum PLQY 96% at its excitation wavelength [163]. Using ratio of PL peak change from peak excitation point to the experimental wavelength (530nm) the average PLQY of Rhodamine 101 was found to be 88%.

The following steps were taken for PLQY measurement:

1) 4 different samples with absorbance value 0.02, 0.04, 0.06, and 0.08 of each nanocrystal and standard samples were prepared. The overall absorbance should not exceed 0.1 as beyond this level, non-linear effects may be observed due to inner filter effects.

2) For each sample absorption and PL emission was measured.

3) Each of the area under the PL curve, which is the total PL, was calculated by integration.

4) PL value was plotted against its corresponding absorption value at 530nm. Linear fitting was made to measure the gradient (Figure 22).

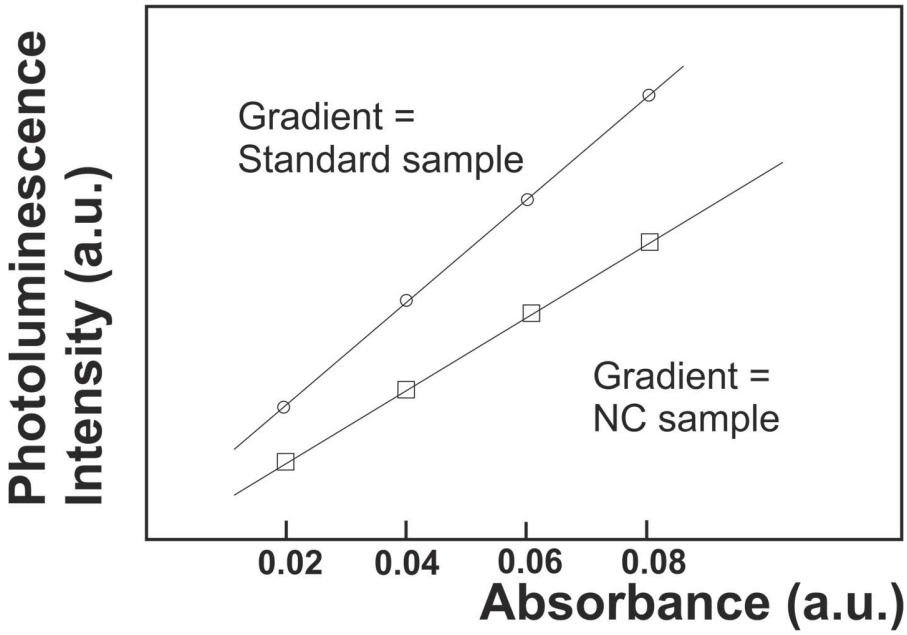

Figure 22- Schematic showing linear fitting of PL against absorption to calculate the gradient for standard sample and NC sample

5. Finally, PLQY was calculated using the equation below where n, is the refractive index of the solvent, and ϕ is the PLQY value.

($n_{Standard\ sample\ solvent}$ is methanol: 1.33, $n_{NC\ solvent}$ is hexane : 1.37, ϕ standard sample rhodamine 101: 88%)

$$\phi_{NC\ sample} = \phi_{Standard\ sample}\left(\frac{Gradient_{NC\ sample}}{Gradient_{Standard\ sample}}\right)\left(\frac{n^2_{NC\ solvent}}{n^2_{Standard\ sample\ solvent}}\right)$$

$$\phi_{NC\ sample} = 88 \times \left(\frac{Grad_{NC\ sample}}{Grad_{Standard\ sample}}\right)\left(\frac{1.37}{1.33}\right)^2$$

3.3.5 *In-Situ* Photoluminescence

In-situ PL is a dynamic PL method, where it is used to detect the changes in PL emission throughout a synthesis procedure. The advantage of this technique is that PL can be

measured in Ar gas filled atmosphere, and nanocrystals cleaning process can be avoided. Therefore, more precise understanding of the changes in PL can be measured.

Using the spectra-suit program provided by the spectrometer, a PL measurement can be taken every 10 seconds. Simultaneously, using a time logger thermocouple, change in temperature with time can be measured. *In-situ* PL is measured by using a fibre optic probe (Thorlabs) that has 3 legs for light source, signal detection, and spectrometer (Figure 23). For light source, 420nm- blue LED was used to observe stronger PL curves. The schematic of the full set-up is shown in Figure 24.

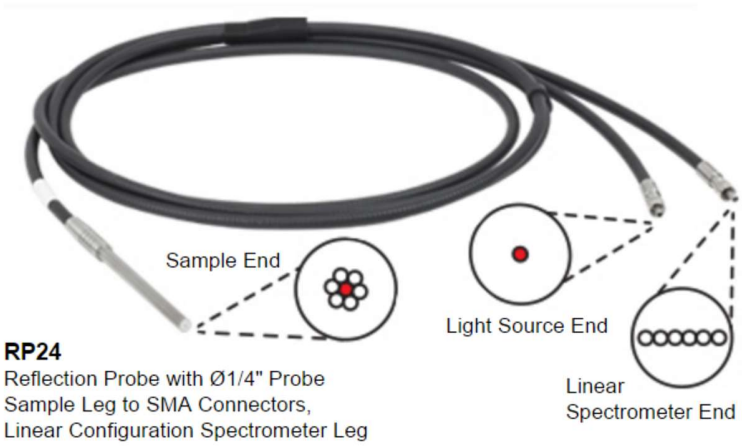

Figure 23- Picture taken form Thorlab website showing the image of the in-situ probe used. End of the probe is both fitted with a light source, and spectrometer, therefore, can simultaneously emit the NCs and measure the reading.

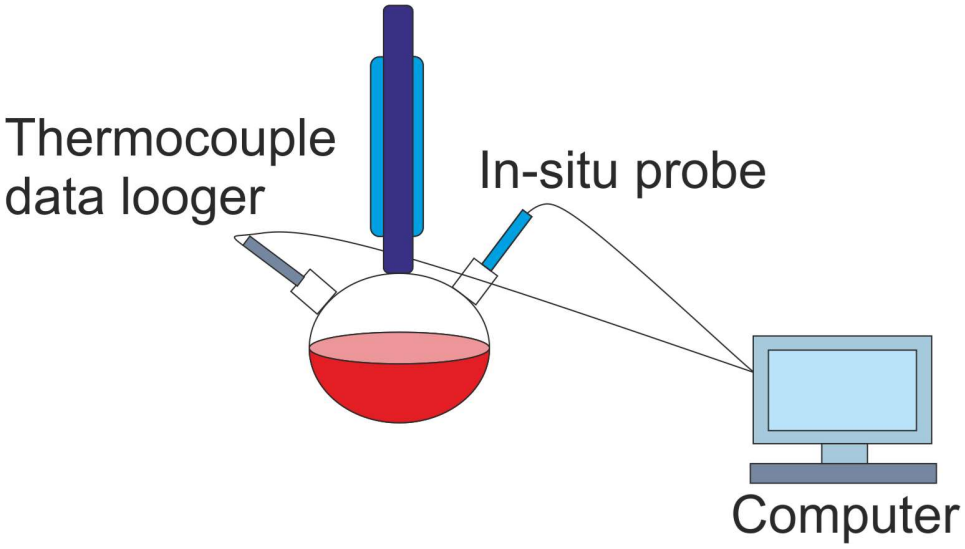

Figure 24- Schematic of the in-situ PL set up. The three neck flask is fitted with in situ probe and thermocouple data logger, which are connected to a PC that stores the temperature and PL intensity measurements.

3.3.6 UV-Vis Absorbance measurement

UV-Vis is an optical spectroscopy that provides information about excitation of electrons of the material, from which the band gap can be calculated. The absorption spectrum of UV to visible was measured by shining light at different wavelengths, and measuring the amount of light that has not been transmitted, relative to the transmittance of a blank reference sample.

All absorption measurement was carried out using Cary Varian 5000. Each sample was prepared by diluting the nanocrystals with hexane. A reference sample of hexane was prepared to deduct the absorption values.

3.3.7 PL lifetime

PL lifetime measurement was conducted by Sam Johnson, using a confocal microscope with x60 objective lens (Nikon 0.7NA). Samples were tested in solution and in the solid-state after drop casting onto a fused silica substrate. For excitation, a 532nm pulsed laser

(Fiannium SC400) with 100 kHz repetition rate was used. Emission was collected onto a single photon avalanche photodiode (Perkin-Elmer SPCM). The statics for lifetime calculation was built by time-correlated single-photon counting module (Edinburgh Instruments T900).

Chapter 4 - $CuInS_2$ and $CuInS_2$-ZnS: Modification of synthesis procedure and halide precursor study

4.1 Introduction

Following on from the various synthesis methods introduced for ternary nanocrystals in Chapter 2, this chapter focuses on modifying the hot-injection synthesis method to yield monodispersed nanocrystals with high PLQY. This can be achieved by modifying synthesis conditions, such as injection temperature, precursor ratio, and precursor combinations.

One of the main limitations of CIS synthesis is controlling the relative reactivity of Cu, In, and S precursor materials to achieve well-dispersed nanocrystals with a homogeneous crystal structure and stoichiometry. Typically CIS synthesis involves the use of 1-dodecanthiol (DDT) [41], a 12-carbon long chain ligand that acts as both a sulfur precursor and surfactant. DDT attaches to the nanocrystal surface through covalent bonding, thus passivating the surface and solubilising the product. The nanocrystals formed by this route tend to be very stable [15]. However, this passivation behaves also as an insulating layer that limits charge carrier transport between nanocrystals [117]. Ligand exchange has been attempted for device fabrication, but as DDT is covalently bonded to the nanocrystals, ligand exchange is not easy to initiate as a process [92].

Herein, DDT is replaced by a much more reactive sulfur precursor, Bis(trimethylsilyl)sulphide (TMSS), which was used in conjunction with more easily removable ligands, oleylamine (OLA) and oleic acid (OA), to control the synthesis and stabilise the product. Based on donor-acceptor-pair (DAP) recombination theory [58], creating an off-stoichiometry between Cu and In has shown to influence PLQY. Therefore,

by controlling the injection temperature and precursor ratio, the ideal Cu: In ratio of the nanocrystals can be established, and, finally, the changes in PLQY can be assessed. Furthermore, differences in halide precursor reactivity were used to predict and control the Cu: In ratio and observe additional enhancements of PLQY through halide passivation effects.

4.2 Synthesis Methodology

As introduced in Chapter 3.2, in a typical hot-injection synthesis, sulfur precursor is injected at a high temperature (~250 °C) to quickly nucleate and grow the nanocrystals. The injection temperature is known to be one of the main factors affecting the final nanocrystal size [108]. For a narrow size distribution of nanocrystals, as described by La Mer [82], rapid nucleation, but slow growth is preferable. Therefore, high injection temperature may generate fast nucleation, but to achieve a monodispersed nanocrystals, slow growth is preferable [114]. In this work, the injection temperature was lowered to less than 130 °C to control the dispersity of nanocrystal size; the synthesis will be defined as low-injection method. In order to achieve a lower injection temperature the highly reactive TMSS precursor was used to create favourable reaction kinetics. TMSS has been widely used in binary chalcogenide nanocrystal synthesis (e.g., PbS [164] [165], CdS, and SnS) as it produces more homogeneous, small diameter nanocrystals at reaction temperature lower than 100 °C [166].

After core synthesis and cleaning steps, an epitaxial shell of ZnS was grown using a zinc stearate and additional injection of TMSS. Details of the apparatus used, synthesis procedure, and characterisation techniques are given in Chapter 3.2.

4.2.1 Summary and rationale for reagents used

The precursors, ligand, and solvent quantities are summarised in Table 6. Initially, acetate precursors were used for both Cu and In. The synthesis method was refined by experimenting with various injection temperatures and precursor ratios. Based on the results, the best synthesis conditions were found. To further enhance the PLQY, 16 halide precursor combinations were used. This experiment studied the influence of precursor reactivity and counter-ion effects.

For ZnS shell, commonly used precursors include zinc chloride, zinc acetate, and zinc stearate. Park *et al*. demonstrated zinc stearate to be the most effective precursor to form a ZnS shell, based on the largest blue shift compared to the other precursors with the same experimental conditions [108]. Therefore, in this chapter zinc stearate was used throughout the experiments for ZnS shell.

The two ligands used were Oleylamine (OLA) and Oleic acid (OA). OLA is a long-chain primary alkylamine commonly used as a surfactant due to its high boiling point (~350°C). It also acts as an electron donor, therefore is a reducing agent [167]. Similarly OA is a long chain fatty acid, that controls the reactivity of indium [91] but also, regulates the crystal shape and structure, and help form a round CP CIS nanocrystals [45]. Lastly, 1-octadecene (ODE) a non-coordinating solvent with a high boiling point of 315°C was used as an additional solvent.

Table 6- List of all the reagents used in this chapter

Reagents	**Linear Formula**	**Quantity (mmol)**	**Quantity (g)**
Copper	$CuCO_2CH_3$	Varies throughout experiment	
	Cu(1)F, Cu(1)Cl, Cu(1)Br, Cu(1)I	0.25	0.03
Indium	$In(C_2H_3O_2)_3$	Varies throughout experiment	
	In(3)F, In(3)Cl, In(3)Br, In(3)I	1.00	0.29
Zinc stearate	$Z_n(C_{18}H_{35}O_2)_2$	2.00	1.27
Oleylamine	$C_{18}H_{35}NH_2$	10.00	5.35
Oleic acid	$C_{18}H_{34}O_2$	5.00	1.41
1-Octadecene	$C_{18}H_{36}$	30.00	7.54
Hexamethyldisilathiane (TMSS)	$((CH_3)_3Si)_2S$	1.50	0.29

4.3 $CuInS_2$ (core) and $CuInS_2$-ZnS (core-shell)

For the first set of CIS synthesis experiments, acetate precursors for Cu and In were employed. Both the acetate precursors were added to the three-neck flask with ODE, OLA, and OA as solvents. The three-neck flask was heated using an oil bath to keep the temperature rising relatively constantly. First, reagents were degassed at 100 °C by cycling three times between a vacuum and argon atmosphere, and on average, this step took 30 mins. Next, the temperature was increased to 180°C to decompose and reduce the precursors, and this process took an average of 10 mins. As the temperature increased, the solution colour changed initially from clear to blue, green, and lastly to light yellow as portrayed in Figure 25. This colour change corresponded to OLA reducing Cu^{+1} to Cu^{0}. After the reaction reached 180 °C, the solution was cooled to the injection temperature required. 30 mins of cooling time were necessary. In this preliminary study, TMSS was injected at 30°C, and upon injection, the solution colour turned dark brown, and then the temperature was increased to 130°C for nanocrystal growth with a concomitant colour change to red-brown. The reaction was stopped 10 mins after reaching 130°C and cooled to room temperature. The time taken for each step and the changes observed were recorded each time. When repeated with the same recipe, each sample batch took an average of 2.5 hours to be synthesised.

Figure 25- Showing colour change in the solution with increasing reduction temperature. From 30°C to 130°C, colour changes from blue → green → yellow, indicating that Cu has been fully reduced.

After the $CuInS_2$ core was cleaned, the ZnS shell is synthesised. The details of this process are described in Chapter 3 in the Methodology Section 3.2.2. ZnS was used for three main reasons: 1) Zn^{2+} has a similar ionic radius as Cu^{+} and In^{3+} (0.74, 0.74, and 0.76Å, respectively); 2) $CuInS_2$ and ZnS have comparable lattice parameters of 5.52Å and 5.40Å, respectively, so lattice mismatch strain is small (between 2-3%); and 3) through cation diffusion, Zn^{2+} can easily replace Cu^{+} or In^{3+}. Son *et al*. recently showed that reaction kinetics are different at the nanoscale and activation energy for diffusion is lower, permitting cation exchange [168]. In addition, the Gibbs formation enthalpy of $CuInS_2$ and ZnS are close, being -221 [169] and -206kJ mol^{-1} [170], respectively, making the reaction thermodynamically favourable for Cu^{+} and In^{3+} cations to be exchanged with Zn^{2+}. Currently, the literature is divided with regards to whether ZnS forms a shell as such [108], or whether a ZCIS alloy is formed [110]. If an additional step was taken to clean the core ($CuInS_2$) and add sulfur precursor, then it is safe to assume a ZnS shell was formed.

Temperature and time are important for shell growth. For example, Park *et al*. demonstrated that increasing the reaction temperature from 150°C to 230°C resulted in a stronger blue-shift in emission and enhanced peak intensity [108], while Nam *et al*. studied PL emissions with growth time and noted a blue-shift in emission for shell-coating

reactions between 30 mins and two hours, after which no further blue-shift was observed [59]. On the basis of these two publications, the shell synthesis in this work was performed at 180 °C for two hours. Throughout the reaction period, the synthesis reaction solution changed colour from brown-red to red.

Analysis of the core-shell nanocrystal colloid with TEM indicated that monodispersed nanocrystals of a size of approximately 3.6nm (±0.5nm) (Figure 26a) are formed. Figure 26b features a high-resolution image of a typical nanocrystal with a lattice spacing of 0.32nm, which corresponds to the (112) plane. This demonstrates the formation of high-quality single crystal nanoparticles with minimal defects. A FFT of the HR-TEM image in Figure 26c confirmed the formation of a CP structure. Unfortunately, HR-TEM could not be employed any further to compare the core and core-shell structures because of the similarity of the crystal structures between CIS and ZnS and the minimal Z-contrast in HR-TEM.

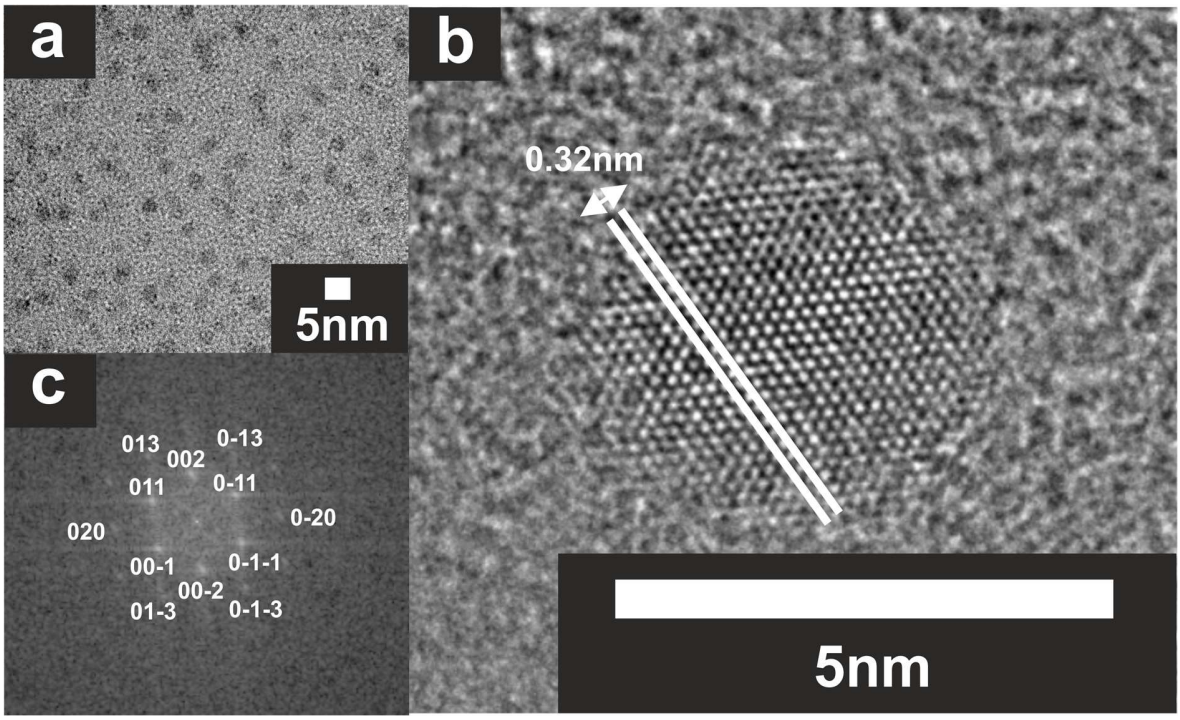

Figure 26- a) Low-resolution TEM depicting the overall size distribution of nanocrystals, b) showing HR-TEM of $CuInS_2$-ZnS at 1.5Mx, and c) FFT of the nanocrystals with size is ~3.2nm with lattice spacing of 0.32nm. The FFT diffraction pattern corresponds to a Chalcopyrite structure.

Subsequent to core synthesis, a shell layer was added. From TEM analysis, as per Figure 27, the nanocrystal size increased from 2.10nm for the core-only nanocrystals to 3.45nm for the core-shell samples. The size of the nanocrystal was measured by first enhancing the contrast and expanding the image using Image J software. Each nanocrystal diameter was measured in four directions and the average was taken. The increase in nanocrystal size indicated that a ZnS shell was formed rather than a ZCIS through cation exchange.

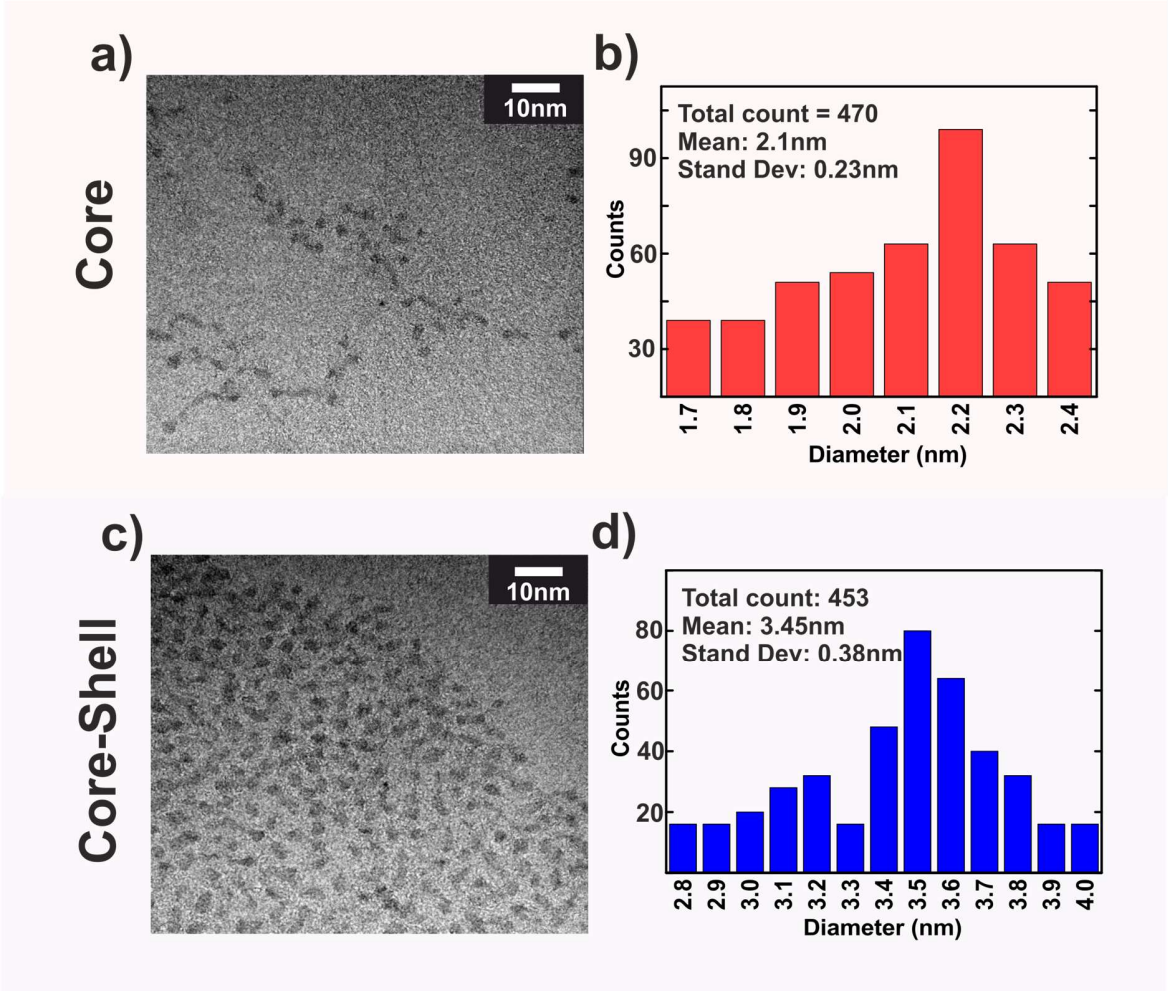

Figure 27- Size distribution of injection temperature at 30°C of both core and core-shell. Core has mean nanocrystal size of 2.10nm, whereas core-shell nanocrystals have a larger diameter of 3.45nm, indicating the growth of a shell layer. The TEM image only represents a small area of the sample. Various different areas were used to estimate the nanocrystal size.

During each instance of cleaning, the difference between CIS and CIS-ZnS was observed. For the CIS cleaning step, a number of nanocrystals were no longer dispersed in hexane as core-only nanocrystals became easily oxidised and unstable [90], while for CIS-ZnS, no product loss was observed, demonstrative of better stability than just the core CIS. A photograph of both core and core-shell products can be seen in Figure 28 with and without UV light illumination. Core-only luminescence is barely noticeable while that from the core-shell nanocrystals is strong. The PL confirmed that emission was enhanced

and blue-shifted in core-shell was seen (Figure 29). This improvement was because of the shell reducing the surface defects by passivating the core, thus, decreasing the non-radiative recombination pathways.

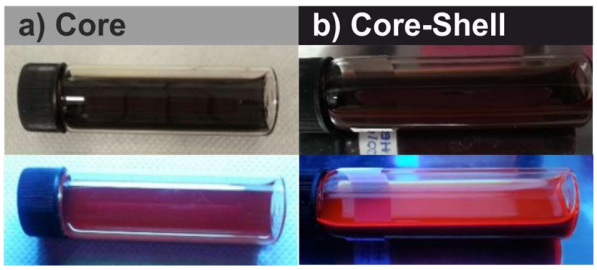

Figure 28- Picture of $CuInS_2$ solution and $CuInS_2$-ZnS at dark and UV illuminated

By adding a shell, the emission peak is shifted by approximately 90nm (Figure 29). There are two theories in the literature that describe the origin of this shift. The first is that cation exchange of Cu and In with Zn occurs, decreasing the size of the core, thereby shifting the emission wavelength [135]. The second theory suggests that there is a reconstruction on the surface that affects the overall band gap [129]. Changes in emission wavelength owing to core-shell structure is further investigated in the next section.

Additionally, according to Figure 29, the core-shell PL peak is slightly asymmetric as the ZnS shell itself must go through recombination. ZnS has a larger band gap than CIS, therefore contributes to photoluminescence within the blue wavelength region.

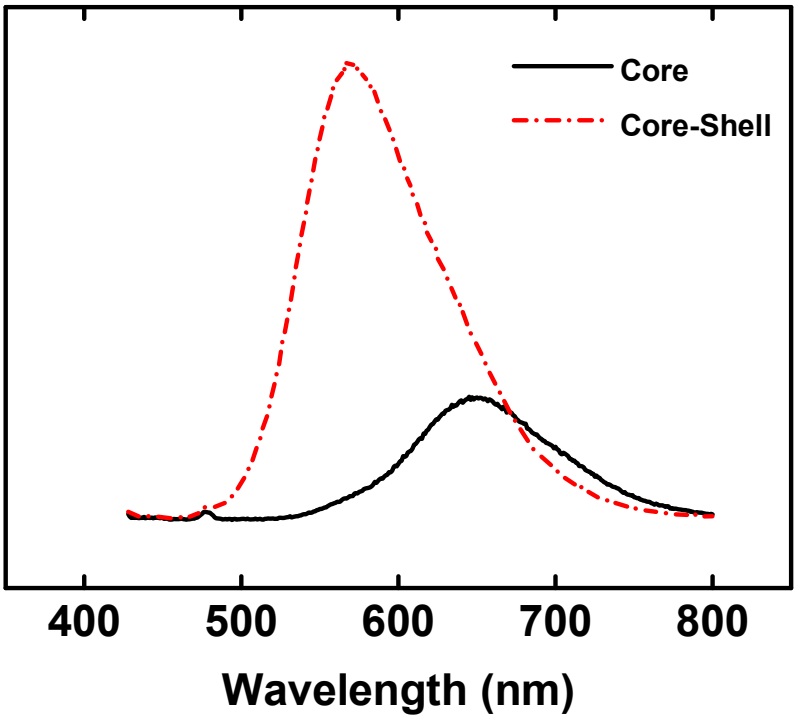

Figure 29- Comparing PL emission of core and core-shell. A blue shift of 90nm is observed between core and core-shell. Enhancement of PL emission is observed with addition of the shell.

4.4 Enhancement of PL through stoichiometry control and core-shell formation

Two strategies for improving the PLQY of ternary nanocrystals have been reported. The first, as mentioned with respect to the preliminary experiments in the previous Section 4.3, PL enhancement can be achieved by forming a core-shell structure. The second strategy is to regulate internal defects. DAP theory suggests the deficiency of Cu creates defects that produce intra-gap states along with donor and acceptor states, which are new radiative recombination pathways, hence increasing PLQY [171]. Defects, in the case of CIS, would be In_{Cu} (In substituted at a Cu site), V_S (S vacancies) being donor states and V_{Cu} (Cu vacancies) being acceptor states. This theory was validated by Castro *et al.* [58] and others [171] where there was an achievement of similarly consistent results which linked internal defects to major radiative recombination sites for ternary nanocrystals [59, 60, 172]. However, there are conflicting hypotheses as to whether the CB or VB plays a role in the recombination of charge with the localised state, or whether the effect simply involves localised states [15]. At this point, a full understanding is not available, meriting further investigation to establish the nature of the recombination. In this sub-chapter, based on DAP theory for increasing PL, the injection temperature and the precursor ratio are changed to see how In content influences PLQY.

4.4.1 The effect of injection temperature on the Cu/In ratio and PL QY

To understand how TMSS injection temperature affects nanocrystal synthesis, four different TMSS injection temperatures, 30, 50, 70, and 90°C, were studied. Each sample was cleaned and a shell layer was added as per Section 4.2, with just a change of the injection temperature.

For each injection temperature, UV-Vis and PL were measured. Figure 30a and Figure 30b show that as the injection temperature was raised, the absorption and emission are shifted to lower wavelengths. This is governed by the increase in In content, which widens the band gap. It is safe to assume that the shift is mainly because of compositional changes, since if it was due to size dependence, an increase in injection temperature would grow larger nanocrystals. Therefore, a red-shift would be observed instead. An in-depth description of theory is found in the following section.

Additionally, in Figure 30b, the FWHM of the PL is demonstrated to decrease as injection temperature is reduced. This is because of the difference in reaction time. Regardless of the injection temperature, the final reaction temperature was increased to 130°C, thus, a sample injected at 30°C has more time to grow than a sample injected at 90°C. The main growth mechanism here is by diffusion-controlled growth, where nanocrystals grow by addition of unreacted precursors. Under these diffusion-controlled conditions, the growth rate is inversely proportional to the radius of the nanocrystals, therefore, overall size variations become narrower with the rise in growth time [85].

In Figure 30d, after shell addition, the shift to the lower wavelength with decreasing injection temperature trend remains. While the FWHM is similar for all injection temperatures as during the two-hour shell growth period, there is also diffusion-controlled growth, the size variations for each batch become homogeneous. Interestingly, an overall blue-shift compared to Figure 30b was also observed. This is a typical observation for CIS-ZnS synthesis, where the band gap widens [171, 173]. When the ZnS shell overcoats the core, partial cation exchange takes place in the outer layer, decreasing the

overall size of the core [129]. Additionally from lattice mismatch (~3.1%) between ZnS and CIS, which induces a compressive stress on the core [78], resulting in an overall blue-shift in terms of emission wavelength.

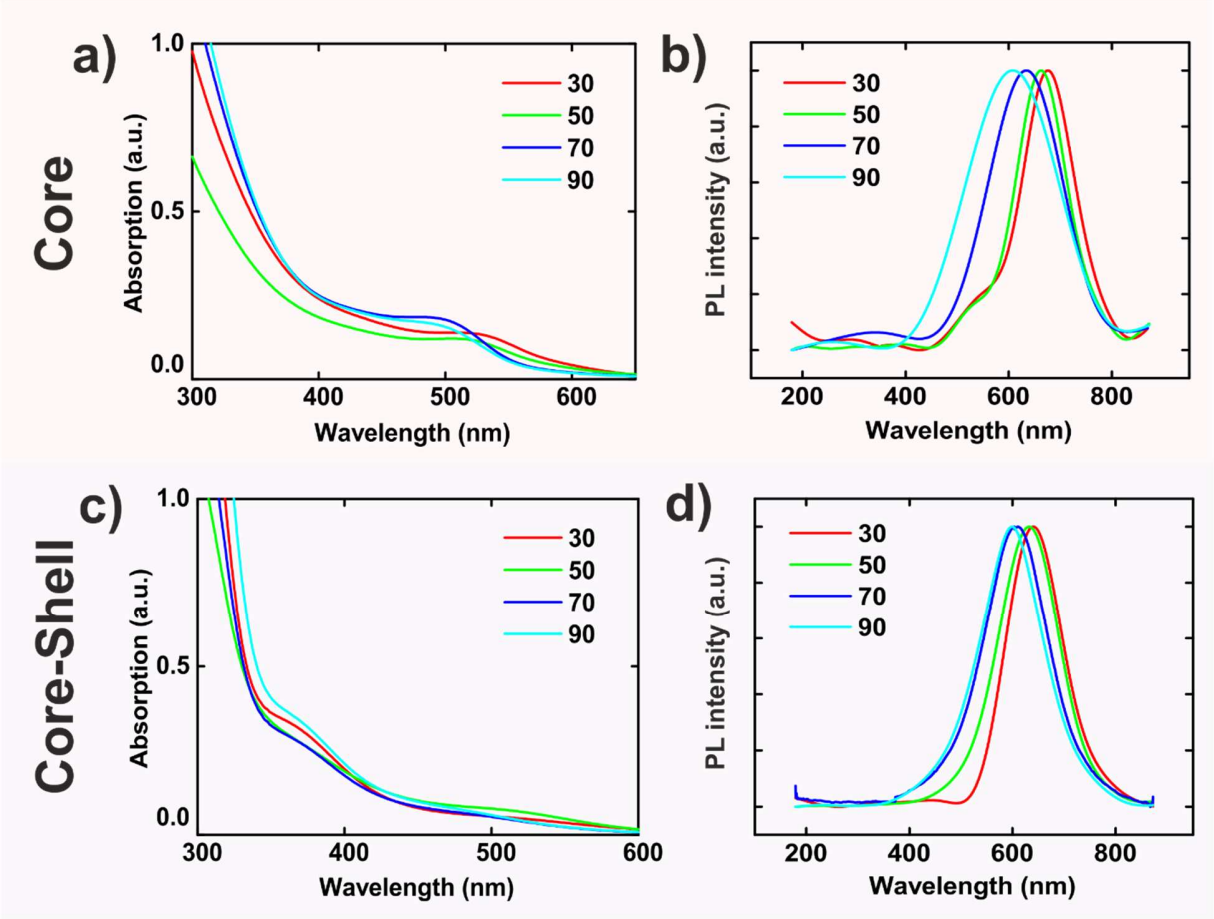

Figure 30- Four graphs showing the results from different TMSS injection temperatures. 21a and 21b show absorption and PL emission from core-only nanocrystals. 21c and 21d show core-shell absorption and PL emission. A shift to lower wavelengths and an increase in FWHM is observed with increasing injection temperature, suggesting that more In is incorporated and an increase in polydispersity with increase injection temperature. Comparing b) and d) PL emission wavelength has blue shifted, with the influence of ZnS formation.

The PL peak values in Figure 30b and Figure 30d are plotted in Figure 31a. The trend determined is that there is a larger blue-shift observed for lower injection temperatures. STEM-EDX was utilised to measure the changes in nanocrystal composition. Figure 31b depicts that higher Zn: Cu+In content is observed for nanocrystals in which the core was

formed with a lower TMSS injection temperature. The amount of Zn incorporated into the nanocrystal sample decreased with rising injection temperature. One hypothesis may be that it is related to the overall Cu content for each CIS synthesis [104,110]. Zn preferentially exchanges with Cu compared to In; this is because the Cu-S bond is weaker than the In-S bond and Zn substitution of Cu is energetically more favourable [174].

Figure 32 shows that as the injection temperature increases, the nanocrystals become more In-rich. Therefore, there is more Cu available at low injection temperatures to exchange with Zn, which enhances the incorporation and growth of the ZnS shell and generates a greater blue-shift.

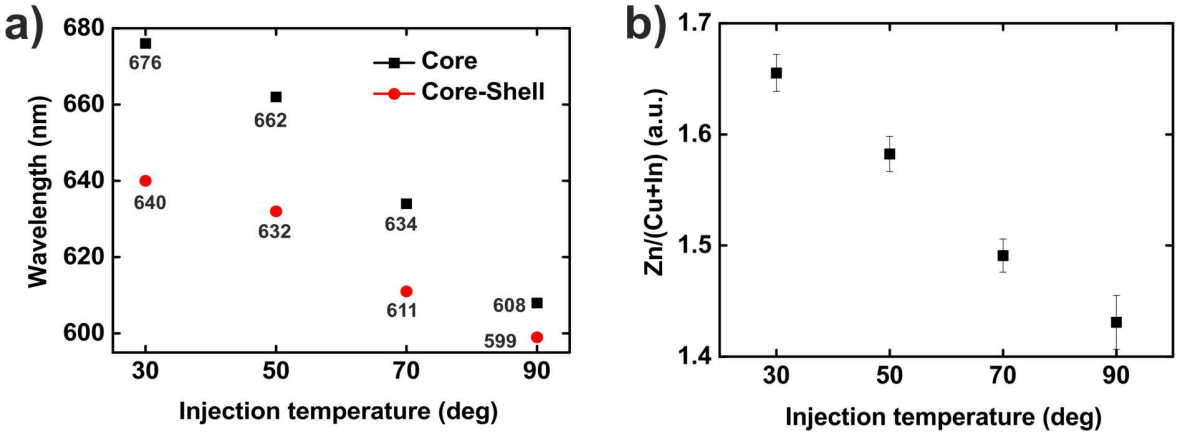

Figure 31- a) showing the difference in peak emission wavelength of core and core-shell at different injection temperature. b) showing Zn ratio of Cu+In changes with injection temperature in core-shell nanocrystals. All experiments were repeated to verify its reproducibility.

From Figure 32a and Figure 32b, it can be seen that the overall PLQY increases 10-fold from the core to the core-shell. Shell formation reduces surface defects, decreasing the non-radiative recombination pathways.

Normally, based on the literatures [108, 103], an increase in In content raises PLQY. However, Figure 32a shows a different trend, where for the core, PLQY and In content are inversely

related. As mentioned earlier, increasing injection temperature means less growth time, which raises the overall polydispersity and this lowers PLQY. Polydispersity of broad size variation also takes place, but this would create nanocrystals with less defined crystal structure, which may be more subject to non-radiative recombination pathways (further details on this are found in Section 5.5). For the core-shell (Figure 32b), during the cleaning procedure, small nanoparticles were partially removed and the two-hour shell growth time allowed nanocrystals to homogenise, and, therefore, polydispersity was reduced. As such, the core-shell linear trend of higher In content results higher PLQY, just as mentioned in the literatures [108, 103].

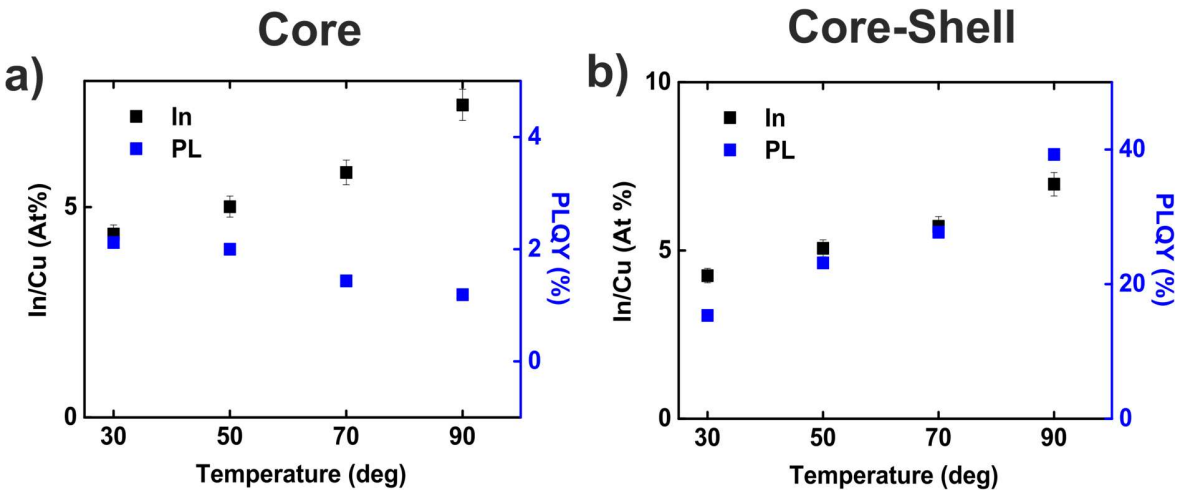

Figure 32- Showing the relationship between In/Cu ratio to PLQY of each injection temperature (a core and b core-shell).

In this section, TMSS injection temperatures were shown to affect both the polydispersity and the Cu:In content of the nanocrystal. At lower injection temperatures, more growth time was available for the nanocrystals, where there was reduced polydispersity. Meanwhile, higher injection temperatures were shown to have overall more In content. After reducing polydispersity, it was shown that there was higher In, an enhancement of

PLQY and blue-shift emission wavelengths because of the resulting increase in the band gap. With a core-shell structure, the highest PLQY achieved was ~40% at 90°C injection temperature.

4.4.2 Investigating the effect of the stoichiometry of the Cu/In ratio on PL QY

From the previous sub-chapter, changing the injection temperature led to differences in Cu:In stoichiometry that influenced the enhancement and changes in the PL emission wavelength. According to the literature, the precursor ratio is modified by adding different amounts of reagents, termed an off-stoichiometry study [42, 175]. Here, using low-injection temperature synthesis, the feasibility of an off-stoichiometry study was assessed and the effects on PL were observed.

Four different Cu:In precursor ratios have been examined in this work - 1:2, 1:3, 1:4, and 1:5. For CIS synthesis, to avoid nanocrystal polydispersity effects, the injection temperature was set to 30°C. All synthesis were followed by a shell addition. Other conditions remain as described in Section 3.2.

Figure 33a shows the STEM-EDX analysis of CIS with different precursor ratios. From the TEM-EDX, it can be seen that In increases proportionally to the amount of precursor added, therefore, the final cation precursor content can be successfully controlled using the low-injection temperature method. Similar to the core-only nanocrystals, core-shell nanocrystals still clearly show, as in Figure 33b, a relative rise in In content with the added precursor.

From the PL emission peaks in Figure 33c, it can be established that as the ratio of the In content increases relative to Cu, the peak shifts to the blue wavelength while PLQY increases (Figure 33d), just as was observed in Section 4.4.1. For Cu-deficient nanocrystals, the Cu d-orbital character decreases and weakens the Cu d-/S p-interband repulsion, which lowers the VB and therefore widens the overall band gap [15,129,176].

Chen *et al.* also observed [42] that greater In content results in enhanced PLQY, with the higher defect density elevating the probability of carrier recombination. Additionally, in Figure 33d, it shows that core-shell, compared to core-only PLQY, increases 10-fold, suggestive of an effective passivation.

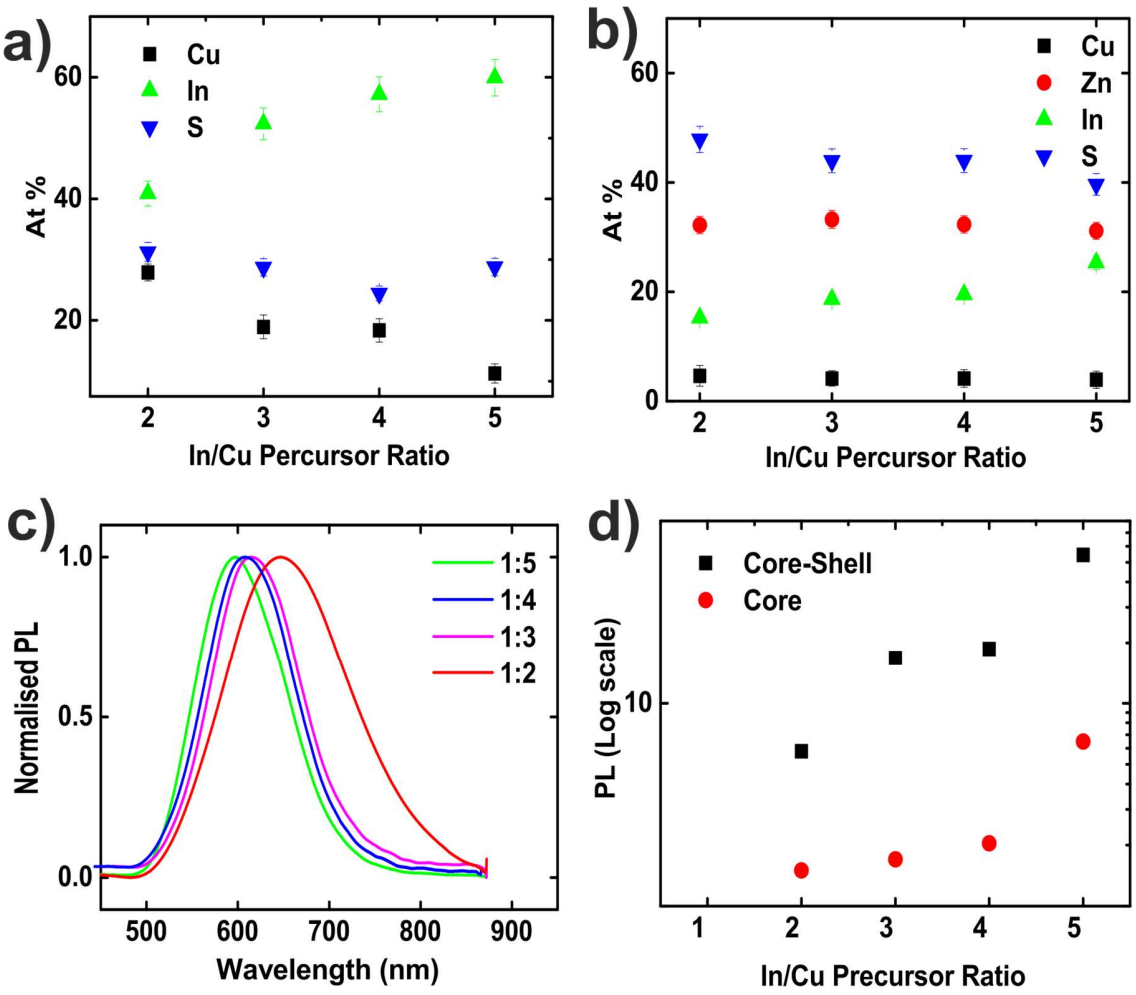

Figure 33- a- EDX data of CIS(core) b- EDX data of CIS-ZnS(core-shell) c- Core-shell PL emission of nanocrystals with 4 different precursor contents d- core & core-shell PLQY in relation to precursor content

To directly compare the Cu:In ratio of the precursors and that of the final composition of the nanocrystals (Figure 33a and Figure 33b), the ratios were plotted (see Figure 34). From Figure 34a, the precursor ratio of both the initial and final compositions are similar to each other. Meanwhile, for the core-shell, as in Figure 34b, the overall In content detected rose. This was expected as discussed in Section 4.2.1 - Zn tends to exchange more readily with Cu, increasing the relative In.

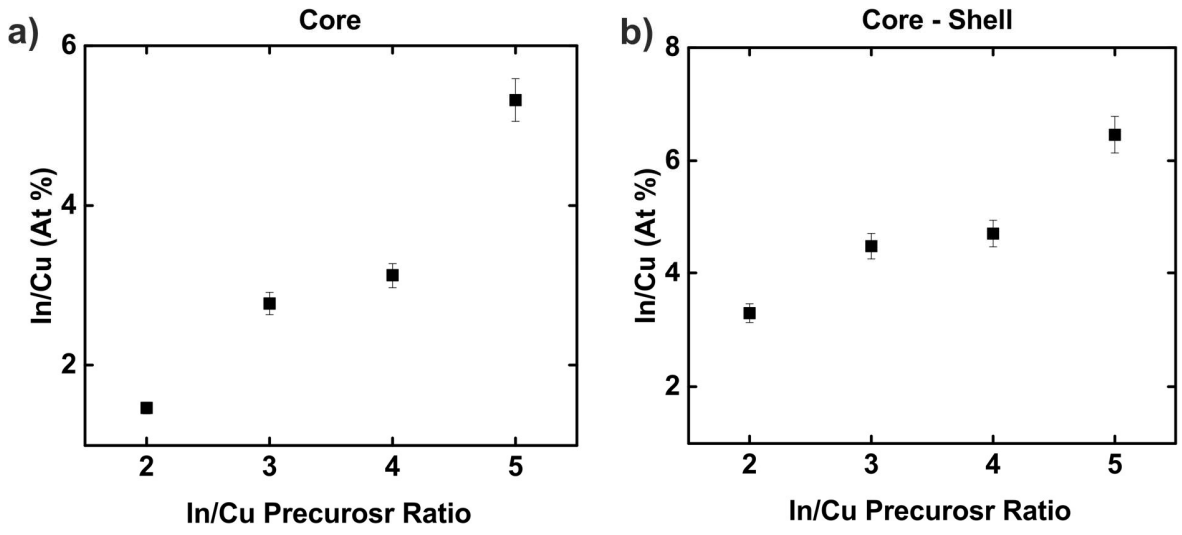

Figure 34- Core (a) and core-shell (b) precursor content detected by EDX (FINAL) vs. actual precursor ratio used (INITIAL). Both core and core-shell show a linear relationship between final and initial precursor ratio, therefore, the low-injection temperature synthesis is effective in capturing the added precursor ratio.

4.5 Effect of halide precursor combinations

The greatest difficulty with ternary nanocrystal synthesis is controlling Cu and In cation precursor reactivity. Cu is a soft Lewis acid and In is a hard Lewis acid. As S is a soft Lewis base, the reactivity of each of the cation precursors with S is different [6]. To regulate the reactivity, OA and OLA ligands were used. OLA is a strong Lewis base that bonds readily with In and controls its reactivity [177] while OA bonds more strongly to the nanocrystal surface than OLA [94], influencing overall growth. However, the ligands cannot fully stabilise the differences in cation precursor reactivity. To control reaction reactivity, one solution is to use different precursors. A study by Ford *et al*. examined iodide, acetate, nitrate, acetylacetonate, and chloride precursors for CIS synthesis and showed that certain shape variations were observed [178].

In this section, a further investigation of precursors was performed to predict the relative reactivity of Cu and In and to control the composition in order to achieve a high PLQY. Fluoride, chloride, bromide, and iodide salts of both Cu and In were used and all 16 permutations investigated. The reaction was carried out as before with an injection temperature of 30°C and reaction heated to 130°C.

Halide precursors were chosen for two reasons. The first was because of HSAB theory, whereby hard acids tend to attach better to hard bases than soft bases, and the same logic applies to soft acids. In particular, 'hard' refers to a small and highly charged state that is weakly polarisable, whereas soft refers to a large and low charged state that is strongly polarisable. Based on the HSAB theory, the order of F→ Cl→ Br → I corresponds to moving from hard to soft bases and as Cu is soft acid and In is a hard acid, the interaction of each halide and cation will be different. Zhong *et al.* examined the HSAB effect on

reactivity by through acetate and iodide Cu precursors. In particular, they observed iodide, being a softer base, strongly attached to Cu (soft acid) compared to acetate. Therefore, the reaction was slower for CuI relative to Cu acetate [179].

The second reason to explore halide precursors is that halide passivation has been shown to enhance PL and device performance with regards to photovoltaics [112]. Halide post-treatment has been used on colloidal quantum dots (CQD) for photovoltaic applications to passivate surface defects [112, 116]. For instance, Sargent's group demonstrated that halide passivation decreases trap sites that large organic ligands cannot bind to. Further, by replacing a long organic ligands with short halide ligands, the distance between CQDs decreased. Therefore, using halide passivation enhanced the overall efficiency of the photovoltaic device with better film density [180].

Different halide precursors will have varying effects on nanocrystals as the halides and counter ions have unique atomic numbers. Tessier *et al.* tested In-Cl, In-Br, and In-I halide precursors for InP nanoparticle synthesis. They observed the nanocrystal size decreasing from Cl → Br → I. They believed that as the atomic number increased down the periodic table, the ion volume rose, providing better blocking of the adsorption sites, which reduced the surface reaction rate, therefore, producing smaller nanocrystals [181].

The reactivity of Cu is known to be higher than In [90]. This is described by Pearson's hard-soft acid and base theory. Cu is a soft acid with a large radius and low positive charge, while, on the contrary, In is a hard acid, has a small ionic radius, and high positive charge. Therefore, Cu is more polarizable than In, hence more reactive. Based on the DAP theory, an increase in In content increases the overall PLQY. The best combination is a In

precursor with the highest reactivity and a Cu precursor with the lowest reactivity. As such the best combinations would be In-I (hard acid-soft base) and Cu-I (soft acid-soft base).

To predict the best combination, an expression for a figure of merit was devised which calculates combinations with the highest In content. This expression is based on solubility and bond dissociation energies of the precursors. For a precursor to decompose and be reduced, it first needs to be solubilised, then its bonds broken for reduction to occur. The solubility and bond dissociation energy values of Cu and In precursors are summarised in Table 7.

Table 7- Solubility (in water [182]) and bond dissociation energy of each Cu and In halide precursor

	Solubility, S		**Bond dissociation energy, Eb (kJ/mol)**	
	Cu	In	Cu	In
F	0.1	11.2	506.15	431.13
Cl	0.0099	212	439.8	383.21
Br	0.0009	571	418.21	331.25
I	2E-05	600	197.21	197.21

The figure of merit is given by:

$$\frac{\frac{S(\mathrm{InX})}{\sum_{i=1}^{4} S(i\text{th In precursor})}}{\frac{E_b(\mathrm{InX})}{\sum_{i=1}^{4} E_b(i\text{th In precursor})}} + \frac{\frac{S(\mathrm{CuX})}{\sum_{i=1}^{4} S(i\text{th Cu precursor})}}{\frac{E_b(\mathrm{CuX})}{\sum_{i=1}^{4} E_b(i\text{th Cu precursor})}}$$

The figure of merit is used to determine which combination will have the highest In content. As solubility (S) becomes higher, it is easier for the solvent to dissolve the solute, therefore, having a positive effect on the figure of merit, whereas bond dissociation

energy (E_b) possesses an inverse relationship because for decomposition to take place, the bond needs to be broken. As bond breaking is an endothermic reaction, energy needs to be absorbed for a reaction to be carried out. The higher the bond energy, the greater the barrier for the reaction. Therefore, the equation is S divided by E_b.

The figure of merit was calculated for all 16 precursor combinations. PLQY against the figure of merit is plotted in Figure 35a. The actual In content was measured by STEM-EDX as seen in Figure 35b. Comparing the two graphs (Figure 35a and Figure 35b), the trends nearly match, suggesting that this figure of merit can be used to predict In content. Figure 36 features a bar chart compiling the data from Figure 35a and Figure 35b. The data are grouped by Cu-halide precursor, and each bar label is the In-halide precursor. As expected, InI_3 (hard acid-soft base) of each group had the highest final In content and figure of merit value.

It is known that PLQY is related to In content, as more In content raises the probability of DAP recombination. From Figure 35b, it can be seen that, for example, the Br-I, I-Cl, and F-I combinations have similar In content but their PLQY varies. Also, I-I has higher In content than Cl-I but has lower PLQY. This can be explained by the counter ion effect of the remaining halide. Zhang *et al.* showed that for PbS synthesis, Pb-Cl had better device efficiency than Pb-Br or Pb-I. This was based on Cl being more passivating as its size was smaller, and Cl_2 prevents oxidation [114]. This halide study demonstrated how high In content increases internal defects for DAP recombination, and smaller-sized counter ions have better passivation because of stronger bonds and size.

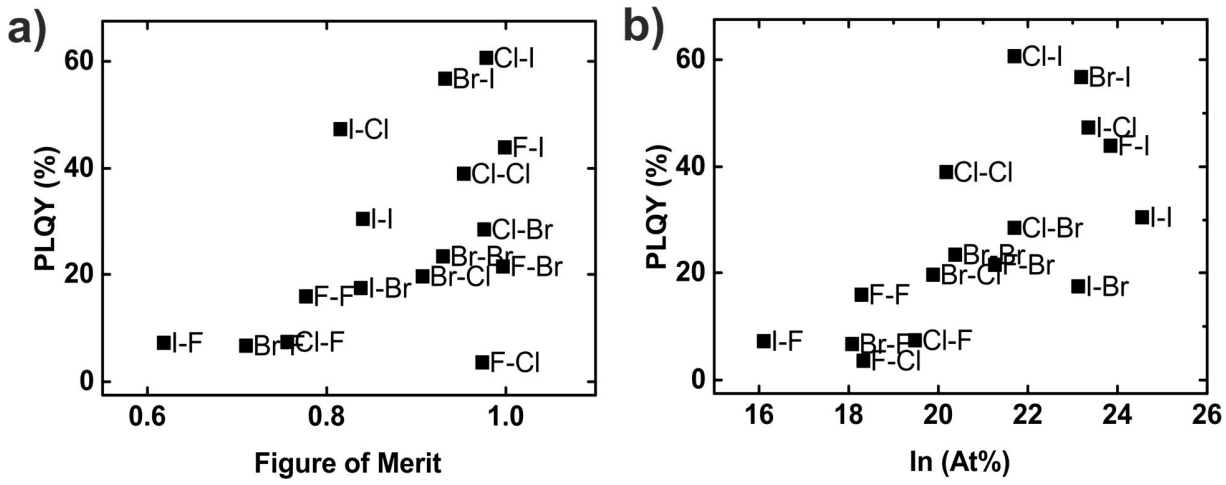

Figure 35- a) Figure of merit b) STEM- EDX measured In content. The two graphs show nearly identical trends.

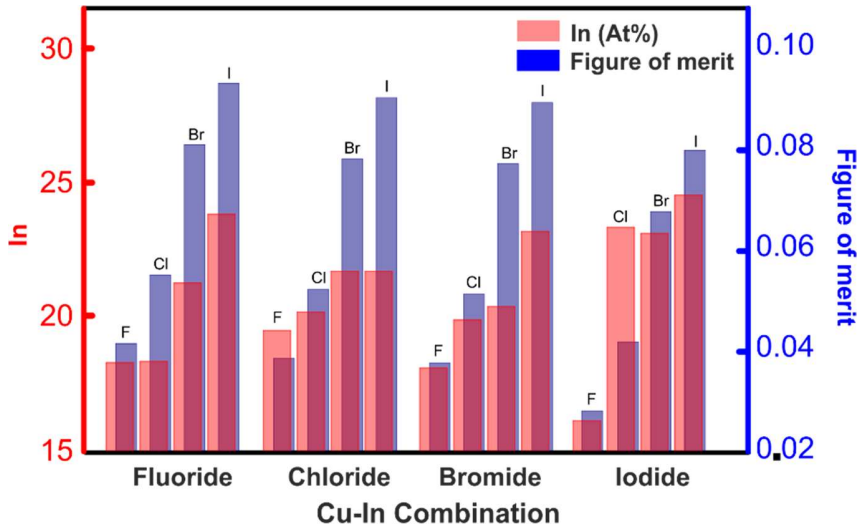

Figure 36- Bar chart reconstructed from Figure 26. Bars are grouped by copper halide precursor. As predicted, combinations involving the InI_3 precursor have both the highest figure of merit and In content.

Compared to acetate precursors, where using the same experimental conditions, the highest PLQY achieved was 50% (Figure 33d), for halide precursors, the highest PLQY achieved was 60%. Therefore, not only can halide precursors be used to control the reactivity of the precursor, but they can also enhance overall PLQY.

4.6 Conclusion

To summarise, this chapter introduced a new synthesis method for $CuInS_2$-ZnS, a low-injection temperature method utilising highly reactive TMSS. For ternary nanocrystals to achieve a high PLQY, DAP recombination pathway should be increased, which is governed through off-stoichiometry with increasing the In content relative to Cu.

Synthesis conditions, injection temperatures, and precursor ratios were changed to test the relationship between PLQY and In content. The best conditions for monodispersed nanocrystals with high PLQY were an injection temperature of 30°C and a 1:4 Cu:In ratio.

In addition to these findings, further enhancement of synthesis was accomplished with different halide precursor combinations. Halide precursors were used to regulate the relative reactivity of Cu and In and for halide passivation. Overall, using the same experimental conditions, compared to acetate precursors, halide precursors achieved a PLQY 10% higher, reaching a PLQY of 60%.

Chapter 5 – In-depth study of $AgInS_2$ synthesis

5.1 Introduction

In the previous chapter, we achieved a high PLQY of 60% using CIS-ZnS nanocrystals. However, the limitation of CIS is that it easily oxidises based on the nature of Cu oxidation. This chapter examines replacing Cu with Ag as the +1 state of Ag is more stable, whereas Cu^{+1} is unstable and could decompose to either Cu^{2+} or Cu^{0+}, leading to formation of various crystal structures per synthesis [183].

The main limitation when using Ag is finding suitable precursors. Seeing that $Ag^{(+1)}$ is easily reduced to $Ag^{(0)}$ metallic compounds as well as unwanted by-products, such as Ag particles, may form [184]. Herein, by employing different halide precursor combinations and modifying the synthesis conditions, precursor reactivity is balanced to produce high PLQY AIS.

The properties of Ag and Cu are similar as they are both in the same group of the periodic table (group 11) and are soft Lewis acids. Therefore, Cu synthesis recipes can easily substitute Cu with Ag [90, 185]. Similarly, as seen in the previous chapter, AIS PLQY is also affected by off-stoichiometry through changes from DAP recombination.

Hence, using the study and synthesis developed from Chapter 4 for CIS-ZnS nanocrystals, a novel synthesis method for AIS was developed. The dynamics of nanocrystal growth were further investigated using *in-situ* PL and an aliquot study of samples taken at different temperatures. The samples were characterized using HR-TEM (EDX), XRD, PL, *in-situ* PL, and UV-VIS.

5.2 $AgInS_2$ Synthesis method

5.2.1 Synthesis procedure

Initially, the low temperature injection method introduced in Section 3.2 was carried out. Thereupon, the synthesis was modified throughout the experiments as new findings were uncovered. Other commonly used synthesis methods for AIS were reviewed in Section 2.3. Based on the literature studies, at least to our knowledge, the low-injection temperature synthesis used here was a novel synthesis method for AIS nanocrystals.

Ag and In precursors (In/Ag = ¼ ratio) were placed in a three-neck flask along with the ligands oleic acid (OA) and oleylamine (OLA), and an additional non-coordinating solvent 1-octadecne (ODE). The solution was heated to 130 °C while degassing for one hour in an argon atmosphere, the temperature was increased to 180 °C and held for five mins, then cooled down to room temperature (~30°C). TMSS was then injected and the temperature was raised back to 130°C for 10 mins in order to grow the nanocrystals. Subsequently, the same cleaning processes were carried out as described in Chapter 3.

5.2.2 Precursor selection

The precursors used for AIS synthesis are summarised in Table 8. If not otherwise specified, the halide precursors AgCl and InBr were used. In the last section of this chapter, Section 5.6, four halide precursor combinations using Cl and Br were tested. Unlike the CIS halide study, in the case of AIS, all four halides (F,Cl, Br and I) could not be used. When F or I were used, in the first cleaning step all the nanocrystals aggregated and could not be re-dispersed in hexane.

Table 8- Summary of the reagents used for AIS synthesis. Two different halide precursors of silver and indium, Cl and Br, are used. The quantities are measured in moles and remain constant throughout the experiments.

Reagents	**Linear Formula**	**Quantity (mmol)**	**Quantity (g)**
Silver	Ag(1)Cl, Ag(1)Br	0.25	0.036, 0.047
Indium	In(3)Cl, In(3)Br	1.00	0.221, 0.355
Oleylamine	$C_{18}H_{35}NH_2$	10.00	2.675
Oleic acid	$C_{18}H_{34}O_2$	5.00	1.412
1-Octadecene	$C_{18}H_{36}$	30.00	7.574
Hexamethyldisilathiane (TMSS)	$((CH_3)_3Si)_2S$	1.50	0.268

5.3 $AgInS_2$ PL stability compared to $CuInS_2$

Like CIS, AIS is a direct band-gap semiconductor. AIS has a band gap that can be tuned between 1.87 and 2.03eV, depending on its crystal structure, namely CP or WZ [186,118], while CIS has a band gap of 1.5eV [187]. Both also have a high excitation coefficient in the visible to near-infrared region [69]. The advantage of AIS nanocrystals over CIS nanocrystals is their stability after the cleaning process. In the case of Cu, the non-passivated Cu sites, when exposed to O_2, are easily oxidised and degrade over time. Riha *et al.* observed that when Cu_2Se was exposed to air at room temperature conditions, Cu^+ oxidised to Cu^{2+} to form an oxide layer on the surface [188]. In agreement with this, Table 9 describes that over a period of 11 days, PLQY has decreased by 50% for CIS, whereas for AIS, it remained constant.

Table 9- Comparing the degradation in PL of AIS and CIS nanocrystals (made by Br-Cl halide precursor combination) over 11 days. AIS nanocrystals are stable throughout the experimental period, whereas, CIS nanocrystals PL degrades quickly over time.

	PLQY (%)	
Number of days	**$AgInS_2$ (AIS)** Error ±0.5%	**$CuInS_2$ (CIS)** Error ±0.5%
1	66	6
3	66	5
5	66	5
7	66	4
9	66	3
11	66	3

Moreover, comparing the overall PLQY of AIS and CIS, AIS had values nearly 10-fold higher than that of CIS. This showed that the synthesis method employed here was able

to form AIS nanocrystals with better crystal structure and fewer surface defects that would cause non-radiative recombination [61]. Figure 37 is a photograph of CIS and AIS nanocrystals under normal room light and UV light. It can be seen that even before the UV light exposure, the Ag solution exhibited greater clarity and a brighter clear orange colour. Further, as expected from the PLQY values, AIS was much brighter than CIS under UV light. Thus, AIS has potential as stable highly luminescing nanocrystals.

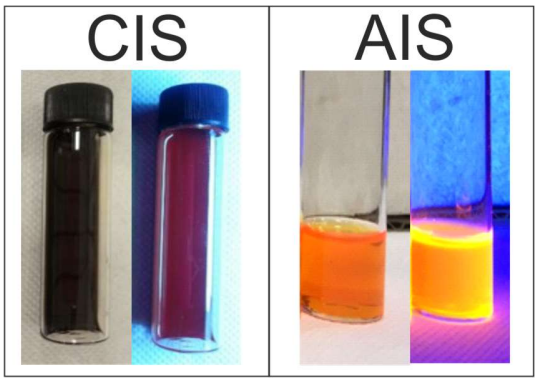

Figure 37-Picture comparing the clarity and the photoluminescence of CIS and AIS under on/off UV light (both images are reused from other figures within the thesis). AIS nanocrystals under room light show better clarity and brighter colour than CIS. Under UV light AIS shows higher PL emission than CIS.

5.4 Preliminary synthesis, characterisation, and results

The first main difference with AIS synthesis, unlike CIS, is that there was no colour changes observed during the reduction stage. In the case of CIS, the colour changed from blue → green → yellow. For AIS, this was not observed (solution remained clear) as the colour change was a characteristic feature of Cu. Only a yellowing of the solution was observed at 180 °C because of the colour change of OLA at high temperatures. Therefore, in the case of AIS, a colour change could not be relied on as a tool to determine the reduction state of Ag.

After cooling to 30 °C for TMSS injection, a noticeable white precipitate was deposited in the three-neck flask. Upon the TMSS injection, the solution turned light brown. As the temperature was increased to 130 °C, the colour gradually changed from light brown-orange to clear dark orange. Further colour changes with temperature are described in the next Section 5.5.

Through the study of the UV-Vis and PL emission of AIS, an excitation peak at ~490nm was observed while the PL emission peaked at ~620nm (Figure 38). Normally, excitonic features are rarely observed in AIS nanocrystals because of an unestablished synthesis procedure, thereby producing a broad range of particle sizes and many surface and internal defects [189, 190]. A large Stokes shift of 130nm as well as a large FWHM was observed between absorption and emission, which is a characteristic of DAP recombination [191].

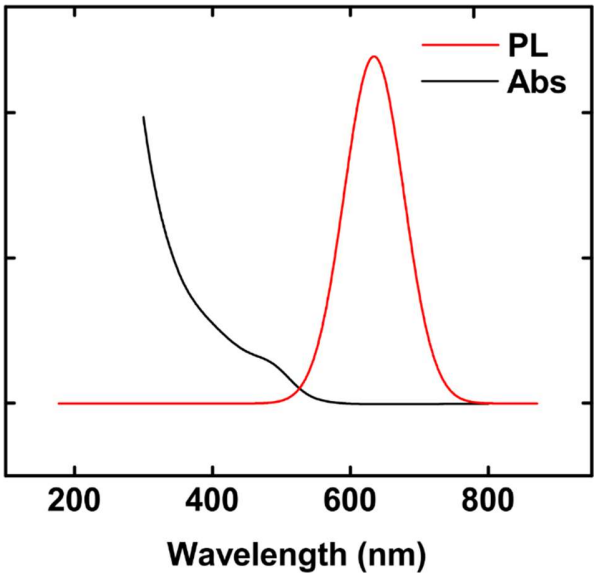

Figure 38- UV-VIS and PL emission of AIS illustrating a large Stokes shift of 130nm, with a clear excitonic peak in absorption at ~490nm and PL emission peak at ~620nm.

The nanocrystals were next cleaned and observed using TEM. Figure 39 features the TEM image of the nanocrystals, where high polydispersity of size and shape was notable. A variety of shapes, including spherical, square, and pyramidal, were observed. Nanocrystals were either large (>10nm) or small (<5nm) owing to bimodal variation, this will be explained in the following in accompaniment to the characterising of the by-products.

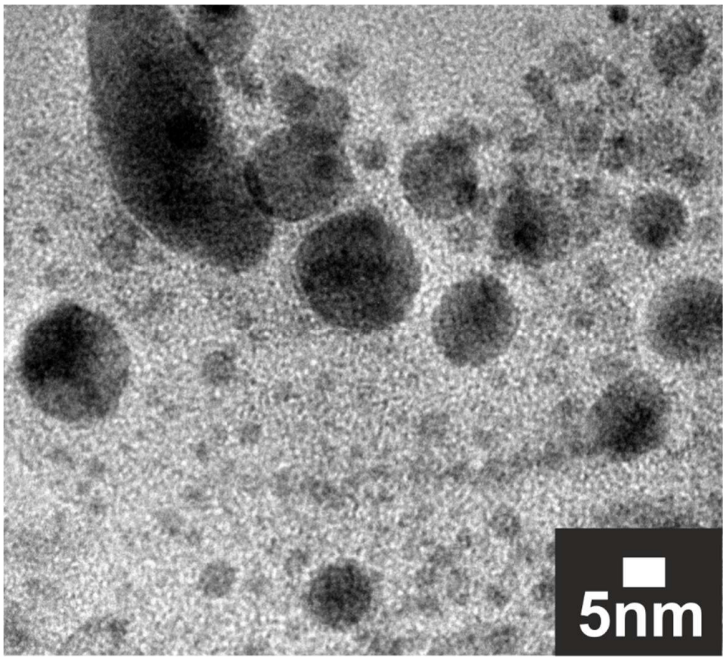

Figure 39-TEM image of AIS nanocrystals after cleaning step, showing the polydispersity of various shape and sizes.

To reduce the polydispersity seen through TEM in Figure 39, the nanocrystals were centrifuged at 2000rpm for 30 mins to assess whether the large nanocrystals could be separated. Surprisingly, the large nanocrystals were heavy enough to deposit as black precipitates at the bottom of the centrifuge. Additionally, CIS nanocrystal samples were centrifuged to verify if similar by-products could be observed, however no deposit was found.

Figure 40a shows the black precipitate collected from AIS and dispersed in hexane. From the UV-Vis (Figure 40b), it was seen there was an onset of absorption at 600nm (~2ev), which matches the band gap of Ag_2S that ranges between 600-1240nm (~1-2eV) [192]. Figure 40c depicts the TEM image of the nanocrystals with a size of approximately 8-10nm and a spherical shape. The large size indicated that the solution had already contained Ag nanocrystals before injection, and thiol, being a soft base, reacts quicker

with Ag, a soft acid [193]. As seen in Figure 41, STEM-EDX analysis confirmed the presence of Ag and S. Thus, through the combination of UV-Vis and TEM data, it was confirmed the black nanocrystals were Ag_2S.

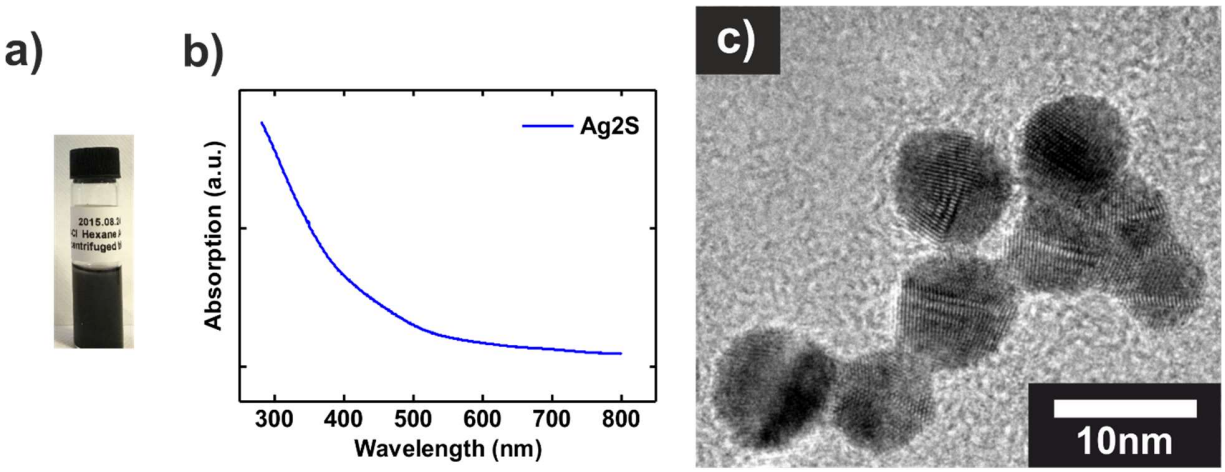

Figure 40-a) Picture of black precipitate found to be Ag_2S b) Corresponding UV-VIS c) TEM

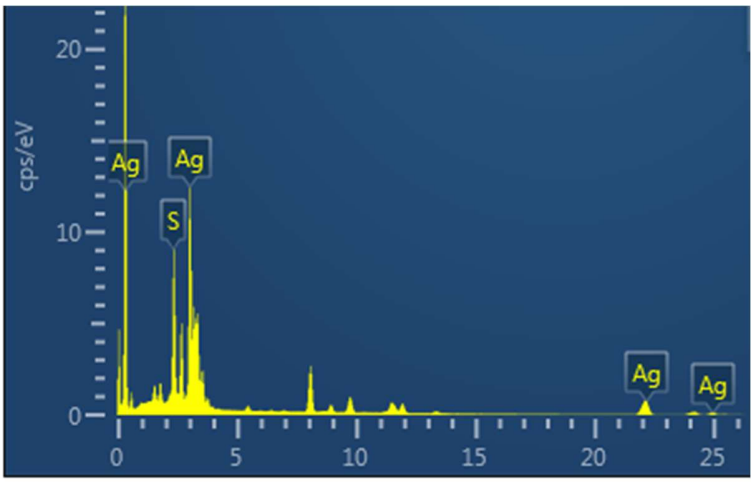

Figure 41- STEM-EDX elemental analysis graph taken from AZTEC software. Graph showing presence of Ag and S.

By removing the black precipitate through centrifugation, the PLQY increased from 43% to 66% (Table 10). Hence, reduction of the concentration of by-products is essential to achieve high PLQY AIS nanocrystals.

Table 10- Enhancement in PLQY of nearly 20 percentage points after removal of black precipitate Ag_2S.

	PL QY (%)
Before black precipitate removal	43
After removal	66

Before injection of TMSS, during the precursor decomposition stage, a small quantity of white precipitate was formed (Figure 42a). To further examine these white precipitates, at each AIS nanocrystal formation step, aliquots were taken for characterisation. Figure 42 (b-d) shows the characterisation results. As suspected, the white precipitate was made up of Ag nanocrystals. Figure 42b is the UV-Vis spectrum of the white nanocrystals, demonstrating a clear plasmonic resonance peak of the Ag nanocrystals around 450nm [194]. TEM analysis (Figure 42c and Figure 42d) indicate that the nanocrystal sizes varied from 10nm-20nm, and were slightly pyramidal and square shaped. Through STEM-EDX (Figure 43), the composition of the white precipitate was confirmed to be pure Ag nanocrystals. As covered before, Ag is known to reduce to $Ag^{(0)}$ easily, even at low temperatures [184,69]. Additionally, Ag nanocrystals can even be easily formed at room temperature in the presence of a reducing agent [195]. Therefore, a high reduction temperature of 180 °C, as in CIS synthesis conditions, is not appropriate for AIS as Ag nuclei nucleate to form Ag nanocrystals.

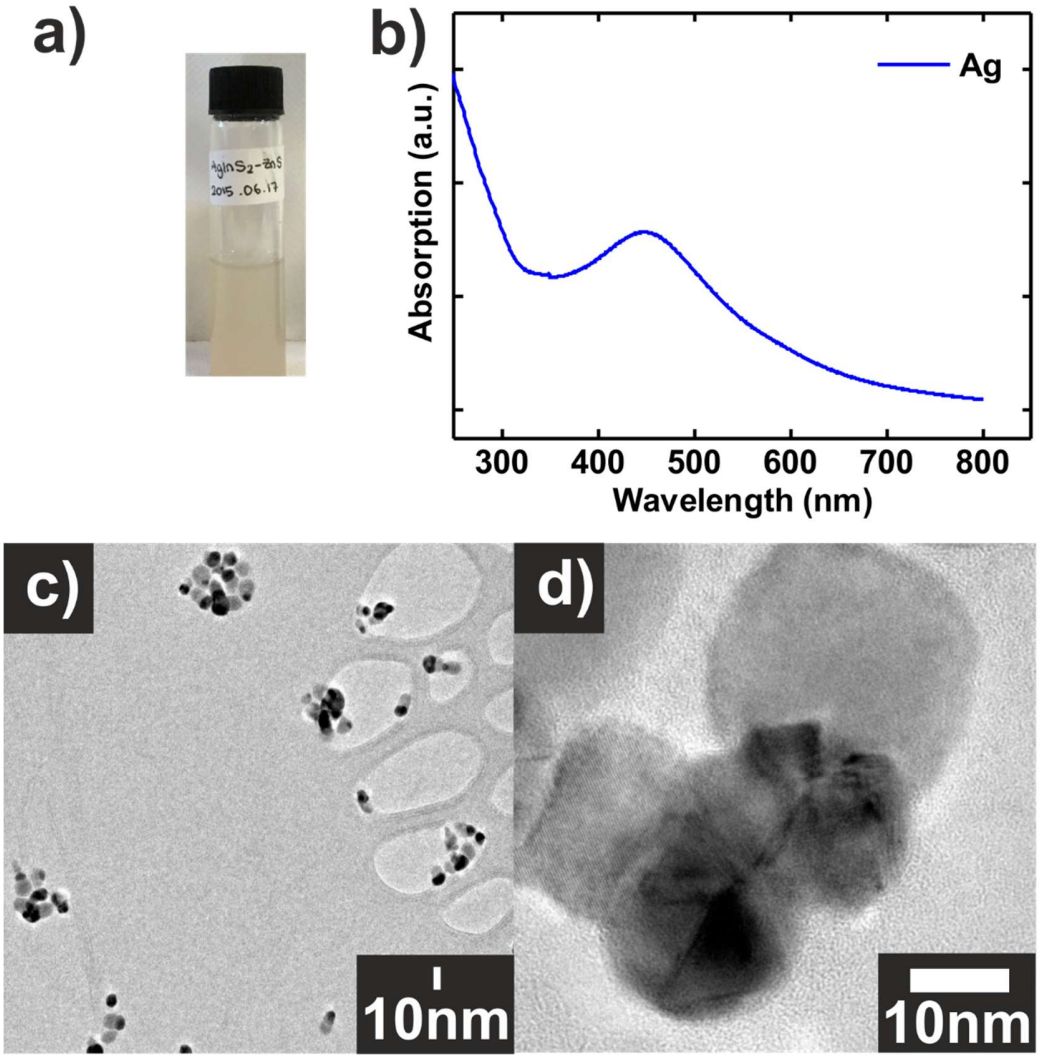

Figure 42- a) Picture of white precipitate dispersed in hexane b) Corresponding UV-Vis spectrum and c & d) TEM image of the precipitate. The UV-Vis peak at 450nm corresponds to the plasmonic resonance peak from Ag nanocrystals. From the TEM image various shapes are observed.

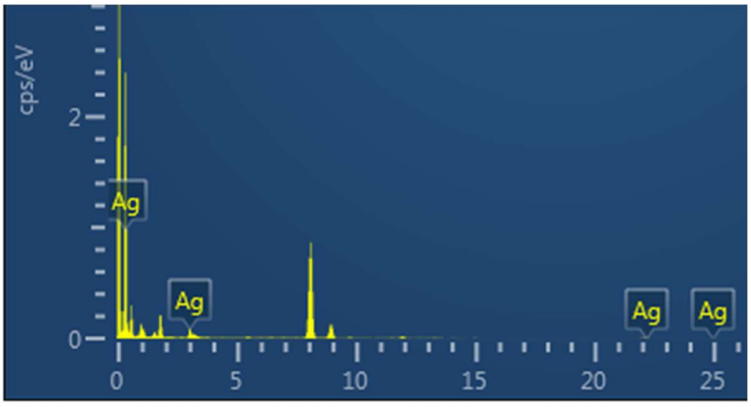

Figure 43- STEM-EDX elemental analysis graph taken from AZTEC software. Graph showing 100% Ag presence.

After the elimination of the black precipitate, HR-TEM was performed to observe the crystal structure of AIS nanocrystals. From this, Figure 44a shows AIS nanocrystals to be of a size equivalent to ~3nm. In Figure 44b, the FFT of the TEM image, shows that the pattern is consistent with a CP structure. AIS forms either a thermodynamically stable CP structure or metastable WZ [193]. From the TEM image in Figure 44c, the overall nanocrystal size distribution is in the range 2.5-3nm, demonstrating that polydispersity was significantly reduced through centrifugation.

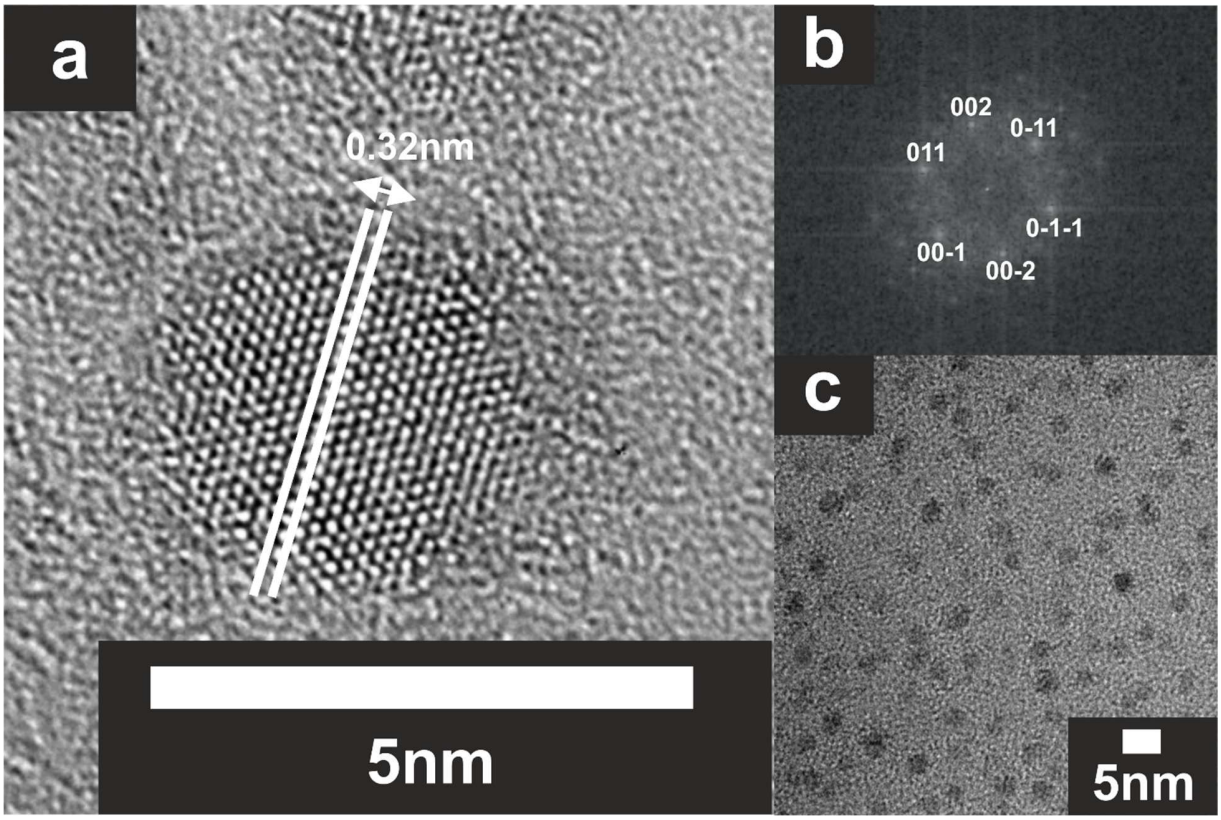

Figure 44- a) HR-TEM of AIS at 1.5Mx b) Corresponding FFT of TEM image labelled with indices of the chalcopyrite crystal structure c) Overall TEM image of nanocrystals size <5nm

5.5 Study of the synthesis dynamics with *in-situ* PL

From the preliminary synthesis, formation of by-products, like Ag and Ag_2S, was observed. This could possibly be attributed to the high reduction temperature (180 °C) setting that was used for CIS synthesis. To further investigate the formation process of AIS nanocrystals, *in-situ* PL was carried out. *In-situ* PL is a dynamic technique that makes use of a probe submerged into the reaction. For the purposes of the current work, it was employed to measure the PL emission peak changes from the point of TMSS injection at 30 °C to the final growth temperature of 130 °C. As a cleaning process was not involved and there was continuous observation monitoring, any changes during the rapid reaction process were captured. Consequently, *in-situ* PL yields a more accurate representation of nanocrystal growth changes than an aliquot PL study. However, aliquots were still taken for other characterisation techniques, namely UV-Vis, XRD, and STEM-EDX, that cannot be conducted dynamically.

To show the colour change from the initial TMSS injection point (at 30 °C) to the final reaction temperature (130 °C), aliquots were taken (Figure 45). Each aliquot was injected into a cold hexane solution to quench any further reaction from happening. A clear colour change from brown to bright orange was observed (Figure 45). Brown is an indication of either Ag_2S formation [193] or Ag-rich nanocrystals. Observation under UV light indicated nanocrystals changed from non-luminescing to bright orange with increasing temperature. Moreover, XRD and STEM-EDX analysis were employed to determine the composition and crystal structure changes.

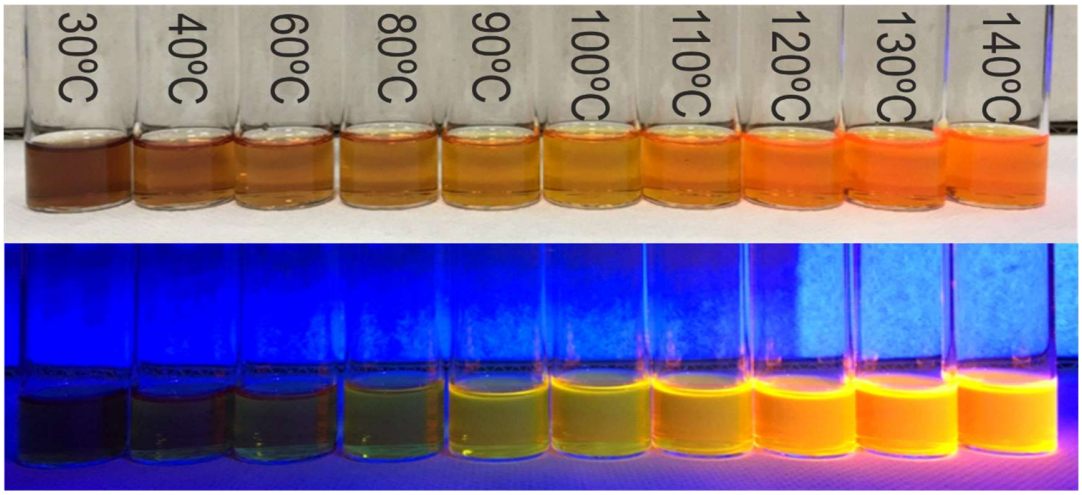

Figure 45- Aliquots were taken at temperatures from 30°C to 140°C. Initially upon injection (30°C) a brown colour is observed. As the temperature increases the colour changes to bright orange. A clear colour change and increase in PL emission is observed.

STEM-EDX was used to study the aliquots' composition (Figure 46). For TEM sample preparation, aliquots needed to be cleaned to remove any excess organic ligands. Unfortunately, during this process, some of the nanocrystals were inevitably lost. At the lower temperatures between 30 °C and 40 °C, after the first cleaning, the nanocrystal samples could not be re-dispersed in hexane, which implied that nanocrystals were not fully grown and unstable. Therefore, based on the loss of nanocrystals, the data may not be a direct representation of the nanocrystal composition, though nevertheless, interesting observations can be made. In Figure 46, the EDX data from each aliquot is plotted with a summary in Table 11. EDX percentage values were obtained by mapping different areas with STEM-EDX. INCA analysis software was used to detect the elements present and quantify the composition while excluding impurities. In order to increase the precision of measurement, each sample was measured in three different grid areas mapped for 30 mins. It could be seen that In content increased with temperature. Initially, at 40°C, In/Ag was 2.9 and at 130°C, In/Ag was 3.5. The initial precursor ratio between

In and Ag placed in the three-neck flask was 4. This demonstrated that the final composition was nearly similar to the actual precursor ratio added in the synthesis. As observed with the CIS injection temperature, In required a higher temperature for the reduction reaction to take place than Cu or Ag. Hence, as temperature increased, more In content was incorporated into the AIS [196,197]. Zhu *et al.* reported that Ag cations are "fluid-like" in a silver-rich AIS, easily forming Ag^{+} vacancies, thus quickly mediating In incorporation [198]. As In content increases with temperature increase, the number of defects in the structure also becomes more numerous, which results in higher DAP recombination. Therefore, overall PL emission becomes brighter (see Chapter 4 for CIS).

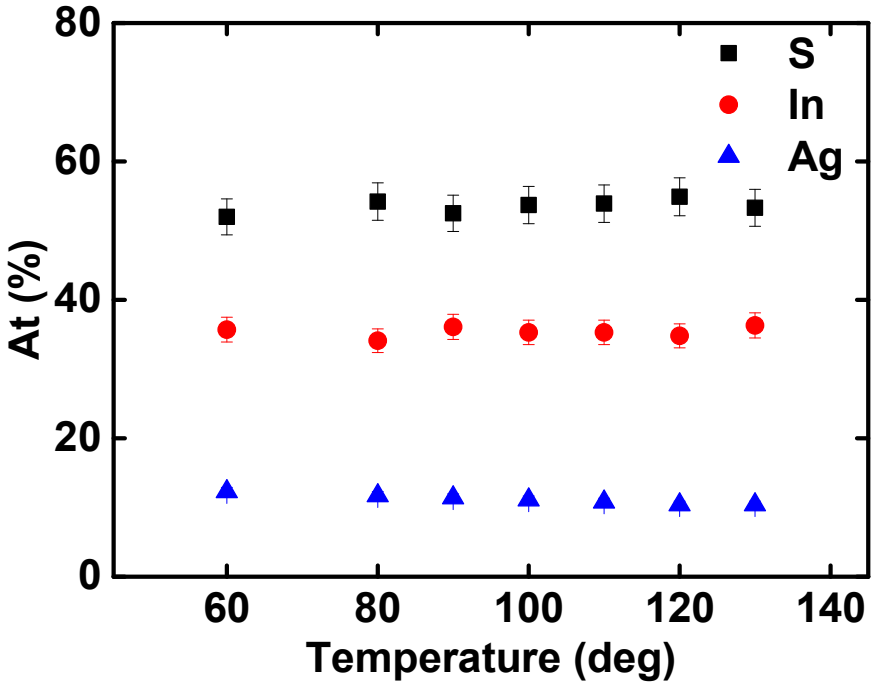

Figure 46- STEM-EDX of temperatures at 60, 80, 90, 100,110,120, and 130°C. Showing the relative atomic mass percentage of Ag, In, and S.

Table 11-Summary of Figure 46 STEM-EDX analysis. The In/Ag ratio increases with temperature, where reaching a ratio of 3.5 similar value as the precursor initially added (In/Ag= 4)

Temperature (°C)	60	80	90	100	110	120	130
S	52.0	54.2	52.5	53.7	53.9	54.9	53.3
In	35.7	34.1	36.1	35.3	35.3	34.8	36.3
Ag	12.3	11.7	11.4	11.1	10.8	10.4	10.4
In/Ag	2.9	2.9	3.2	3.2	3.3	3.3	3.5

XRD was conducted to understand the changes in the crystal structure of each temperature aliquot. From the XRD trace (Figure 47), it is observed that as the temperature rises, the peaks become more defined and sharper. The peak sharpening indicates the crystal structure becoming more defined. On the other hand, an increase in nanocrystal size will also lead to apparent peak sharpening, described by the Scherrer equation, as FWHM value decreases. With increasing temperature, nanocrystal size become larger and FWHM values decreases. However, there are new peaks forming at greater angles, which suggest that the changes are more influenced by crystal structure. This XRD data explains why emissions were not observed at 60°C with In/Ag = 2.9 (Figure 45). As determined from the XRD data, at 60 °C broad peaks are present, implying that the nanocrystals have poorly defined crystal structure. According to the CIS experiments in Chapter 4, at a ratio of 3:1 for In:Cu, some luminescence could be observed. However, although the In/Ag ratio may be sufficiently high, the poorly defined crystal structure will likely have a large number of non-radiative surface defects that prohibit PL emission. The number of these non-radiative surface defects is reduced with increases in temperature. Therefore, for instance, at 90 °C as compared to 60 °C, there

was only a difference of around 0.3 for the In/Ag ratio, but a sudden luminescence was observed for 90 °C and three XRD peaks become more defined.

The three XRD peaks correspond to the CP structure of AIS, where peaks of CP structure are normally observed at 26.7°, 44.8°, and 52.3° [199]. For AIS, the most common crystal structures are either CP or WZ. For the solution process, usually orthorhombic shapes are observed at high reaction temperatures, whereas CP is observed at lower temperatures [49].

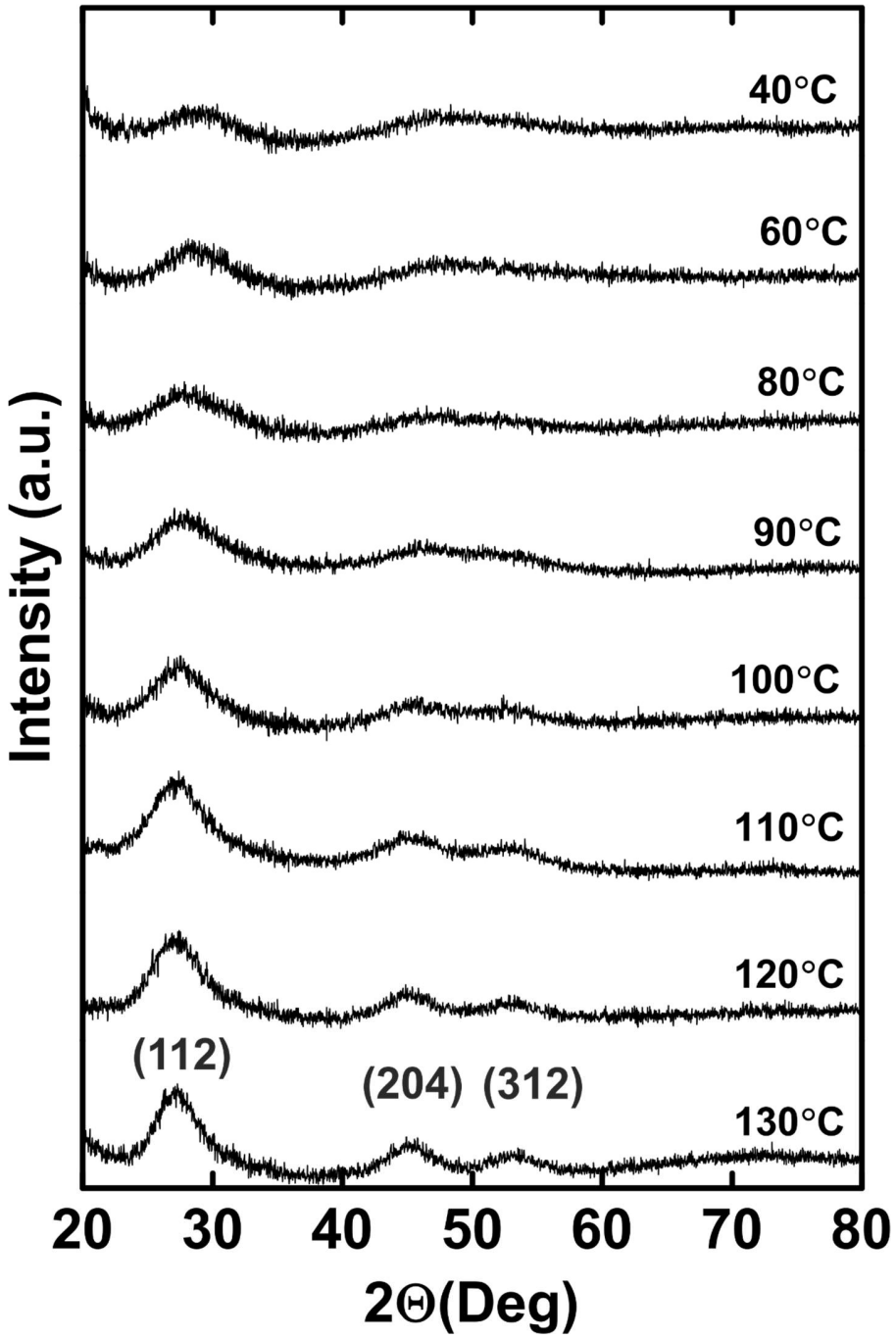

Figure 47- XRD of the aliquots taken at different temperatures during the reaction showing that AIS formed is a chalcopyrite crystal structure from the positions of the three peaks at 26.7°, 44.8°, and 52.3°, corresponding to the (112), (204), and (312) planes.

According to the Scherrer equation, the average size of the nanocrystals can be calculated.

The Scherrer equation is $t = 0.9\lambda/\beta\cos\theta$, where t is the grain size of the sample, λ is the

wavelength of the X-ray (0.154nm), β is the FWHM of the diffraction peak, and θ is the Bragg angle. Using the XRD peaks from the 130 °C injection temperature, the nanocrystal size is calculated to be 2.4nm, which lies in the range measured by TEM.

In Figure 47, it can be observed that XRD peaks are slightly shifted to lower angles with an increase in temperature. This can be related the increase in the In/Ag ratio as the reaction proceeds. Since the bond length of In-S is 5% larger [42], it increases the unit cell parameter, thus widening the crystal lattice [200].

Overall, Ag or Ag_2S by-products were not observed during XRD analysis. Ag nanocrystals have peaks at 38.2°, 44.5°, and 64.6°, with a face-centred cubic (FCC) structure. Ag_2S nanocrystals have a monoclinic structure with several peaks between 30° and 40° [201]. Peaks due to the by-products may not be present here as they are minority products relative to the AIS nanocrystals such that XRD is not sensitive enough to detect them. Alternatively, the by-products may have been lost during the sample preparation and cleaning processes.

As *in-situ* PL takes measurements every 10s and produces a total of 100 data readings, only a few of the relevant graphs were selected for every 20°C until 100°C, and from then on for every 10°C. For each PL reading, aliquots of the sample were taken for UV-Vis measurement. Figure 48 shows the PL emission graph and UV-Vis data. As temperature increases, on the absorption graph, a well-defined excitation peak was observed. This indicated a narrow size distribution or a reduced non-radiative recombination pathway [191], which aligns with the findings from the XRD data (Figure 47) that showed peak sharpening with a rise in temperature.

From the PL emission graph, interesting peak changes were observed (Figure 48). At 40 °C, two emission peaks appeared. The lower wavelength (~500nm) peak was due to In-rich nanocrystals. The higher wavelength (~700nm) peak is was from Ag-rich nanocrystals as a consequence of the pre-made Ag nanocrystals present (Figure 42) before injection. From 60°C to 80°C, the higher wavelength peak disappeared and only the lower wavelength peak remained. The higher wavelength peak decreased in size as there was more incorporation of Ag. A similar observation was seen with CIS nanocrystals, where an increase in Cu content diminished the PL emission [42]. This was mainly because of the decrease in defect concentration, where with increased Cu (or Ag), donor and acceptor states are reduced, limiting the recombination sites. Simultaneously, the lower wavelength peak began to red-shift as nanocrystals increased in size. However, at the same time, the peak intensity increased as the crystal structure became more defined, decreasing internal defects that may induce non-radiative recombination. Furthermore, as focused (diffusion-controlled) growth occurs over time with increasing temperatures [191], nanocrystals grow from the remaining unreacted precursor and form more monodispersed nanocrystals [85].

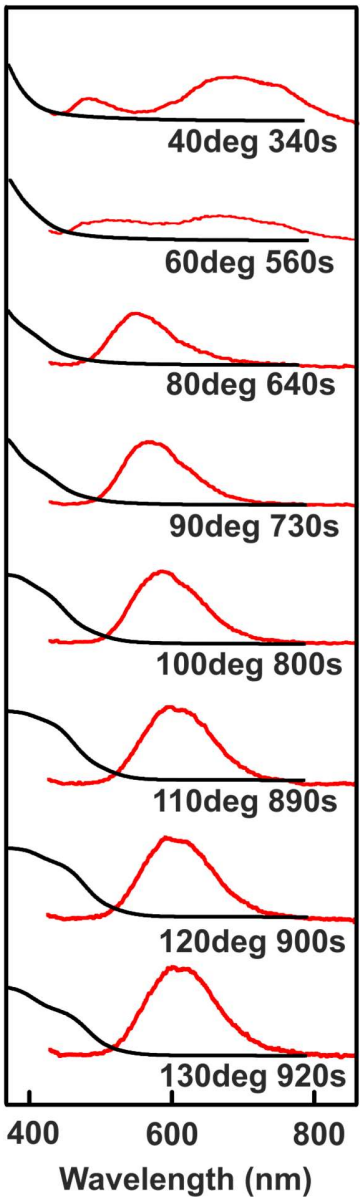

Figure 48-In-situ PL graphs plotted with corresponding UV-Vis spectra. Two peaks are observed at 40°C, but as temperature increases only single peak at ~590nm remains at 80°C. The peak shifts to higher wavelength with increasing temperature.

To understand the changes in PL emission peak in greater detail, FWHM and PL peak wavelengths were plotted (Figure 49). FWHM decreases exponentially with increases in temperature beyond 60 °C. This confirmed that the size dispersity of the nanocrystals was decreasing. Plotting the maximum peak of each PL of In-rich graphs, it was observed

that the peak continued to shift to a higher wavelength with rising temperature. This is a typical phenomenon of red-shift based on the growth of nanocrystals size [90]. Figure 50 shows the analysis of nanocrystal size distribution for 90 °C, 110 °C, and 130 °C, which supports that nanocrystal size increases with temperature.

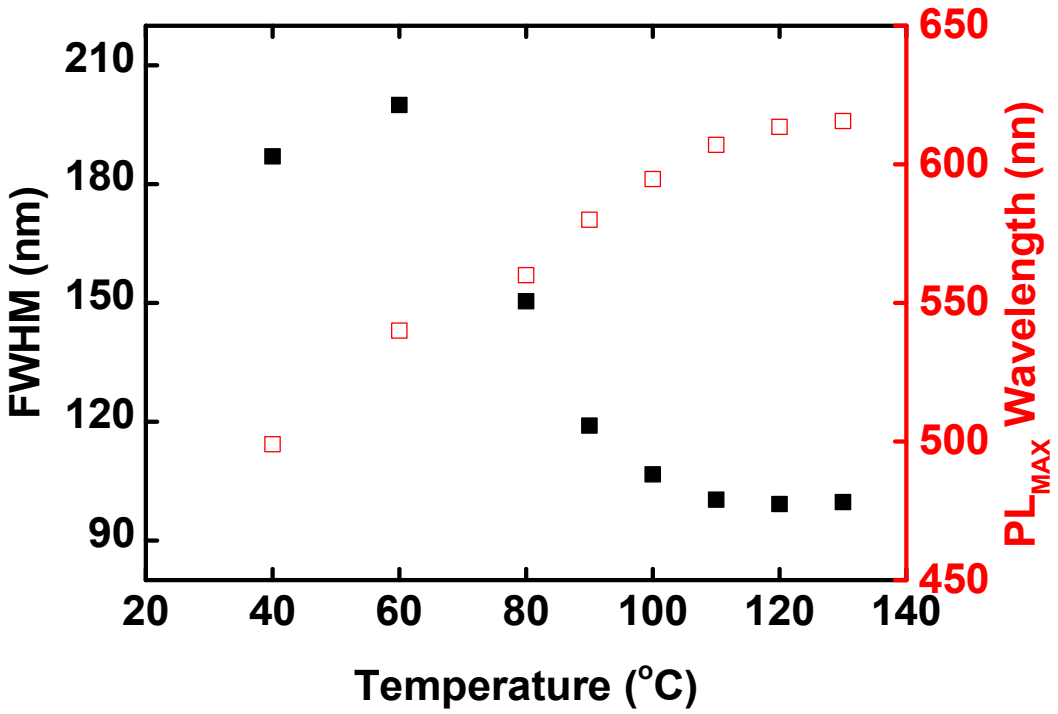

Figure 49- Graph representing FWHM and PL peak wavelength of the data from PL emission of in-situ PL study. FWHM decreases exponentially with increase in temperature after 60°C. While, PL peak red shifts up with increase in temperature as nanocrystals size grows.

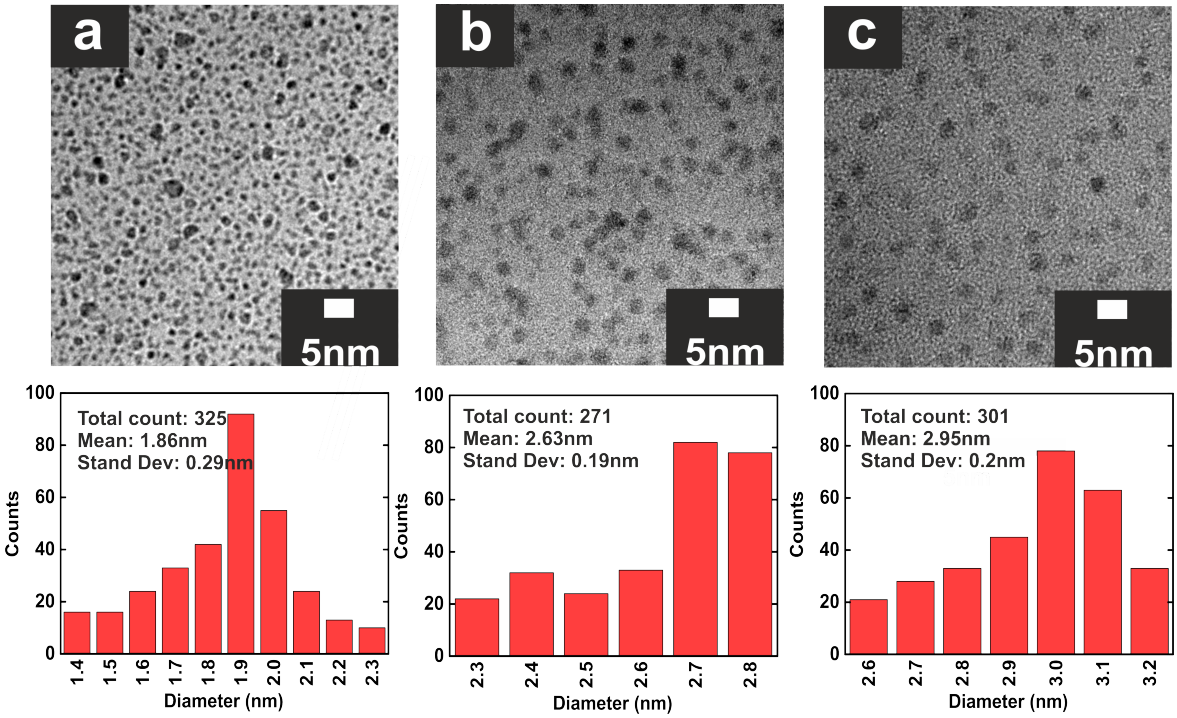

Figure 50- Size distribution of different temperatures a) 90°C, b) 110°C, and c) 130°C. Each TEM represents a far view image of a single area of the sample. Image J was used to measure size of the nanocrystals in various sample areas.

Using the aliquots taken during the *in-situ* PL, PLQY was calculated and plotted with In/Ag content ratio data taken with STEM-EDX from Figure 46 against temperature changes (Figure 51). PLQY was measured according to the same procedure outlined in Section 3.3.4.

As expected based on the image from Figure 45, PLQY increased with temperature. From the two plots (Figure 51), it could be seen that the In/Ag ratio increased overall in a linear manner, whereas PLQY rose exponentially. This is indicative of the fact that PLQY is not solely related to increases in DAP recombination. Based on the findings from the XRD and PL (FWHM) analyses, PLQY is affected by two other factors. First, an increase in crystallinity reduces non-radiative recombination as the nanocrystals' non-radiative defects decrease. Second, the decrease in dispersity of nanocrystals by removing the by-

products or a decrease in size variation with growth incorporates remaining precursors in solution.

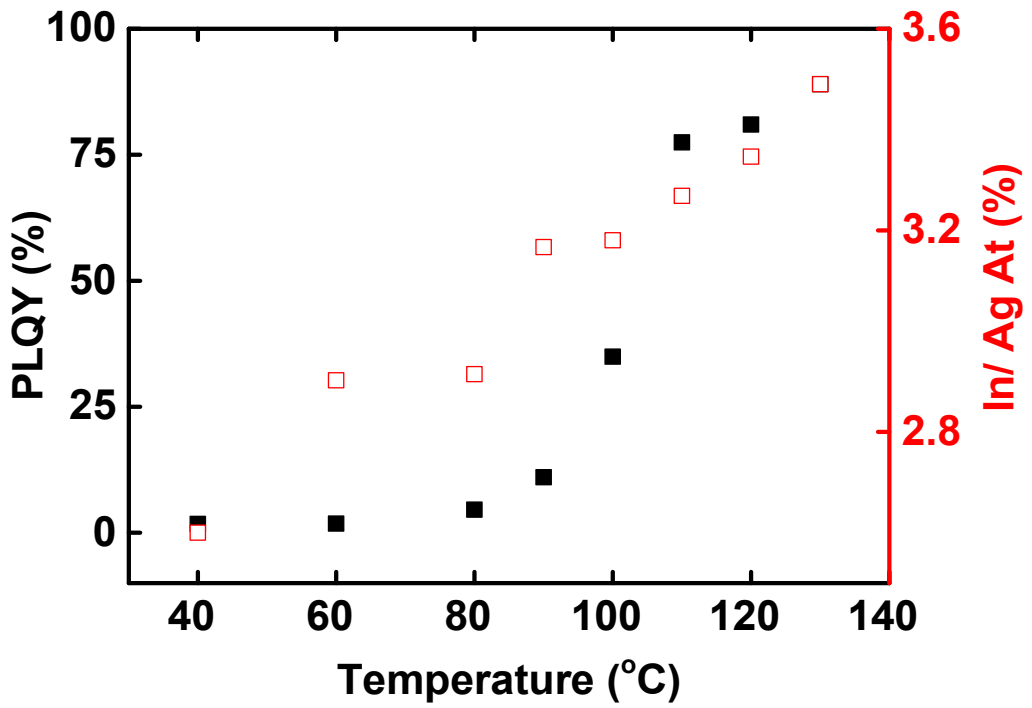

Figure 51- Aliquots from in-situ PL are characterized to measure PLQY and In/Ag content from STEM-EDX. PLQY increases exponentially, while In/Ag content increases linearly showing that PLQY is not solely dependent on the In content.

5.6 Lowering the injection temperature to reduce by-product formation

From the previous section (Section 5.4), it was found that removing the by-products, Ag and Ag_2S, was crucial to achieve a high PLQY. Although centrifugation was used to remove a significant amount of the large Ag_2S, some small-sized by-products were still left as different Ag nanocrystal sizes were shown to form (Figure 42). Therefore, elimination or reduction of Ag nanocrystals is important for enhancing the PLQY of AIS nanocrystals.

So far, based on studies from the literature, the highest PLQY achieved for AIS was 15-20% [202], and in most of the literature, the highest PLQY was accomplished through a ZnS shell. For AIS-ZnS, the highest PLQY was between 40-80% [75, 203]. With further treatment of AIS-ZnS by ligand exchange [101] and post-synthesis treatment [111], the PLQY reached 80%.

In this section, to further improve the 66% PLQY, which was obtained by removing Ag_2S (Table 10), the influence of the reduction temperature was examined. Additionally, other halide precursors were studied to determine their influence on PLQY.

The initial reduction temperature of 180 °C was based on the temperature from CIS synthesis. However, this temperature was not suitable for Ag, since Ag nanocrystals can easily form at even very low temperatures. To avoid formation of Ag nanocrystals, the reduction temperature was lowered to 150 °C. However, any temperature lower than 150 °C has been shown to affect the In reduction process and would result in the requirement of a longer reaction time.

Figure 52 shows the *in-situ* study of two different reduction temperatures. The top of Figure 52 shows the PLQY using a reduction temperature of 180 °C and the bottom of

Figure 52 at 150°C. For the sake of an easier comparison, the 180 °C sample will be called the high sample and 150 °C will be called the low sample.

Comparing the two sets of data in Figure 52, it is clear that the double peaks observed at 40 °C in the high sample are not present for the low sample. For the low sample, at 40 °C a single peak starts to form around 600nm. The Ag-rich nanocrystals with PL at 700nm seen with the high sample are not present as Ag nanocrystal formation is suppressed. Furthermore, based on naked eye observation, the white precipitates observed during the cooling stage reaction was barely observed in the low sample.

The remainder of the process after 80 °C was observed for both low and high samples - in both cases, a red-shift in wavelength was observed because of the growth in nanocrystal size with rising temperature.

After the cleaning process, both samples were centrifuged to remove any Ag_2S nanocrystals present. For both the high and low samples, black precipitate was present, but in the low sample, there was less than half the black precipitate found in the high sample. Although lowering the reduction temperature did not fully resolve the problem, it showed that it influenced the overall quantity of by-product formation.

Figure 53, shows the PL peak of Ag_2S taken from literature. The S4 sample emission wavelength at 727nm compares most closely with the black precipitate as it has particles that are similar in size (as seen in Figure 40). This data supports that the PL peak observed in Figure 52 at 700nm is related to Ag_2S nanocrystal emissions.

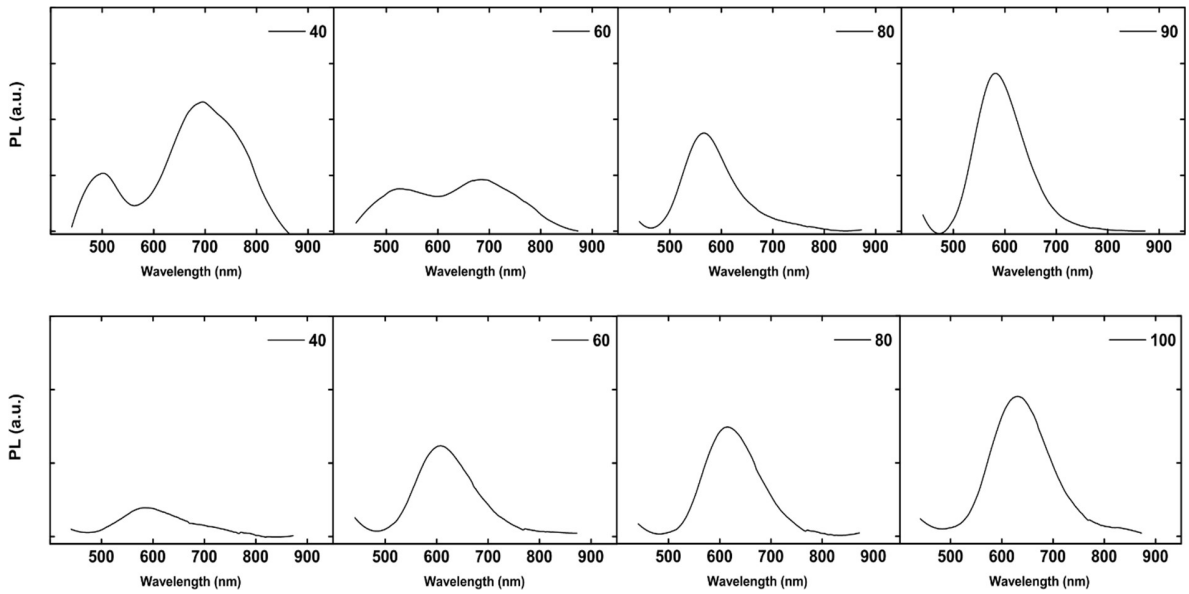

Figure 52- Comparing the effects of reduction temperature on nanocrystals formation. ***Top*** *a reduction temperature at 180°C, where double peaks are observed at 40°C.* ***Bottom*** *is at 150°C, from the beginning double peak is not present.*

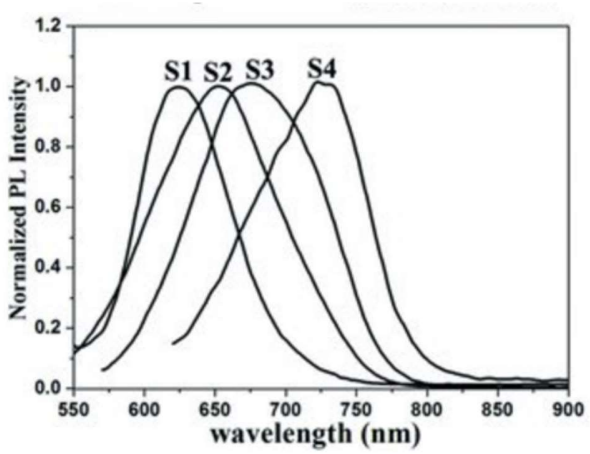

Figure 53- Showing PL peak of Ag_2S sample. Each peak represents different size of Ag_2S nanocrystal. S1 1.7nm, S2) 2.1nm, S3) 3.0nm, and S4) 3.7nm. To compare Ag rich AIS nanocrystal from Figure 52, S4 sample should be used as it is similar in size. Figure reproduced from reference. [204]

Similar to the CIS halide precursor studies in Chapter 4, different AIS halide precursors were tested to determine whether comparable observations could be made. Unlike CIS, only two different halide precursors could be used. Further characterisation may be

required to understand this phenomenon. Therefore, using bromide and chloride precursors, four different combinations were examined. For each halide combination, synthesis were repeated five times to assess reproducibility and reliability.

To achieve high PLQY based on the DAP recombination theory, the higher the imbalance of the Ag:In ratio (In content being higher), the greater there is radiative recombination through DAP recombination pathways. Therefore, slower Ag reactivity and faster In reactivity is the best combination to produce high off-stoichiometry. Similar to CIS, based on the HSAB theory, a combination of Ag (soft acid)–halide precursor (soft base) and In (hard acid)-halide precursor (soft base) should be made use of. Therefore, as bromide is a softer base than chloride, the most ideal combination for [Ag-In] in terms of the highest In content would be on the order of [Br-Br]→ [Cl-Br]→ [Br-Cl]→ [Cl-Cl].

Based on the STEM-EDX analysis of the four combinations, In/Ag content increases (Table 12) were in agreement with what was predicted. [Br-Br] exhibited the highest In/Ag content whereas [Cl-Cl] had the lowest.

Table 12- Summary for STEM-EDX data for four different halide precursor combinations for AIS synthesis. By using the halide precursor relative reactivity, the combination with the highest In content can be predicted. The results are as predicted in the order of [Br-Br]→ [Cl-Br]→ [Br-Cl]→ [Cl-Cl] from high to low In content.

	Atomic weight percentage (%)			
	Br-Br	**Cl-Br**	**Br-Cl**	**Cl-Cl**
Ag	14.10	13.40	12.90	13.50
In	55.71	50.86	45.15	44.10
S	30.19	35.74	41.95	42.40
In/Ag	3.95	3.80	3.50	3.27

However, from the PLQY analysis of the four combinations (Figure 54), the prediction that high In content will also correspond with high PLQY values was not as expected, similar to the results from Chapter 4 for CIS nanocrystals (Figure 35). The [Br-Br] sample had lower PLQY values than those with [Cl-Br] (Figure 54). This is because further down the periodic table, the halides become more voluminous and less passivating [181]. Cl is smaller than Br, so samples with Cl will have better surface passivation. As [Br-Br] and [Cl-Br] have similar In/Ag ratios, but because [Cl-Br] contains chloride, fewer surface defects were present. Therefore, [Cl-Br] would have an overall higher PLQY.

With the halide precursor combinations (Figure 54), it was found that the highest PLQY reached was 89% using the [Cl-Br] combination. So far, based on the previous literature findings [205], this is the highest PLQY achieved with just core synthesis of AIS nanocrystals. The average of the four samples for PLQY was approximately 66% (Figure 54), which is still higher than the 15-23% reported previously [202]. Therefore, this is demonstrative of the new synthesis with the low-injection temperature technique being an efficient synthesis for achieving high PLQY.

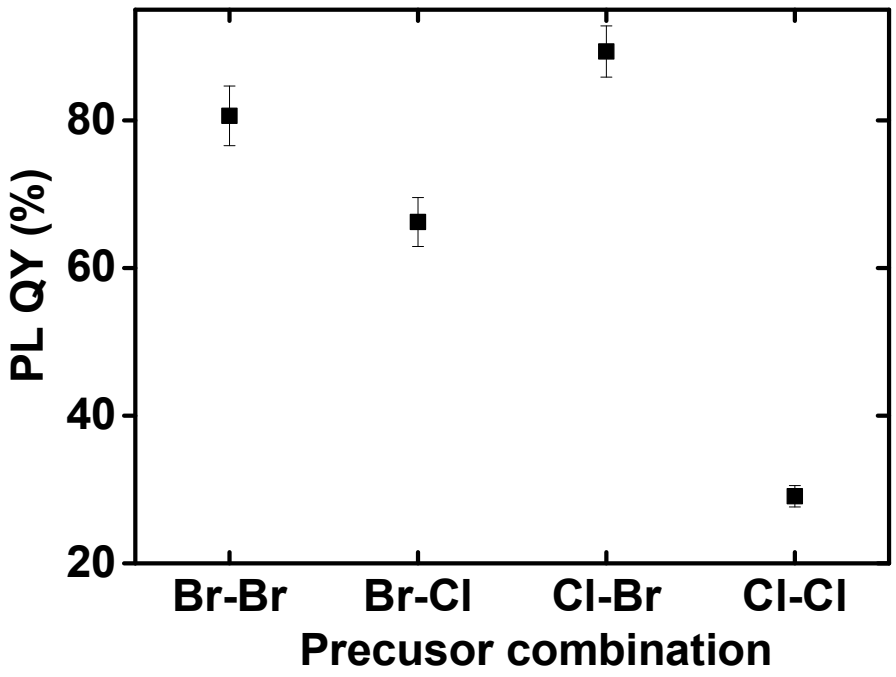

Figure 54- PLQY of four different halide precursor combinations for AIS synthesis. The highest PLQY (89%) was achieved with a [Cl-Br] combination. Taking the average of the four precursor samples, overall of 66% of PLQY is achieved.

5.7 PL lifetime

One of the major characteristics of DAP recombination is the long PL lifetime. Experimental methods for determining PL lifetime can be found in Section 3.3.6. AIS nanocrystals tend to have a long PL lifetime - between 150 to 350ns [206, 69]. Here, a bi-exponential function [72] (equation found subsequently) was used to fit the data, where A_1 and A_2 are amplitudes and T_1 and T_2 are lifetimes. The average PL lifetime is contributed by fast decay and slow decay, which are surface (T_1) and intrinsic (T_2) defects [69]. Using the equation, it was found that the average lifetime was ~320ns, which fits within the range found in the literature [101]. For binary CdSe nanocrystals without DAP recombination pathway, the average PL lifetime is ~20ns [41]. The long PL lifetime supports the idea that the main recombination pathway for AIS nanocrystals is DAP recombination. This long PL lifetime can be useful for applications that require a delay between excitation to emission, like, for example, biomedical applications.

$$\tau_{ave} = (A_1(\tau_1)^2 + A_2(\tau_2)^2)/(A_1\tau_1 + A_2\tau_2)$$

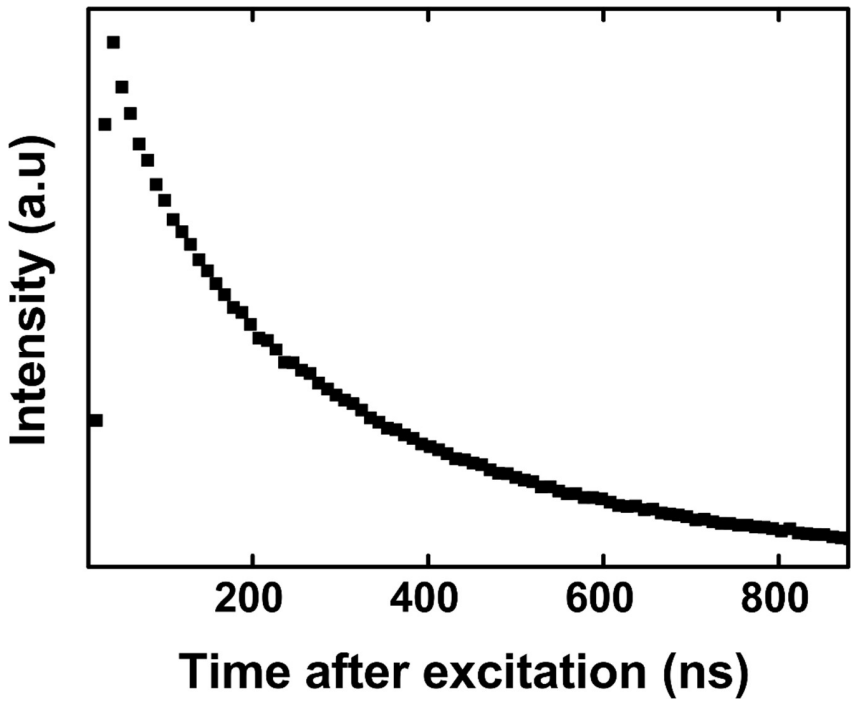

Figure 55- Graph representing the PL lifetime of $AgInS_2$

5.8 Conclusion

Based on the understanding from Chapter 4 of CIS synthesis, a new synthesis method for AIS was formulated using only halide precursors. In reviewing the current literature on AIS, there has not been much research performed or synthesis developed previously. This chapter used *in-situ* PL to understand AIS nanocrystal formation. Removal of reaction by-products gave rise to an increase in PLQY.

From the initial synthesis, it was found that by-products, such as Ag and Ag_2S nanocrystals, were formed, which reduced the overall PLQY. To reduce the number of Ag nanocrystals to avoid Ag_2S formation, the reduction temperature was lowered from 180 °C to 150 °C. Although Ag_2S nanocrystals were still detected, the quantity was reduced by approximately 50%, indicating overall improvement.

To further increase the PLQY, four different halide precursor combinations were studied using bromide and chloride halide precursors. From STEM-EDX and PLQY analyses, it was observed that the combination of both high In/Ag ratios and the presence of chloride halide was required to achieve a high PLQY. In the work presented here, the highest PLQY achieved was 89% for AIS core nanocrystals. Therefore, AIS alone without a shell features great potential as a replacement for Cd-based toxic luminescing nanocrystals for diverse future applications, such white light-emitting diodes, bio-imaging, or solar cell concentrators.

Chapter 6 –$AgInS_2$ Luminescent Concentrator

6.1 Introduction

Luminescent concentrators (LC) absorbs light, which is then re-emitted by a fluorescence process and guided to an edge. Typically, LC have been used to concentrate light into solar cells [9]. In the current chapter, this concept is extended to build a light antenna for visible light communication (VLC) [10].

Herein, AIS nanocrystals synthesised in Chapter 5 will serve as the luminescing material for the concentrator. The optoelectronic properties of AIS, which has a high PLQY, large Stoke shift, and large absorption coefficient, are the desired properties for VLC concentrators.

In order for light to be concentrated to the edges, total internal reflectance (TIR) needs to occur in the concentrator layer. Therefore, the transmitting lights need to pass from a high refractive index to low refractive index. For these refractive indices to match, the base polymer for the concentrator layer is $n \cong 1.5$.

As the concept of LC using AIS is novel, herein, the fabrication method of LC was studied. Various polymers were tested to find a compatible polymer that will disperse the nanocrystals evenly, has high clarity, and forms a smooth surface. Furthermore, to increase light concentration, new structures were assessed to minimize the loss of light.

6.2 Method

6.2.1 Concentrator fabrication method

Structure of the concentrator

To optimise performance, a series of structures were fabricated as shown in Figure 56. To enhance the performance, a low refractive index layer was placed below the polymer composite. Additionally, a mirror layer was added at the bottom to reflect light that has not been absorbed on first pass, this was done by evaporating an aluminum (Al) layer, using vacuum thermal evaporation.

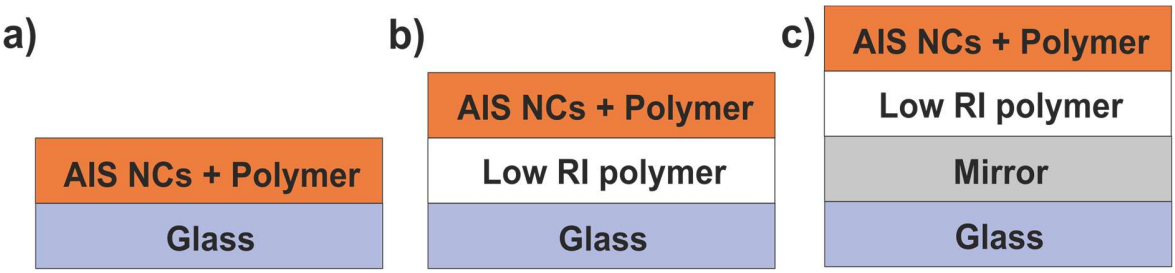

Figure 56- Schematic of the 3 structures that are fabricated. Based on the conventional structure additional layers are added to study the enhancement of total internal reflectance. a) Conventional concentrator structure b) Low refractive index polymer added c) mirror layer added

Preparation of glass substrates

Two types of glass substrates were used. For the first part of the characterisation, a standard microscope slide was used. For the second part, the gain measurement, a special cross-shaped cut glass substrate was used. This was to fit the special detector built for measuring all 4 edges at the same time, shown in Figure 57. After depositing the layers, a second glass substrate was placed on the top to encapsulate and protect the polymer layers.

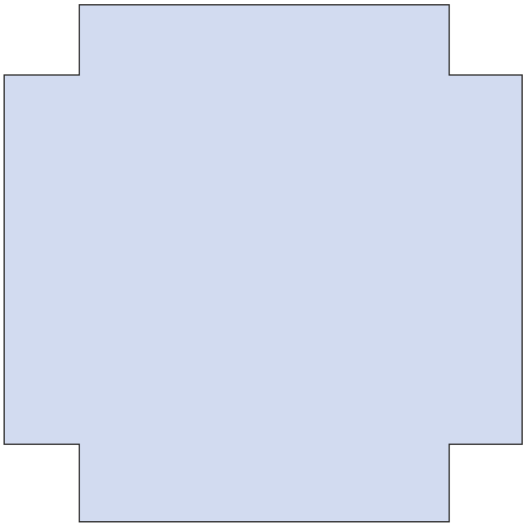

Figure 57- Schematic of the specially cut cross-shaped glass to measure 4 sides

The glass substrates were cleaned through the following steps; DI (distilled water) + Decon → DI → Acetone → Isopropanol, each step was sonicated for 10mins at 60°C. Afterwards, the glass was plasma-treated using Nanotech PLASMOD, purged with O_2 gas. This process cleaned the surface and increased its wettability.

Preparation of luminescing layer

The luminescent composite layer was prepared by mixing AIS with a host polymer. The polymer was required to adhere the nanocrystals onto the substrate, and to build thick layers through which light can be guided. Thickness was controlled by increasing the viscosity (concentration) of the polymer (2, 4, 6, 8, and 10mg/ml) and using different deposition techniques. After deposition, the film was dried under ambient air, while being heated at 60°C to remove residual solvent. The film thickness is crucial as there is a limit to how thin a photodiode, located on the edge of the sample, can be. Therefore, for direct comparison between using a concentrator and using a plain photodiode, the

thickness of the concentrator layer should be as thick as possible in order to be similar to a photodiode. Here, the maximum thickness deposited was 0.1mm.

To obtain a thick, uniform, and smooth luminescing layer, two different methods were used to make the film: drop casting and doctor blading.

Drop casting is a simple process whereby a certain amount of AIS polymer composite is poured onto the substrate and dried while being loosely covered to prevent any dust contamination. The thickness of the film is controlled by the volume poured and viscosity of the polymer.

Doctor blading is a technique which is used to coat large areas. The mechanism involves feeding the polymer behind the blade. As the blade passes over the substrate, the excess polymer is pushed out through the gap between the blade and substrate. The height of the gap and viscosity of the polymer determines the thickness of the film [207].

Low refractive index polymer

Most low refractive index polymers have fluorine groups, making them extremely hydrophobic, which inhibits the deposition of the next layer on top. Here, nafion (Aldrich) was used as the low refractive index polymer. It has a refractive index of 1.38 and is tetrafluoroethylene based with sulfonated side groups, making the polymer less hydrophobic. Due to its viscous nature, it was deposited by spin coating in order to achieve a uniform film. The rotation speed was 2000 rpm and the resulting film was dried at 120°C for 30mins to evaporate the remaining solvent.

Mirror layer

The mirror layer was fabricated by thermal evaporation of Al. Thermal evaporation is a physical vapour deposition technique, where a metal source is evaporated by heating in a low-pressure environment. The evaporation was carried out with an Edwards 306 evaporator at a base pressure of ~ 1.0×10^{-5} Torr at a rate of 0.1nm/s, as monitored by a quartz crystal. A total of 150nm of Al was evaporated.

6.2.2 Polymer selection and preparation

Polymer selection

Important characteristics of LC as mentioned in Section 2.6.3, is high PLQY (near unity), with large Stoke's shift to reduce reabsorption, photostability for long device lifetime, and short PL lifetime for quick response. In order to achieve this, host polymer used to mix the AIS nanocrystals needs to disperse the nanocrystals without affecting their properties and to avoid aggregation. Five different polymers, ethyl cellulose, polystyrene (PS), poly(ethylene)oxide (PEO), polycaprolactone (PCL), and Nail polish were tested. The properties are summarised in Table 13. They were chosen based on their solubility in a non-polar solvent, low melting point, smooth film formation without forming aggregates, high transparency, high abundance, and high refractive index. Refractive index is important as it needs to match the refractive indices of other layers to build a TIR in the nanocrystal layer, as discussed in Section 2.6.2.

Nail polish was chosen as it contains chemicals that form transparent smooth films. To list its chemical components, the base solvent is toluene, the film former is nitrocellulose, and plasticizer is dibutyl phthalate [208]. The various colours of nail polish were made

simply by adding a dye. Based on this idea, nail polish was used to see if a similar result can be induced using AIS nanocrystals.

Table 13- Summary of the 5 polymers with their melting point in toluene and refractive index (RI)

Number	Polymer	Melting point in Toluene (°C)	Refractive index
1	Ethyl cellulose	60	1.47
2	Polystyrene	70	1.49
3	Poly(ethylene)Oxide (PEO)	65	1.45
4	Polycaprolactone (PCA)	60	1.43
5	Nail polish	N/A	N/A

Polymer preparation

For the first four polymers listed in Table 13, toluene was used as the solvent. Nail polish was used without any modifications. For the initial part of the experiment, each of the four polymers were prepared to make 6wt% in toluene. Here are the preparation steps;

1.) 0.6g of polymer was dissolved in 9.4g of toluene to make 6wt%.

2.) Each of the samples was heated and stirred in an oil bath at 60°C for two hours. After all the polymer powder was dissolved, the solution was cooled to room temperature.

3.) 0.1ml of AIS nanocrystal with concentration of 3mg/ml dispersed in toluene was added to 5ml of polymer sample. 5ml volume was based on the amount required to cover the glass substrates.

4.) The mixture was stirred at room temperature for another 30mins to ensure all nanocrystals were dissolved without formation of aggregation.

5.) Finally, it was degassed under vacuum to remove any air bubbles trapped inside the solution.

Finally, after testing the polymer and AIS nanocrystals' compatibility, ethyl cellulose was chosen as the best film forming host polymer. This will be discussed in Section 6.3 results and discussion. Ethyl cellulose was used to further study the influence on film characteristics of changing polymer and nanocrystals concentrations.

Two sample batches were prepared using the same process as above. 1.) Ethyl cellulose 2, 4, 6, 8, and 10wt% were prepared and mixed with the same concentration of AIS nanocrystals (3mg/ml). 2.) Using 8wt% ethyl cellulose, 3 different concentrations of AIS nanocrystals 1, 3, and, 9mg/ml were prepared in toluene, from each of it 0.1ml were pipetted and added to study the effects of concentration. Since refractive index of ethyl cellulose is large (n=1.47), by adding nanocrystals it will increase further. Therefore, based on the theory, it was assumed that TIR will occur within the luminescing layer.

6.2.3 Characterisation

The characterisation tools used in this chapter are summarised in this section. The mechanism and operation procedures are outlined.

Reflectance

Reflectance measures the amount of light that is reflected by the surface. The reflectance can indicate the roughness of the surface and its glossy appearance. The concentrator requires a smooth and low reflectance surface in order for the light to be absorbed and TIR to occur.

There are two types of reflection, diffusive and specular. Diffusive reflection is light reflected at many angles this is observed in a non-homogeneous or rough surface. Specular reflection is light reflected at a specific angle from the incident light which occurs at metal or glossy surfaces. An ISP-REF integrating sphere from Ocean Optics is used to measure both diffusive and specular reflection. It has a built-in tungsten halogen light source. The inner part of the sphere is coated with Spectralon, which is a white diffusing material that provides a highly reflecting surface. The sample was placed on top of the light source covered with a black cardboard paper. Any light that was reflected from the surface was bounced inside the sphere which was detected using an Ocean Optics USB4000-FL spectrometer (ocean optics). All measurements were compared to an Ocean Optics WS-1 reflectance standard, that has >98% reflectance between 250-1500nm. For background reference measurement, the reflectance of the glass substrate used was measured.

Diffusive Transmittance

Diffusive transmittance measures the amount of incident light that has transmitted through the sample in all angles. To find the most transparent polymer, all five polymers without nanocrystals were first tested to study their inherent characteristics. The polymer-nanocrystal composite was then measured in order to see how the transmittance changes with nanocrystals present.

Transmittance was measured using the ISP-REF integrating sphere with an external light source to shine a light on the top side on the sample. The integrating sphere was used to detect all the light that has passed through the sample. The USB4000-FL spectrometer

was used to collect the light detected. For the background reference, a clean microscope slide was used.

MicroXAM

MicroXAM is an optical microscopy that uses phase shifts of light reflected from the sample to provide a non-contact 3D mapping of the surface. Here an Omniscan MicroXAM 5000B with a lateral resolution of ~1μm and vertical resolution of~1nm was used to study the surface of the polymers. Two parameters Sp, maximum peak, and Sa, the arithmetic average of 3D roughness were measured. Sp detects the maximum height in the Z direction of the measured area. The Sa parameter is expanded from the 2D roughness value where it measures the surface roughness based on the absolute values in three-dimensions. All the MicroXAM measurements were conducted by Assia Kasdi, a colleague in our lab.

DEKTAK

DEKTAK is a contact surface profilometry technique. It can be used to measure the thickness of a sample at a sample edge, where the step height was measured by a stylus dragged across a certain distance. The machine used, a Veeco DEKTAK 6M, has a vertical resolution <1nm, therefore, it is suitable for measuring thick film thickness.

Following steps were taken for measurement (specific parameters used in DEKTAK are summarised in Table 14). 1.) Prepared polymer sample was scratched using a blade. 2.) A rough DEKTAK measurement was taken to check the surface placed horizontally and the stylus force was adjusted not to damage the polymer. The polymers were dried firm so the stylus force did not have an effect. 3.) Stylus length was set to scan both of the

polymer and the underlying substrate area. For measurement accuracy, 5 measurements were taken and the mean value was calculated. 4.) Software provided by DEKTAK was used to calculate the step height.

Table 14- Summary of the specific parameters used in Dektak

Parameters	
Scan length	6000 µm
Scan duration	60 sec
Stylus force	3 mg
Profile	Hills & valleys
Stylus radius	12.5 µm

Flood/Full illumination

To measure the light transmitted to the edges, flood/full illumination was used. The setup is shown in Figure 58. This technique was used to measure the PL emission at the edges by shining a 420nm blue light source (Thorlabs- M420F2) onto the large concentrator area. A fiber was fixed onto the edge of the concentrator, and the other end was connected to the spectrometer where the detected light was measured. The distance between the light source and the concentrator was fixed at 20cm to allow the light to be scattered and cover the entire surface of the concentrator.

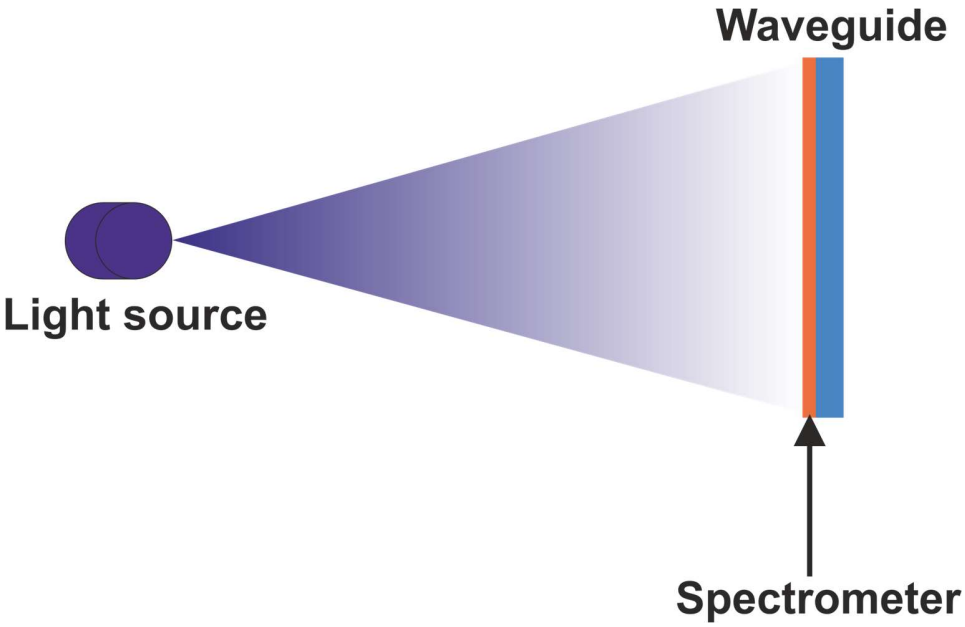

Figure 58- Schematic of the full illumination set up. A fibre connected to the spectrometer is fixed at the edge of the concentrator to measure light transmitted.

To ensure only light from the edge of the concentrator is detected, the glass sides were painted with a black permanent marker as shown in Figure 59.

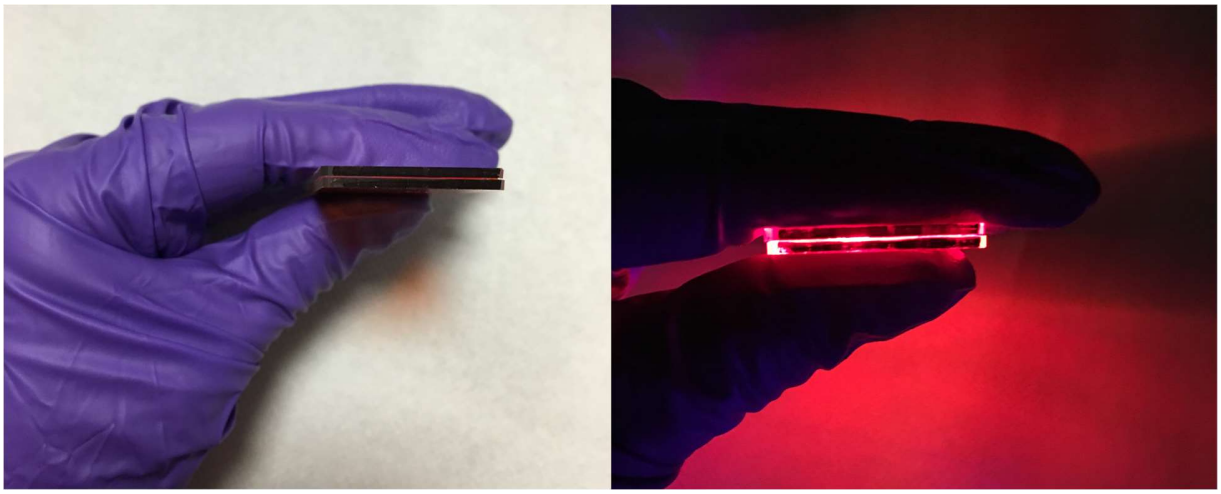

Figure 59- Picture showing sample cross-section before and after illumination. The glass is painted with black permanent marker to detect light only from the concentrator polymer layer.

Spot illumination

Spot illumination is used to measure the amount of light detected relative to the distance of the light source along the concentrator. It is used to study the effects of reabsorption. Spot illumination has a similar set-up to flood illumination. The difference is that the light source is a spot, as seen in Figure 60. The blue light source, 420nm (Throlabs), was connected to a fiber and fixed in place. In between the light source and substrate, a converging lens was placed to keep the spot size at 0.5cm. The PL emission was detected at the edge, while the spot was moved from one edge to the other. The edge close to the detector will be named, near edge, while the opposite edge will be called far edge. The distance between near to far edge was measured to be 40mm. For every 4mm distance, the measurements of PL emission was taken.

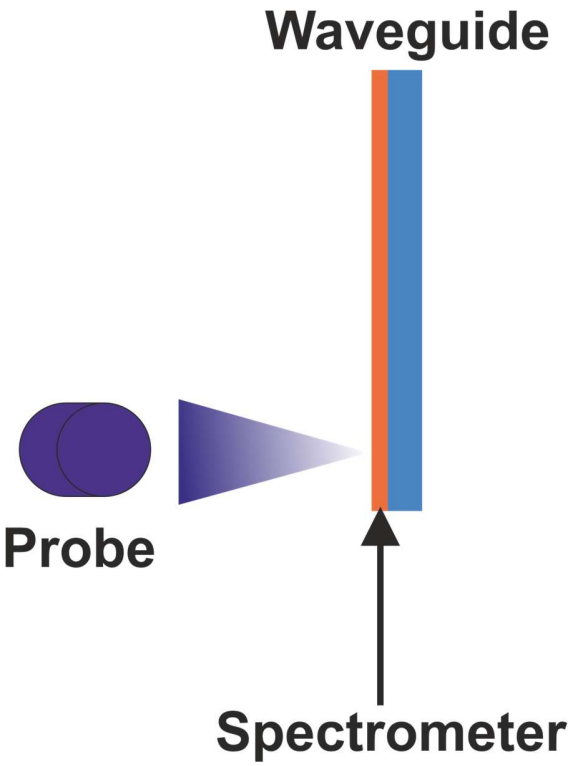

Figure 60- Schematic of spot illumination set up. A converging lens is placed to keep the spot size of the light fixed as 0.5 cm. Using the XYZ stage the probe is moved from the near to the far edge.

Gain measurement

Gain, as known as the concentrating factor, measures the relative amount of light that has been detected at an edge compared to the light detected by a plain photodiode facing the light source. For the gain measurement, a special device as seen in Figure 61 was built by Grahame Faulkner in the Engineering department. This device has four silicone photodiodes connected to detect light at all four edges of a concentrator simultaneously. Photodiode is a semiconductor device which converts the incident light to electric current. Therefore, each photodiode is connected to an oscilloscope which measures the light received in peak to peak voltage. For this experiment, the measurement from a single detector was used.

Gain was calculated by comparing the peak to peak voltage from a concentrator photodiode and a plain photodiode measured at the same distance (15cm) away from the blue light source. Using the equation below the gain for the concentrator was calculated.

$$Gain = \frac{Voltage_{with\ waveguide}}{Voltage_{without\ waveguide}}$$

For an accurate comparison, the difference between the area of the photodiode and cross section of the concentrator edge needs to be taken into account. The dimensions of the photodiode are 1.2mm X 29.1mm and the concentrator cross section of the edge which is 0.1mm (thickness) X 28mm (length). The dimension of the photodiode is approximately 12.5 times greater, therefore, the gain from the concentrator should be multiplied by 12.5.

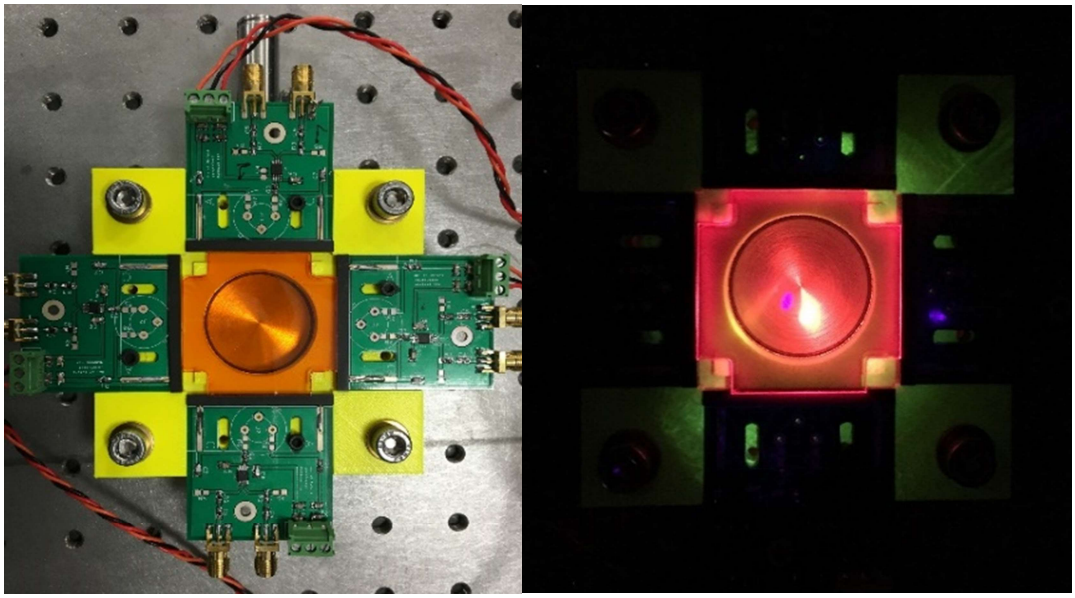

Figure 61- Image showing the device used for gain measurement. The image on the left is under room light, on the right showing concentrator under UV light. 4 photodiodes are attached which can measure the light simultaneously from all 4 edges.

6.3 Results and discussion

To fabricate an efficient concentrator, the three most important factors are the nanocrystals, polymer, and structure of the layers. The nanocrystals need to have a high PLQY, air stability, large Stokes shift, and short PL lifetime (specific to VLC). With respect to the polymer, it must disperse the nanocrystals without aggregation, have chemical stability, and feature robust film formation. Lastly, the structure of the layers requires a low-high-low RI structure in order to achieve TIR. As such, the suitability of possible polymer candidates and their alignment with the nanocrystals were evaluated to select the best polymer. The concentrations of the selected polymer and nanocrystals were modified to observe the effects on the efficiency of the concentrator.

6.3.1 Polymer result

Five different polymers - ethyl cellulose, polystyrene (PS), poly(ethylene)oxide (PEO), polycaprolactone (PCA), and nail polish – were assessed. Five pure polymers (6wt% in toluene) and five polymers (5ml, 6wt% in toluene) mixed with AIS nanocrystals (0.1ml, 3mg/ml) were deposited by two fabrication methods, drop casting and doctor blading, onto a microscope slide. Both transmittance and reflectance were measured to determine the most transparent and smooth film. The surface was further closely examined using MicroXAM. This section is will be sub-divided by data obtained with each of the characterisation techniques.

Transmittance

The transmittance results from the two fabrication methods were identical, showing that the film process method did not affect final film clarity. Figure 62, shows the pure polymer transmittance, where nail polish was exhibited to have the highest

transmittance of ~99%, whereas, PEO had the lowest of ~30%. The second best was ethyl cellulose at ~96%, followed by PCA at ~80%. Therefore, nail polish, ethyl cellulose, and PCA were the top three polymer candidates in terms of transparency. This is an important factor for a concentrator as it suggests less absorption and scattering of incident light by the polymer.

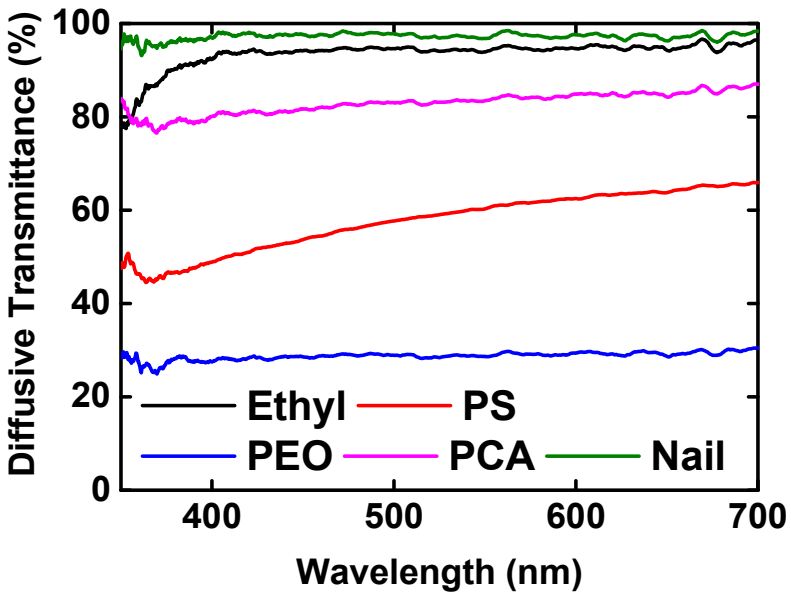

Figure 62- Transmittance of 5 polymers cast from 6wt% toluene solution. The best candidates are Nail polish, Ethyl cellulose, and PCA.

Figure 63 describes the transmittance of the five polymers mixed with AIS nanocrystals. The shapes had changed, reflecting the optical characteristics of the AIS nanocrystals. AIS has a broad absorption from 400-500nm and emits at ~620nm. As compared to the pure polymer measurements, the top two polymers, nail polish and ethyl cellulose, continued to have the highest transmittance. However, the third best position changed from PCA to PS. PCA's 80% transmittance at 600nm for the pure polymer decreased to ~60%,

whereas PS remained constant. This was because of a lack of dispersity of the AIS nanocrystals in the PCA polymer, causing aggregates to form that would have caused the incident light to scatter and reflect outwards, also reducing efficient light guiding. Therefore, when choosing a polymer, the transmittance value on its own is significant, but so, too, are the properties after adding the nanocrystals as they may change.

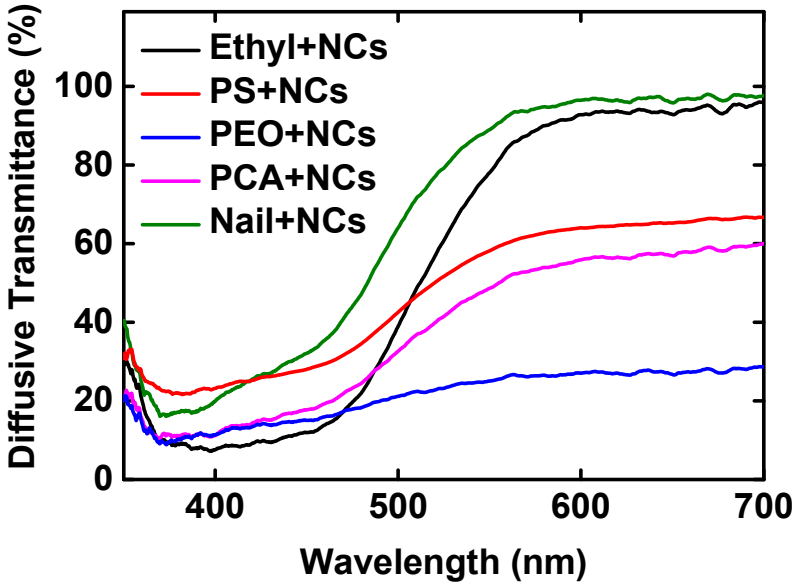

Figure 63- Transmittance of five polymers cast from 3wt% toluene solution mixed with 3mg/ml AIS nanocrystals. The top candidates are nail polish, ethyl cellulose, and PS.

Reflectance

Both diffusive and specular reflectance were measured by the integrating sphere. Background measurement of clean glass is deducted to measure only the light that has been reflected off from the polymer layer. Reflectance is an important parameter for the concentrator film: a lower the value suggests a smoother film. Figure 64, as expected from the transmittance study, shows that PEO, with the lowest transmittance, has the

highest reflectance. The peak at 620nm is a spectrometer artefact. The remaining four polymers' reflectance values are between 0-5%, indicating quite a smooth film formation.

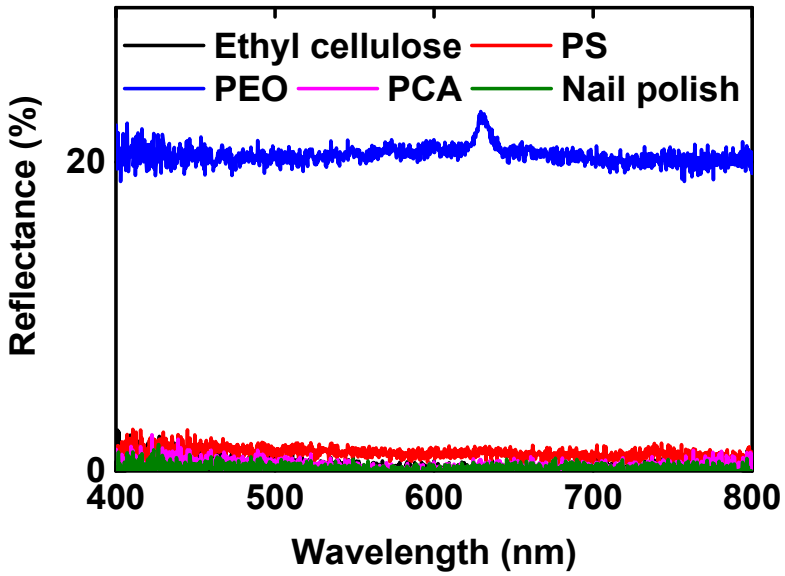

Figure 64- Reflectance of 5 polymers cast from 3wt% toluene solution. Aside from PEO, the remaining polymer shows nearly 0% reflectance value.

The reflectance of a polymer mixed with AIS nanocrystals is measured, as shown in Figure 65. Similarly to transmittance, the peak shape changes due to AIS absorption characteristics. Again, the 4 polymers, aside from PEO, show low reflectance. Therefore, the 4 polymers in terms of smoothness are all suitable and show consistent results throughout the nanocrystal mixture.

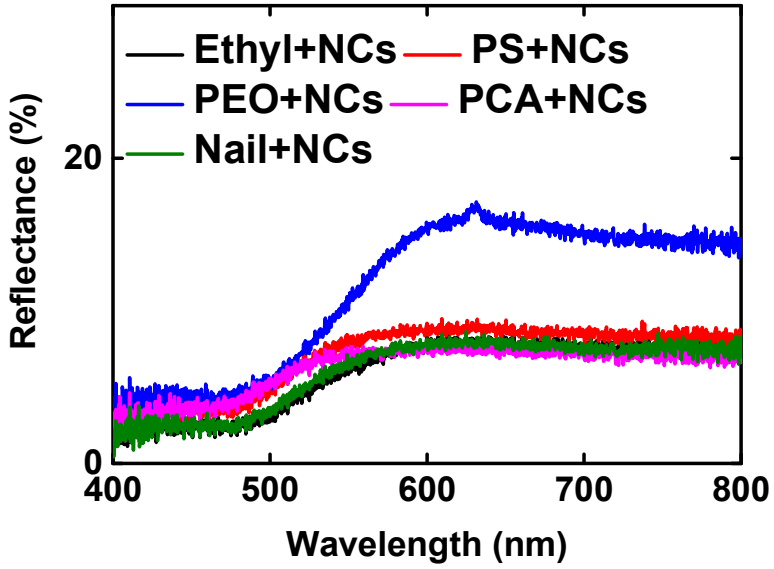

Figure 65- Reflectance of 5 polymers cast from 3wt% toluene solution mixed with AIS nanocrystals 3mg/ml. Apart from PEO, all 4 polymers have low reflectance value.

Surface morphology

A photograph of each of the nanocrystal polymer film samples is shown in Figure 66. Using the Oxford University logo as background, each sample opacity can be compared visually. PEO, in particular, features a patchy and aggregated surface, which explains the poor results from the transmittance and reflectance experiments. The rest of the samples had similar opacities.

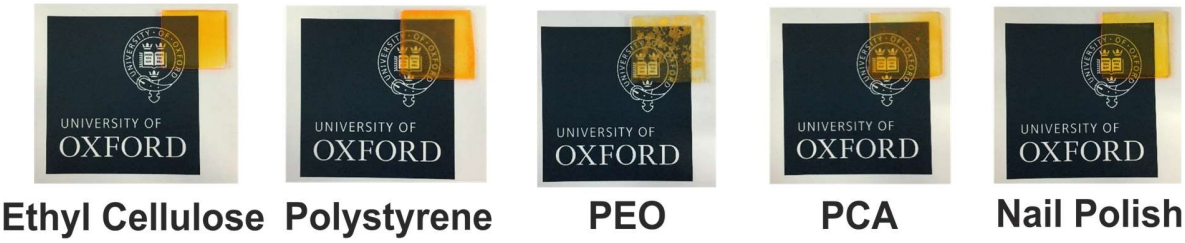

Figure 66- Photograph showing 5 polymer/nanocrystals films placed over the Oxford University logo as background reference. PEO shows a patchy aggregated surface.

MicroXAM was used for an in-depth analysis of the surface of five polymers. Images of the surface taken by MicroXAM are found in Figure 67. The left-hand side of the images are of films formed by drop casting and on the right-hand side by doctor blading. The images are in the order of a) ethyl cellulose, b) PS, c) PEO, d) PCA, and e) nail polish. Compared to the photographs taken in Figure 66, the presence of micro defects that cannot be easily observed by the naked eye are visualised.

The observations are summarised in Table 15. Comparing the two methods, it seems that samples prepared with doctor blading mostly contain contaminates. This can be explained by the preparation environment. The doctor-blading machine is placed in an open space, where dust contamination is inevitable, and the coating time takes a minimum of one min for the blade to pass and the sample to be moved for drying, during which time it is exposed to air. In contrast, drop casting is a quick procedure that can be performed inside a fume hood and samples are covered quickly after the polymer is deposited. Therefore, drop casting has less exposure to dust relative to doctor blading.

The crack-like features in the PS and PCA samples (Figure 67b and Figure 67d, respectively) are owing to crazing. Crazing is a network of lines that are observed internally in the polymer layer, where they are normally not felt at the surface. Crazing, in this case, occurs as strain increases within the polymer during the drying process, and it is a common feature observed in thermoplastics, like PS and PCA [209]. For ethyl cellulose (Figure 67a) the small particle-like features are not based on aggregation, but rather small micro air bubbles trapped within the film according to naked eye observation.

Although degasification was undertaken to remove air bubbles, during the polymer deposition process, new bubbles might have formed.

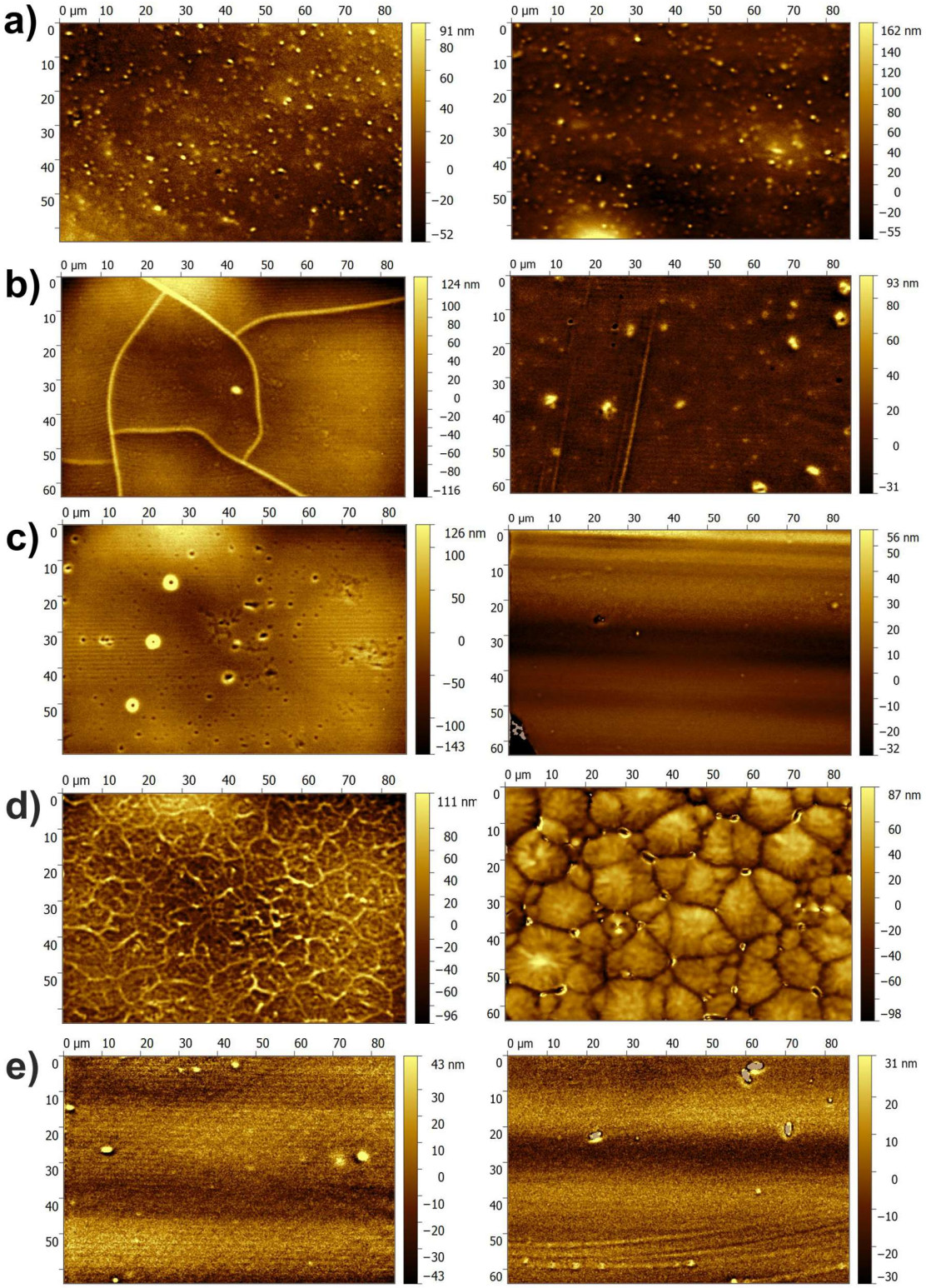

*Figure 67-MicroXAM images taken a) Ethyl cellulose b) PS c) PEO d) PCA e) Nail polish, images of the **left** is **drop casting** and images of the **right** is **doctor blading.***

Table 15- Summary of the observations from Figure 67.

Polymer sample	**Drop casting**	**Doctor blading**
1. Ethyl cellulose	Air bubbles	Air bubbles
2. PS	Large crazing	Contaminants from air, voids
3. PEO	Voids	Contaminants from air
4. PCA	Small crazing	Medium-sized cracks, contaminants from air
5. Nail polish	Contaminants	Contaminants for air

The impact of the features seen in Table 15 on film formability can be quantified by carrying out surface roughness measurements using MicroXAM. Figure 68 shows the surface roughness of the five polymer films produced by both doctor blading and drop casting. Overall, doctor blading has a higher surface roughness than drop casting, while the overall trend remained the same. As explained earlier, doctor blading involves dust contamination, which would explain the higher surface roughness. From the measurements, nail polish had the lowest surface roughness. Despite the air bubble features observed with ethyl cellulose, its surface roughness was the second lowest. PEO, again, had the highest surface roughness. The surface roughness values observed from MicroXAM showed similar trends as reflectance and transmittance.

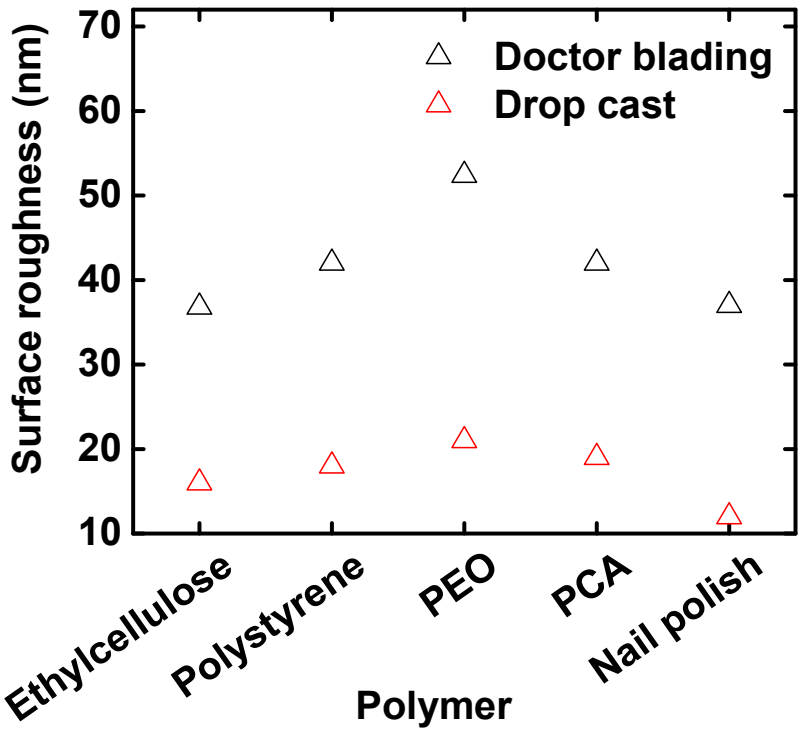

Figure 68- Surface roughness value from MicroXAM analysis of 5 polymers plotted for doctor blading and drop casting. Overall doctor balding has a higher surface roughness. From the measurement, in the order of nail polish, ethyl cellulose, and PS has the lowest surface roughness.

6.3.2 Ethyl cellulose concentration

Based on the aforementioned experiments, nail polish was found to have the best optical properties. However, as it is a commercially-made product that has various unknown chemical additives, there is less control over its physical properties. Therefore, ethyl cellulose was chosen as the candidate for the remaining experiments. The film fabrication method used was drop casting as it had the least surface roughness.

One of the most important properties for a concentrator is the ability to form a thick nanocrystal layer to increase the amount of light emitted on the edges. Thickness can be controlled by density and viscosity of the polymer using different weight percentages. Here, mixtures of nanocrystals in 2, 4, 6, 8, 10wt% ethyl cellulose solutions were

prepared and the optical properties of the resulting films were studied via transmittance and reflectance. The thickness was measured through DEKTAK. It is hypothesised that as the weight percentage of ethyl cellulose increases the transmittance will be reduced and reflectance will increase.

Transmittance

Figure 69 shows the transmittance of films at the five different ethyl cellulose concentrations. It is shown that there is a slight decrease in transmittance with increasing wt%. All transmittance values are high, being above ~90%. After the nanocrystals were added, the graph shape changed (Figure 70). As seen previously in Section 6.4.1, the change in graph's trend was because of the AIS absorption and emission. These effects were better observed with ethyl cellulose as the polymer itself has a high transmittance at all wavelengths. At 400-500nm, based on absorption of AIS, the transmittance dropped to 20%, whereas at peak emission wavelength of ~620nm, the transmittance recovered to 90%.

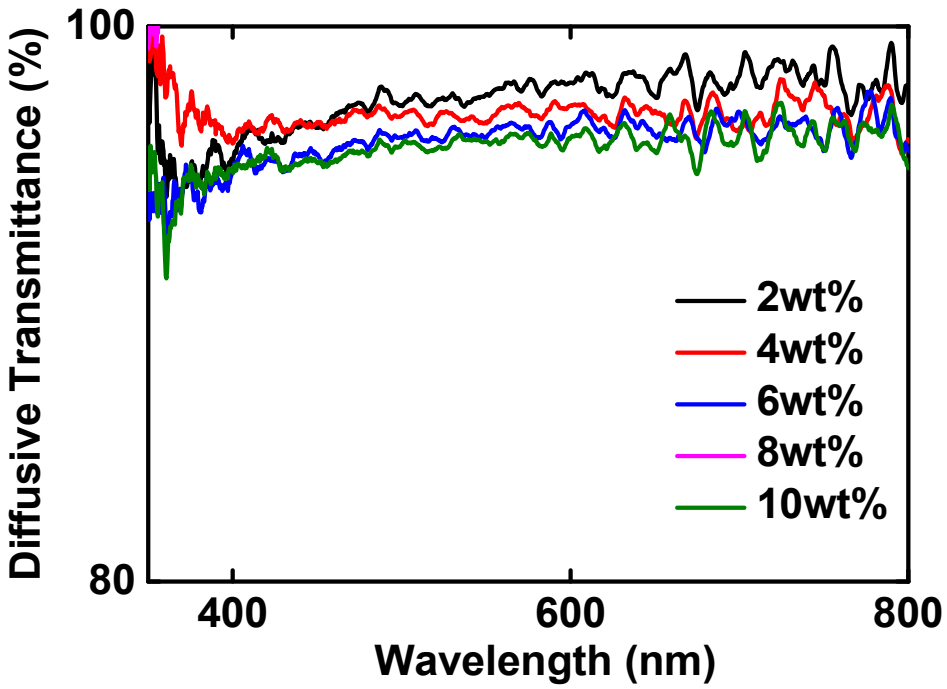

Figure 69- Diffusive transmittance of 5 different wt% of ethyl cellulose, showing small variation in value with the change with wt%.

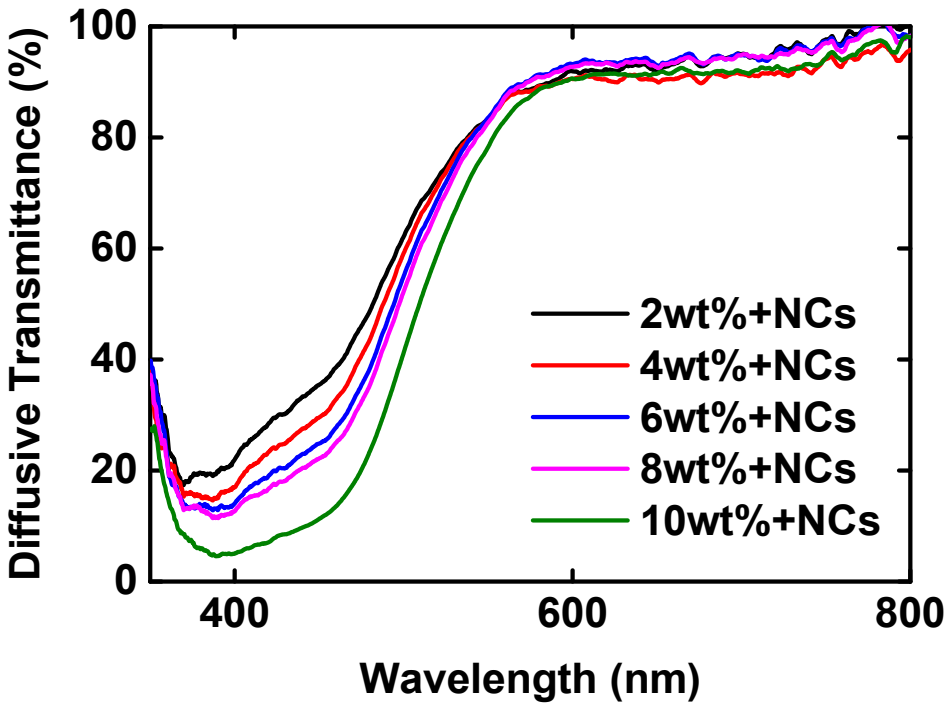

Figure 70- Diffusive transmittance of 5 different wt% of ethyl cellulose + AIS Nanocrystals. The shape of the graph changes due to the absorption characteristics of the nanocrystals.

Reflectance

In Figure 71, the reflectance of the different weight percentages of ethyl cellulose are seen. Overall, the reflectance is small, being below ~5%. As expected, the reflectance increases with raising the amount of ethyl cellulose. This was expected because by adding more polymer, the number of polymer molecules increased per unit, thereby increasing the overall density of the solution [210].

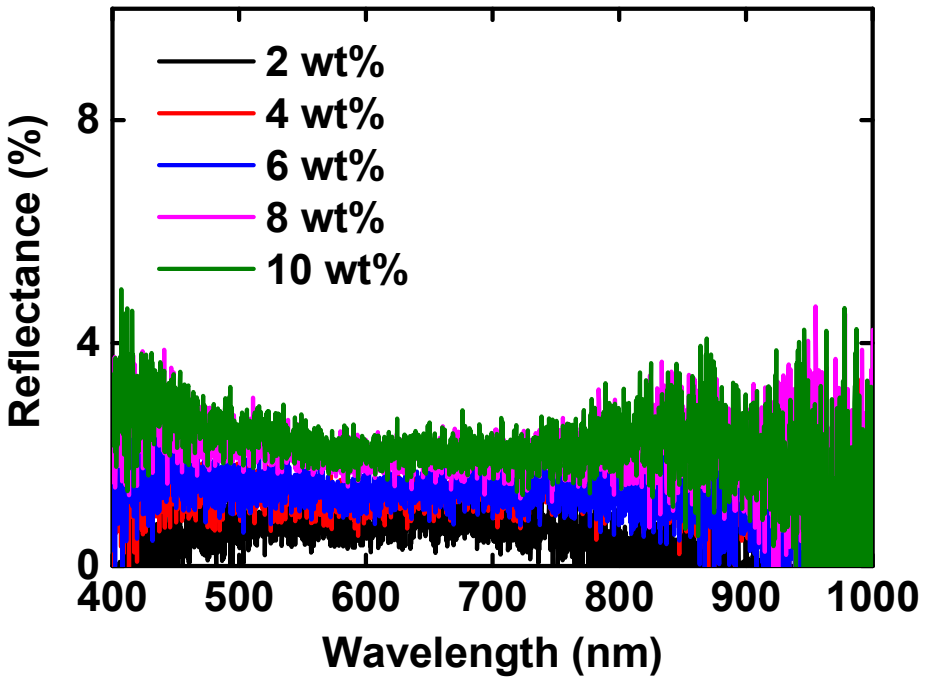

Figure 71- Reflectance of 5 different wt% of ethyl cellulose. All the samples show a low reflectance value of 4% and lower.

When AIS nanocrystals were added, the reflectance shape changed because of the nanocrystals' optical characteristics, as seen in Figure 72. Below ~490nm, where AIS absorption takes place, the reflectance values were further lowered below 4%. At 620nm, which is the peak emission wavelength of AIS, an increase in reflectance is thus observed.

In general, the relative transmittance and reflectance of the nanocrystals with ethyl cellulose was minimal, demonstrating that ethyl cellulose wt% change does not have a huge impact on nanocrystals' optical properties.

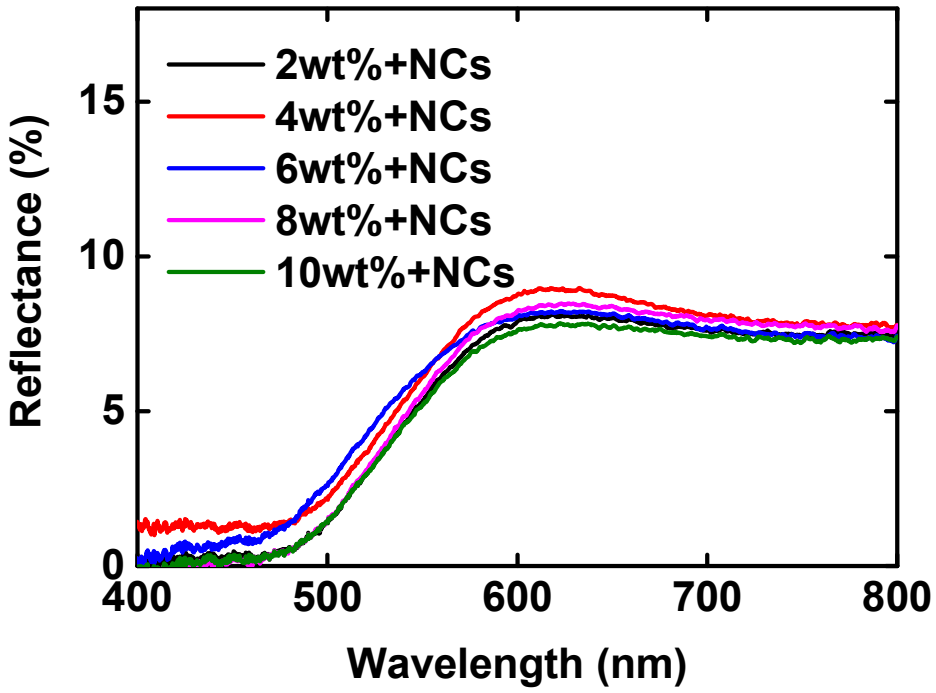

Figure 72- Reflectance of 5 different wt% of ethyl cellulose +AIS Nanocrystals. The graph shape changes according to the AIS optical characteristics.

As observed in Table 16, by increasing the concentration of ethyl cellulose, an increase in film thickness is notable. For the same amount of volume poured, using different wt%, higher amounts of polymer are evident as polymer density increases. Therefore, the final thickness is also increased. Yet, with the increase in wt%, the polymer becomes dense and viscous, making it difficult to disperse the nanocrystals uniformly. Although high thickness is preferred, for better nanocrystal dispersion, 8wt% was selected as the optimum wt% for the rest of the sample preparations.

Table 16- Summary of the thickness measurement of ethyl cellulose using DEKTAK

Ethyl Cellulose (wt %)	**Thickness (um)**
2	54
4	62
6	83
8	116
10	377

6.3.3 Effect of concentration of nanocrystals on flood/full illumination

Three different concentrations of AIS nanocrystals – 1mg/ml, 3mg/ml, and 9mg/ml – 0.1ml were dispersed in the 5ml of 8wt% ethyl cellulose to observe the changes in emission intensity through flood illumination. As the concentration of AIS nanocrystals rose, the PL peak intensity increased because there were more fluorescing particles per given volume (Figure 73). For a concentrator, it was preferable to have as many nanocrystals as possible within the same volume as this would increase the overall gain.

With the concentration increase, the spectra broadened to longer wavelengths, which is different than a red-shift. This phenomenon was attributed to reabsorption, which prominently occurred for optically dense samples. Absorption took place where emission and absorption overlapped. Therefore, this indicates that there is a limit to the concentration of AIS nanocrystals that can be employed before reabsorption affects performance.

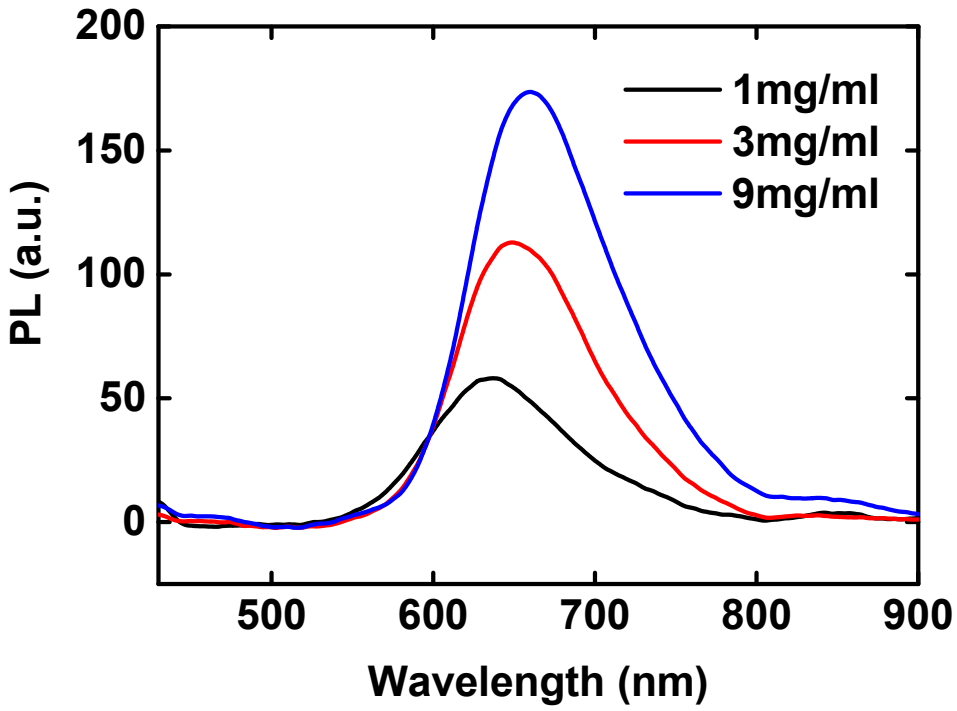

Figure 73- Flood illumination of 3 different concentrations of AIS nanocrystals in 8wt% ethyl cellulose in toluene. PL broadening occurs with increasing AIS concentration, which is an indication of re-absorption.

6.3.4 Effect of concentration of nanocrystals on spot illumination

Figure 74 depicts spot illumination where PL measurement is taken every 4mm, from the near to the far edge. According to the Beer-Lambert law equation:

$$A = -\log\left(\frac{I}{I_0}\right) = \varepsilon C l,$$

where I_0 is incident light, I is light passed through the sample, ε is molar absorptivity of the sample, l is the sample path length, and C is the concentration of the sample.

From the equation, the intensity decreases exponentially with the length of the path that light needs to travel through the medium [11]. The longer the path from excitation to the point of detection, the higher the probability of reabsorption. Therefore, as seen from

Figure 74, at all three concentrations, PL emission decreased exponentially with increasing distance.

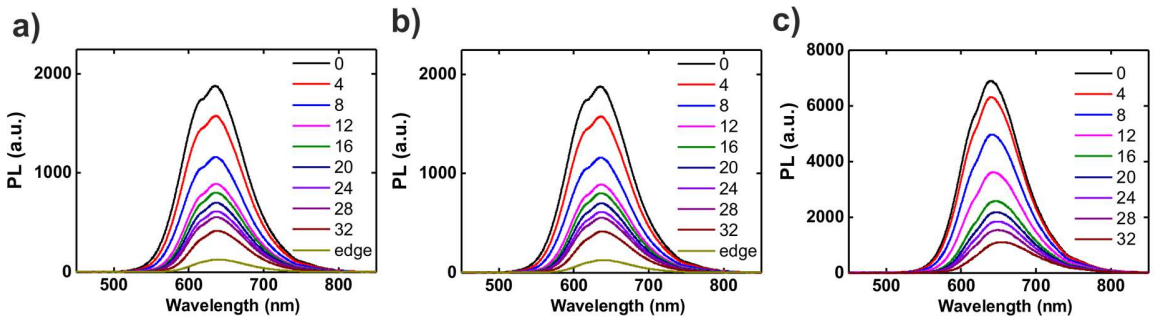

Figure 74- Spot illumination of 3 different concentration of AIS in 8wt% of ethyl cellulose. a) 1mg/ml, b) 3mg/ml, c) 9mg/ml. The PL emission decreases exponentially with increasing spot distance from the detector.

Normally, as seen with $CuInS_2$, a double peak, as shown in Figure 75, is observed with far edge measurements. This is another characteristic feature of reabsorption. Emission at higher wavelengths grows at the expense of the low wavelength emission as reabsorption becomes stronger [211]. This may not have been as clearly observed for these AIS nanocrystals because of the large Stokes shift.

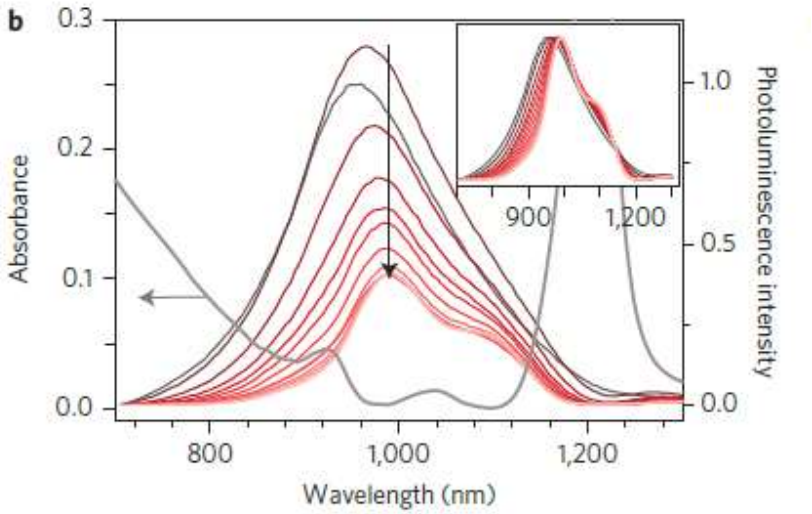

Figure 75- PL emission graphs plotted with excitation distance (0-12cm) distance measurement. Double peaks occur at far edge, a characteristic feature of reabsorption. Image reproduced from reference, Meinardi et al. [211].

The total power of light can be calculated by taking the area under the PL curve. For each of the PL curves with the three different concentrations, the power was calculated and plotted in Figure 76. As seen with the PL peak changes, the total power exponentially decreases with distance. 9mg/ml has the overall highest total power, but has the steepest decrease compared to the other two concentrations.

When choosing the length of the concentrator, the results from Figure 76 should be taken into account. For the 9mg/ml sample, after 12mm distance, the total power decreased to 50% of its initial value. As the length for the device sample for gain measurement was 28mm, the total light at this distance will be reduced in intensity 73% of its initial value.

From these experiments, it was concluded that from the flood and spot illumination, total emission increased by raising the concentration of AIS, but this also increased the reabsorption factor. Therefore, an optimum length of concentrator should be considered.

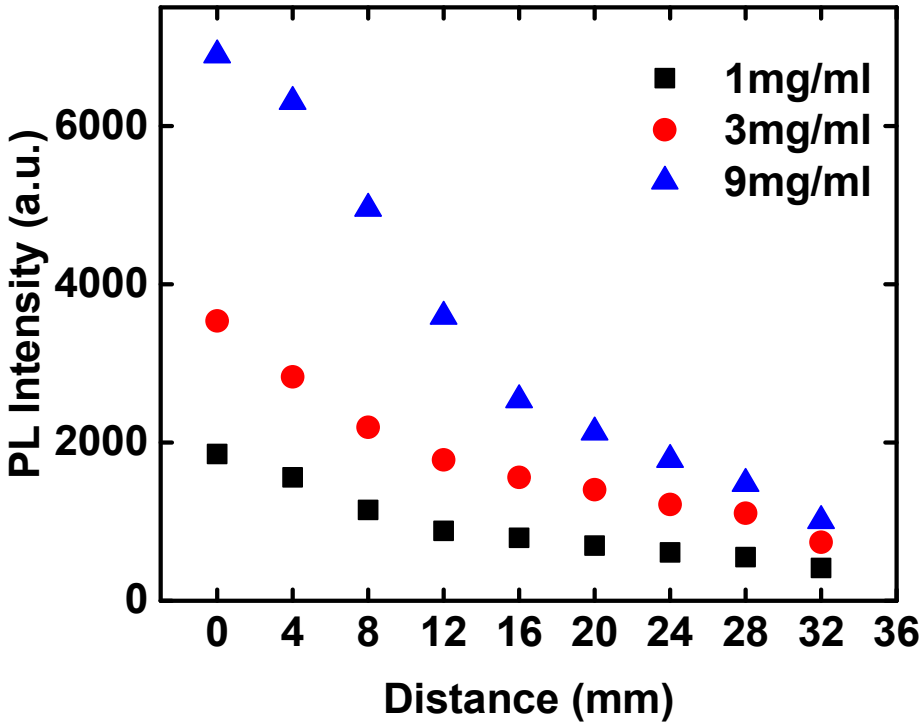

Figure 76- Plot of the total power of light emitted per each distance for 3 different NC concentrations. As expected 9mg/ml with the highest concentration has the highest total power. However, shows a steep exponential decrease in power with distance.

6.3.5 Gain measurement

Combining the findings from the polymer and nanocrystal concentration study, it was found that a combination of ethyl cellulose with 5ml of 8wt% in toluene and 0.1ml of 9mg/ml of AIS nanocrystals was the best choice in terms optical properties suited for light concentration. Using this very combination, three different structures of nanocrystals, nanocrystals + low RI polymer, and nanocrystals + low RI + mirror were produced to measure the gain achieved compared to a single photodiode directly facing the light source. The measurements are plotted in Figure 77, where it was shown that among the three structures, that with the mirror layer had the highest peak. Each peak

was corrected by unit per area, as the cross-sectional area of the photodiode was 12.5-fold greater compared to the concentrator thin film which was on the micrometre scale.

As more layers were added to the basic structure, each addition enhanced the TIR within the polymer plus nanocrystal layer. A lower RI with the polymer addition helped match the RI difference so that higher TIR could occur. The mirror assisted with reflecting the light that would have been normally transmitted through the nanocrystal layer back upwards for a second chance for absorption.

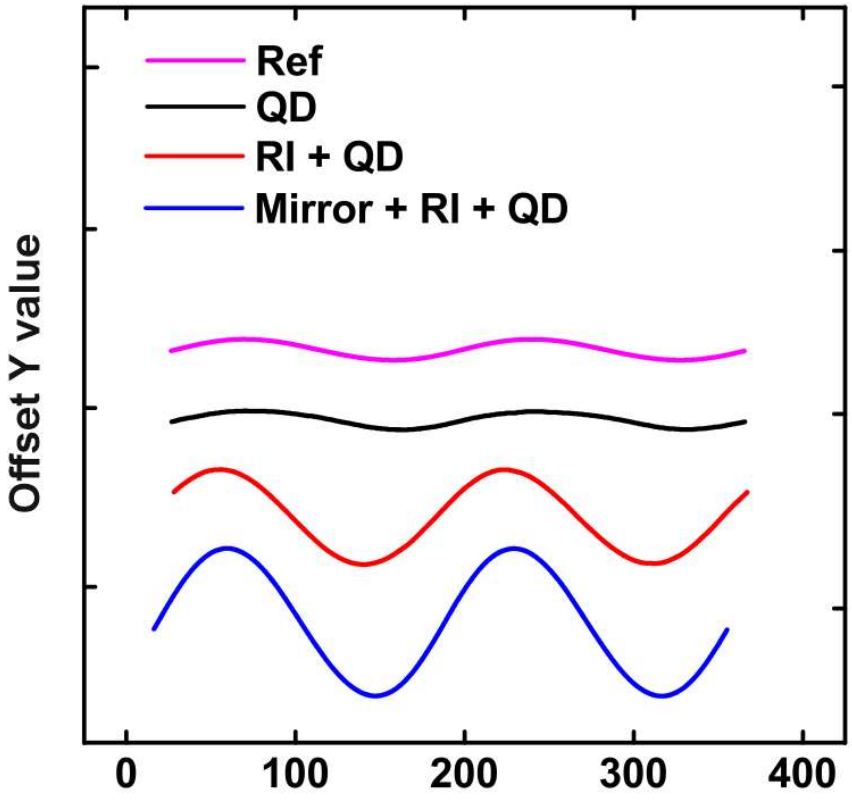

Figure 77- The sine waves of 3 different structures and the reference (the photodiode) collected from the oscilloscope. Each peak are corrected by unit per area. Peak is enhanced with new layer added.

Utilising the peak-to-peak values of the curves, the gain was calculated using the equation in Section 6.2.3. Table 17 summarises the results. With the mirror structure, it was calculated that the gain was 7 compared to a single photodiode. For communication

applications, if a photodiode on its own was used, the results showed that less light would be detected. Photodiode size cannot be increased as a solution to increase light gained as it needs to be kept small to foster a large bandwidth. Hence, using a large area concentrator helps the photodiode maximise the amount to light gained while keeping the photodiode the thinnest thickness (1.2mm) possible.

Table 17 - Relative gain of 3 different structures compared from reference (the photodiode)

	Nanocrystals	**RI + Nanocrystals**	**Mirror + RI + Nanocrystals**
Relative Gain	1	4.7	7

6.4 Conclusion

AIS nanocrystals are potential materials for replacing organic dyes or other Cd/Pb-based luminescent nanocrystals for concentrator applications (LSC or VLC) based on their large Stokes shift and high PLQY. In this chapter, AIS nanocrystals were used to optimise a LC through modifying polymer types, nanocrystal concentrations, and device structure.

Five different polymers, namely ethyl cellulose, PS, PEO, PCA, and nail polish were studied to determine suitability for concentrator applications. Transmittance and reflectance were assessed to understand surface roughness and clarity. MicroXAM and DEKTAK were used to observe the surface and measure roughness and thickness. From this, it was shown that ethyl cellulose had the smoothest, most transparent, and well-dispersed nanocrystal films.

Three concentrations of AIS nanocrystals in ethyl cellulose were compared and it was found through flood illumination experiments that higher concentrations of nanocrystals increased the overall PL detected at the edge, while spot illumination indicated that higher nanocrystal concentrations had stronger reabsorption.

Using ethyl cellulose mixed with nanocrystals, the optical properties of different structural combinations were evaluated to understand the PL emissions and reabsorption effects. It was observed that the nanocrystal + low RI + mirror combination had the highest gain, being 7, compared to a plain reference photodiode.

The polymer and concentrator fabrication methods established here can be used for other types of nanocrystals. With further improvements in the structure and AIS

nanocrystal properties, there is great promise for VLC as a next-generation communication technology.

Chapter 7 -Conclusion and future work

7.1 Conclusion

The aim of the thesis was to understand and establish a synthesis method for CIS and AIS, in order to achieve a high PLQY, and apply suitable nanocrystals to develop a light concentrator device.

The synthesis method was based on the hot-injection procedure, and among the inorganic nanocrystals $CuInS_2$ were chosen based on its lower toxicity (when compared with cadmium or lead nanocrystals), high photo stability and absorption co-efficiency. Through modification of $CuInS_2$ synthesis parameters, PLQY was improved from the initial value of ~6% to ~60%. The established synthesis method of CIS was then applied to synthesise AIS nanocrystals. AIS synthesis was further developed in order to reduce the by-products through changes in the reduction temperature. This resulted in achieving a high PLQY of 89%. Finally, AIS nanocrystals were applied to fabricate a first ever inorganic LC.

Over the course of the study, the following conclusions were determined:

1. The new synthesis method, low injection synthesis, was applied by using TMSS, a highly reactive sulfur precursor. This method has a short preparation time (~2.5 hours excluding cleaning time), high reproducibility and low cost due to use of low temperature (the injection temperature was brought down to less than 90°C), thereby demonstrating it's potential to be used for mass production. The synthesis procedure was improved by investigating 4 different injection temperatures and precursor concentrations to determine the best result. A low injection temperature (30°C) allowed formation of

monodispersed nanocrystals, while a high-injection temperature (90°C) gave rise to nanocrystals with greater indium content. Changes in the precursor ratio were reflected in the final nanocrystal composition, as demonstrated through STEM-EDX measurement. The result showed that more In-rich nanocrystals lead to a higher PLQY. Through these efforts, PLQY was increased to ~ 50% by using a 30°C injection temperature with 1:4 ratio of Cu:In.

2. Further improvement of the synthesis was made by using halide precursors, which led to the highest PLQY, ~60%, with the combination of copper bromide and indium chloride. 16 combinations of fluoride, chloride, bromide, and iodide were investigated to find the best combination that controls the reactivity of the precursors and produces the highest halide passivation effect. The precursor reactivity was predicted and calculated by using the figure of merit equation that was formulated based on the combination of Lewis HSAB theory, solubility conditions and bond dissociation values. The figure of merit equation was shown to have a high correlation with the experimental results.

3. The synthesis parameters established from $CuInS_2$ synthesis has shown to be also effective for AIS synthesis. Through analysis of STEM-EDX and UV-VIS, by-products of Ag and AgS nanocrystals were observed. Using *in-situ* PL, formation of silver nanocrystals were observed because of the high reduction temperature (180°C). By lowering the reduction temperature, this controlled the reactivity of silver precursor, which decreased Ag and AgS by-products. As a result, the highest PLQY to date, 89%, of AIS nanocrystals was achieved.

4. The first inorganic LC was fabricated using AIS. This was the first attempt at an inorganic LC; thus, the host polymer for the nanocrystals and the concentrator parameters (thickness, device layer, and etc.) were established from scratch. After testing 5 different polymers, ethyl cellulose was chosen due to its low reflectance, high transmittance and high AIS solubility. Different concentrations of nanocrystals and ethyl cellulose were characterised, and it was found that an 8wt% ethyl cellulose solution and 9mg/ml nanocrystals resulted in an optimal balance, achieving low reabsorption and high thickness. Using different device structures, glass – mirror (Al coating) – low-refractive polymer – nanocrystal polymer composite, achieved the highest gain of 7 relative to a plain reference photodiode.

Overall, the work presented here adds a significant contribution to the synthesis of CIS and AIS nanocrystals. Many studies that improve CIS PLQY relies mostly on adding a shell structure or changing the composition. In this thesis, a new approach is developed to use a variety of halide precursor combinations to control the reactivity of the precursors and enhance PLQY. Additionally, a new synthesis method, low injection of TMSS (sulphur precursor), was developed. By using an *in-situ* PL technique, it has been shown that the synthesis method was effective in terms of the addition of indium content. Therefore, the final composition of the nanocrystal reflects the initial precursor quantities that have been used.

With the improvements made on the nanocrystal synthesis method, AIS nanocrystals with a high PLQY of 89% with a clear excitonic peak was achieved. The concentrator built using the AIS nanocrystal has been shown to have a higher (more than 7) gain over light

absorbed by a photodiode alone. This achievement is a first significant step towards using an inorganic nanocrystal for VLC concentrator.

The long PL lifetime, which is a limiting factor of using AIS for communication applications, needs to be addressed. Possible solutions include the use of post-treatment techniques or shell over-coating to reduce the unwanted defects that add to the PL lifetime. Furthermore, to replace the cadmium-based nanocrystal, with PLQY of near unity, improvement in the PLQY of ternary nanocrystals is required. To achieve a PLQY near unity, the recombination mechanisms need to be further investigated to enhance DAP recombination while reducing the unwanted non-radiative recombination.

Nevertheless, AIS has valuable properties, such as photo-stability and large Stokes shifts, which are vital for concentrator material characteristics and provide a starting point for synthesising highly luminescing AIS that is applicable to various concentrator applications.

7.2 Future work

I. Further improvements in the PLQY of $AgInS_2$ nanocrystals could be achieved by applying a core-shell structure and post treatments, such as etching or applying halide ligands, to reduce surface defects. Current AIS, NC's PLQY arises just from the core nanocrystals, but by reducing non-radiative recombination, an enhancement in PL can be made.

II. By-product formation can be reduced by separating the silver and indium precursor-reduction temperature. It has been seen that silver can easily reduce at low temperatures to form silver nanocrystals. A dual flask set-up can be used to separate the reaction temperatures and the two precursors could be mixed just before the injection of sulfur precursor.

III. Device structures can be improved by modifying the fabrication process.
   a. Fabrication in a clean room or in a glove box to prevent dust contaminants and compare film forming results.
   b. The current deposition method of using a pipette needs to be modified to prevent air bubbles forming. Alternatively, the solution could be dried in a vacuum environment to release trapped air during deposition.
   c. A thicker nanocrystal layer could be made to increase the PL emission through stacking layers on top of each other or using molds to peel and stick the nanocrystal film.

IV. Use 4 detectors to measure emission from all the 4 edges to enhance detection of light, which will increase the overall gain. Compare the gain with

4 separate photodiodes as a reference and calculate the difference in signal to noise ratio.

Chapter 8 -Reference

1. Altavilla, C.; Ciliberto, E., *Inorganic Nanoparticles: Synthesis, Applications, and Perspectives*. CRC Press: 2016.
2. and, A. L. E.; Rosen, M., The Electronic Structure of Semiconductor Nanocrystals. *Annual Review of Materials Science* **2000,** *30* (1), 475-521.
3. Vayssieres, L., Growth of Arrayed Nanorods and Nanowires of ZnO from Aqueous Solutions. *Advanced Materials* **2003,** *15* (5), 464-466.
4. Lee, S. M.; Cho, S. N.; Cheon, J., Anisotropic Shape Control of Colloidal Inorganic Nanocrystals. *Advanced Materials* **2003,** *15* (5), 441-444.
5. Dabbousi, B. O.; Rodriguez-Viejo, J.; Mikulec, F. V.; Heine, J. R.; Mattoussi, H.; Ober, R.; Jensen, K. F.; Bawendi, M. G., (CdSe)ZnS Core−Shell Quantum Dots: Synthesis and Characterization of a Size Series of Highly Luminescent Nanocrystallites. *The Journal of Physical Chemistry B* **1997,** *101* (46), 9463-9475.
6. Kolny-Olesiak, J.; Weller, H., Synthesis and Application of Colloidal CuInS2 Semiconductor Nanocrystals. *ACS Applied Materials & Interfaces* **2013,** *5* (23), 12221-12237.
7. Zhong, H.; Zhou, Y.; Ye, M.; He, Y.; Ye, J.; He, C.; Yang, C.; Li, Y., Controlled Synthesis and Optical Properties of Colloidal Ternary Chalcogenide CuInS2 Nanocrystals. *Chemistry of Materials* **2008,** *20* (20), 6434-6443.
8. CIsco Visual Networking Index: Global Mobile Data Traffic Forecast Update, 2016-2021 White Paper. **2017**.
9. Zhou, Y.; Benetti, D.; Fan, Z.; Zhao, H.; Ma, D.; Govorov, A. O.; Vomiero, A.; Rosei, F., Near Infrared, Highly Efficient Luminescent Solar Concentrators. *Advanced Energy Materials* **2016**, n/a-n/a.
10. Li, C.; Chen, W.; Wu, D.; Quan, D.; Zhou, Z.; Hao, J.; Qin, J.; Li, Y.; He, Z.; Wang, K., Large Stokes Shift and High Efficiency Luminescent Solar Concentrator Incorporated with CuInS2/ZnS Quantum Dots. *Scientific Reports* **2015,** *5*, 17777.
11. Krumer, Z.; Pera, S. J.; van Dijk-Moes, R. J. A.; Zhao, Y.; de Brouwer, A. F. P.; Groeneveld, E.; van Sark, W. G. J. H. M.; Schropp, R. E. I.; de Mello Donegá, C., Tackling self-absorption in luminescent solar concentrators with type-II colloidal quantum dots. *Solar Energy Materials and Solar Cells* **2013,** *111*, 57-65.
12. Aldakov, D.; Lefrancois, A.; Reiss, P., Ternary and quaternary metal chalcogenide nanocrystals: synthesis, properties and applications. *Journal of Materials Chemistry C* **2013,** *1* (24), 3756-3776.
13. Collins, S.; Mulyawan, R.; Rajbhandari, S.; Chu, H.; Faulkner, G. E.; Brien, D. C. O.; Manousiadis, P. P.; Vithanage, D. A.; Turnbull, G. A.; Samuel, I. D. W. In *A simple wide field of view concentrator for free space visible light communications*, Summer Topicals Meeting Series (SUM), 2015, 13-15 July 2015; 2015; pp 43-44.
14. Månsson, N.; Bergbäck, B.; Sörme, L., Phasing Out Cadmium, Lead, and Mercury. *Journal of Industrial Ecology* **2009,** *13* (1), 94-111.
15. Leach, A. D. P.; Macdonald, J. E., Optoelectronic Properties of CuInS2 Nanocrystals and Their Origin. *The Journal of Physical Chemistry Letters* **2016,** *7* (3), 572-583.
16. Jia, Y.; Wang, H.; Yan, Z.; Deng, L.; Dong, H.; Ma, N.; Sun, D., A facile method for the synthesis of CuInS2-ZnS quantum dots with tunable photoluminescent properties. *RSC Advances* **2016,** *6* (96), 93303-93308.
17. Ekimov, A.; Onushchenko, A., Quantum size effect in three-dimensional microscopic semiconductor crystals.
18. Ekimov, A.; Onushchenko, A., Quantum size effect in the optical-spectra of semiconductor micro-crystals. *Soviet Physics Semiconductors-Ussr* **1982,** *16* (7), 775-778.

19. Brus, L. E., Electron–electron and electron-hole interactions in small semiconductor crystallites: The size dependence of the lowest excited electronic state. *The Journal of Chemical Physics* **1984,** *80* (9), 4403-4409.
20. Brus, L., Electronic wave functions in semiconductor clusters: experiment and theory. *The Journal of Physical Chemistry* **1986,** *90* (12), 2555-2560.
21. Murray, C. B.; Norris, D. J.; Bawendi, M. G., Synthesis and characterization of nearly monodisperse CdE (E = sulfur, selenium, tellurium) semiconductor nanocrystallites. *Journal of the American Chemical Society* **1993,** *115* (19), 8706-8715.
22. Hines, M. A.; Guyot-Sionnest, P., Synthesis and Characterization of Strongly Luminescing ZnS-Capped CdSe Nanocrystals. *The Journal of Physical Chemistry* **1996,** *100* (2), 468-471.
23. Malik, M. A.; O'Brien, P.; Revaprasadu, N., A Simple Route to the Synthesis of Core/Shell Nanoparticles of Chalcogenides. *Chemistry of Materials* **2002,** *14* (5), 2004-2010.
24. Peng, X.; Schlamp, M. C.; Kadavanich, A. V.; Alivisatos, A. P., Epitaxial Growth of Highly Luminescent CdSe/CdS Core/Shell Nanocrystals with Photostability and Electronic Accessibility. *Journal of the American Chemical Society* **1997,** *119* (30), 7019-7029.
25. He, Y.; Lu, H.-T.; Sai, L.-M.; Su, Y.-Y.; Hu, M.; Fan, C.-H.; Huang, W.; Wang, L.-H., Microwave Synthesis of Water-Dispersed CdTe/CdS/ZnS Core-Shell-Shell Quantum Dots with Excellent Photostability and Biocompatibility. *Advanced Materials* **2008,** *20* (18), 3416-3421.
26. Drbohlavova, J.; Adam, V.; Kizek, R.; Hubalek, J., Quantum Dots — Characterization, Preparation and Usage in Biological Systems. *International Journal of Molecular Sciences* **2009,** *10* (2), 656-673.
27. Guo, W.; Li, J. J.; Wang, Y. A.; Peng, X., Conjugation Chemistry and Bioapplications of Semiconductor Box Nanocrystals Prepared via Dendrimer Bridging. *Chemistry of Materials* **2003,** *15* (16), 3125-3133.
28. Jaiswal, J. K.; Mattoussi, H.; Mauro, J. M.; Simon, S. M., Long-term multiple color imaging of live cells using quantum dot bioconjugates. *Nat Biotech* **2003,** *21* (1), 47-51.
29. Liu, W.; He, Z.; Liang, J.; Zhu, Y.; Xu, H.; Yang, X., Preparation and characterization of novel fluorescent nanocomposite particles: CdSe/ZnS core-shell quantum dots loaded solid lipid nanoparticles. *Journal of Biomedical Materials Research Part A* **2008,** *84A* (4), 1018-1025.
30. Zhang, B.; Cheng, J.; Li, D.; Liu, X.; Ma, G.; Chang, J., A novel method to make hydrophilic quantum dots and its application on biodetection. *Materials Science and Engineering: B* **2008,** *149* (1), 87-92.
31. Gerion, D.; Pinaud, F.; Williams, S. C.; Parak, W. J.; Zanchet, D.; Weiss, S.; Alivisatos, A. P., Synthesis and Properties of Biocompatible Water-Soluble Silica-Coated CdSe/ZnS Semiconductor Quantum Dots. *The Journal of Physical Chemistry B* **2001,** *105* (37), 8861-8871.
32. Dubertret, B.; Skourides, P.; Norris, D. J.; Noireaux, V.; Brivanlou, A. H.; Libchaber, A., In Vivo Imaging of Quantum Dots Encapsulated in Phospholipid Micelles. *Science* **2002,** *298* (5599), 1759-1762.
33. Zeng, Q.; Kong, X.; Sun, Y.; Zhang, Y.; Tu, L.; Zhao, J.; Zhang, H., Synthesis and Optical Properties of Type II CdTe/CdS Core/Shell Quantum Dots in Aqueous Solution via Successive Ion Layer Adsorption and Reaction. *The Journal of Physical Chemistry C* **2008,** *112* (23), 8587-8593.
34. Gallagher, S. A.; Comby, S.; Wojdyla, M.; Gunnlaugsson, T.; Kelly, J. M.; Gun'ko, Y. K.; Clark, I. P.; Greetham, G. M.; Towrie, M.; Quinn, S. J., Efficient Quenching of TGA-Capped CdTe Quantum Dot Emission by a Surface-Coordinated Europium(III) Cyclen Complex. *Inorganic Chemistry* **2013,** *52* (8), 4133-4135.
35. Kumar, P.; Kumar, P.; Bharadwaj, L. M.; Paul, A. K.; Sharma, S. C.; Kush, P.; Deep, A., Aqueous Synthesis of l-Cysteine Stabilized Water-Dispersible CdS:Mn Quantum Dots for Biosensing Applications. *BioNanoScience* **2013,** *3* (2), 95-101.

36. Chen, O.; Zhao, J.; Chauhan, V. P.; Cui, J.; Wong, C.; Harris, D. K.; Wei, H.; Han, H.-S.; Fukumura, D.; Jain, R. K.; Bawendi, M. G., Compact high-quality CdSe–CdS core–shell nanocrystals with narrow emission linewidths and suppressed blinking. *Nat Mater* **2013,** *12* (5), 445-451.
37. Qin, H.; Niu, Y.; Meng, R.; Lin, X.; Lai, R.; Fang, W.; Peng, X., Single-Dot Spectroscopy of Zinc-Blende CdSe/CdS Core/Shell Nanocrystals: Nonblinking and Correlation with Ensemble Measurements. *Journal of the American Chemical Society* **2014,** *136* (1), 179-187.
38. Dai, X.; Zhang, Z.; Jin, Y.; Niu, Y.; Cao, H.; Liang, X.; Chen, L.; Wang, J.; Peng, X., Solution-processed, high-performance light-emitting diodes based on quantum dots. *Nature* **2014,** *515* (7525), 96-99.
39. Ding, T. X.; Olshansky, J. H.; Leone, S. R.; Alivisatos, A. P., Efficiency of Hole Transfer from Photoexcited Quantum Dots to Covalently Linked Molecular Species. *Journal of the American Chemical Society* **2015,** *137* (5), 2021-2029.
40. Wang, L.; Nagesha, D. K.; Selvarasah, S.; Dokmeci, M. R.; Carrier, R. L., Toxicity of CdSe Nanoparticles in Caco-2 Cell Cultures. *Journal of Nanobiotechnology* **2008,** *6*, 11-11.
41. Zhong, H.; Bai, Z.; Zou, B., Tuning the Luminescence Properties of Colloidal I–III–VI Semiconductor Nanocrystals for Optoelectronics and Biotechnology Applications. *The Journal of Physical Chemistry Letters* **2012,** *3* (21), 3167-3175.
42. Chen, B.; Zhong, H.; Zhang, W.; Tan, Z. a.; Li, Y.; Yu, C.; Zhai, T.; Bando, Y.; Yang, S.; Zou, B., Highly Emissive and Color-Tunable CuInS2-Based Colloidal Semiconductor Nanocrystals: Off-Stoichiometry Effects and Improved Electroluminescence Performance. *Advanced Functional Materials* **2012,** *22* (10), 2081-2088.
43. Shabaev, A.; Mehl, M. J.; Efros, A. L., Energy band structure of $CuInS_2$ and optical spectra of $CuInS_2$ nanocrystals. *Physical Review B* **2015,** *92* (3), 035431.
44. Pan, D.; An, L.; Sun, Z.; Hou, W.; Yang, Y.; Yang, Z.; Lu, Y., Synthesis of Cu–In–S Ternary Nanocrystals with Tunable Structure and Composition. *Journal of the American Chemical Society* **2008,** *130* (17), 5620-5621.
45. Vahidshad, Y.; Tahir, M. N.; Mirkazemi, S. M.; Iraji Zad, A.; Ghasemzadeh, R.; Tremel, W., One-pot thermolysis synthesis of CuInS2 nanoparticles with chalcopyrite-wurtzite polytypism structure. *Journal of Materials Science: Materials in Electronics* **2015,** *26* (11), 8960-8972.
46. Xie, B.-B.; Hu, B.-B.; Jiang, L.-F.; Li, G.; Du, Z.-L., The phase transformation of CuInS(2) from chalcopyrite to wurtzite. *Nanoscale Res Lett* **2015,** *10*, 86.
47. Batabyal, S. K.; Tian, L.; Venkatram, N.; Ji, W.; Vittal, J. J., Phase-Selective Synthesis of CuInS2 Nanocrystals. *The Journal of Physical Chemistry C* **2009,** *113* (33), 15037-15042.
48. Hong, S. P.; Park, H. K.; Oh, J. H.; Yang, H.; Do, Y. R., Comparisons of the structural and optical properties of o-AgInS2, t-AgInS2, and c-AgIn5S8 nanocrystals and their solid-solution nanocrystals with ZnS. *Journal of Materials Chemistry* **2012,** *22* (36), 18939-18949.
49. Tian, L.; Elim, H. I.; Ji, W.; Vittal, J. J., One-pot synthesis and third-order nonlinear optical properties of AgInS2 nanocrystals. *Chemical Communications* **2006,** (41), 4276-4278.
50. Feng, Z.; Dai, P.; Ma, X.; Zhan, J.; Lin, Z., Monodispersed cation-disordered cubic AgInS2 nanocrystals with enhanced fluorescence. *Applied Physics Letters* **2010,** *96* (1), 013104.
51. Shi, Y.; Jin, Z.; Li, C.; An, H.; Qiu, J., Effect of [Cu]/[In] ratio on properties of CuInS2 thin films prepared by successive ionic layer absorption and reaction method. *Applied Surface Science* **2006,** *252* (10), 3737-3743.
52. Tapley, A.; Liu, L.; Cui, X.; Zuin, L.; Love, D. A.; Zhou, J.; Sham, T.-K.; Ding, Z., Assessing the Band Structure of CuInS2 Nanocrystals and Their Bonding with the Capping Ligand. *The Journal of Physical Chemistry C* **2015,** *119* (36), 20967-20974.
53. Jaffe, J. E.; Zunger, A., Electronic structure of the ternary chalcopyrite semiconductors. *Physical Review B* **1983,** *28* (10), 5822-5847.
54. Tsuji, I.; Kato, H.; Kobayashi, H.; Kudo, A., Photocatalytic H2 Evolution Reaction from Aqueous Solutions over Band Structure-Controlled (AgIn)xZn2(1-x)S2 Solid Solution

Photocatalysts with Visible-Light Response and Their Surface Nanostructures. *Journal of the American Chemical Society* **2004,** *126* (41), 13406-13413.
55. Deng, D.; Chen, Y.; Cao, J.; Tian, J.; Qian, Z.; Achilefu, S.; Gu, Y., High-Quality CuInS2/ZnS Quantum Dots for In vitro and In vivo Bioimaging. *Chemistry of Materials* **2012,** *24* (15), 3029-3037.
56. Li, L.; Pandey, A.; Werder, D. J.; Khanal, B. P.; Pietryga, J. M.; Klimov, V. I., Efficient Synthesis of Highly Luminescent Copper Indium Sulfide-Based Core/Shell Nanocrystals with Surprisingly Long-Lived Emission. *Journal of the American Chemical Society* **2011,** *133* (5), 1176-1179.
57. Binsma, J. J. M.; Giling, L. J.; Bloem, J., Luminescence of CuInS2. *Journal of Luminescence* **1982,** *27* (1), 55-72.
58. Castro, S. L.; Bailey, S. G.; Raffaelle, R. P.; Banger, K. K.; Hepp, A. F., Synthesis and Characterization of Colloidal CuInS2 Nanoparticles from a Molecular Single-Source Precursor. *The Journal of Physical Chemistry B* **2004,** *108* (33), 12429-12435.
59. Nam, D.-E.; Song, W.-S.; Yang, H., Noninjection, one-pot synthesis of Cu-deficient CuInS2/ZnS core/shell quantum dots and their fluorescent properties. *Journal of Colloid and Interface Science* **2011,** *361* (2), 491-496.
60. Wang, X.; Liang, Z.; Xu, X.; Wang, N.; Fang, J.; Wang, J.; Xu, G., A high efficient photoluminescence Zn–Cu–In–S/ZnS quantum dots with long lifetime. *Journal of Alloys and Compounds* **2015,** *640*, 134-140.
61. Hamanaka, Y.; Ogawa, T.; Tsuzuki, M.; Kuzuya, T., Photoluminescence Properties and Its Origin of AgInS2 Quantum Dots with Chalcopyrite Structure. *The Journal of Physical Chemistry C* **2011,** *115* (5), 1786-1792.
62. Omata, T.; Nose, K.; Kurimoto, K.; Kita, M., Electronic transition responsible for size-dependent photoluminescence of colloidal CuInS2 quantum dots. *Journal of Materials Chemistry C* **2014,** *2* (33), 6867-6872.
63. Kraatz, I. T.; Booth, M.; Whitaker, B. J.; Nix, M. G. D.; Critchley, K., Sub-Bandgap Emission and Intraband Defect-Related Excited-State Dynamics in Colloidal CuInS2/ZnS Quantum Dots Revealed by Femtosecond Pump–Dump–Probe Spectroscopy. *The Journal of Physical Chemistry C* **2014,** *118* (41), 24102-24109.
64. Sun, J.; Zhu, D.; Zhao, J.; Ikezawa, M.; Wang, X.; Masumoto, Y., Ultrafast carrier dynamics in CuInS2 quantum dots. *Applied Physics Letters* **2014,** *104* (2), 023118.
65. Chen, H.; Wang, C.-Y.; Wang, J.-T.; Wu, Y.; Zhou, S.-X., First-principles study of point defects in solar cell semiconductor CuI. *Physica B: Condensed Matter* **2013,** *413*, 116-119.
66. Rice, W. D.; McDaniel, H.; Klimov, V. I.; Crooker, S. A., Magneto-Optical Properties of CuInS2 Nanocrystals. *The Journal of Physical Chemistry Letters* **2014,** *5* (23), 4105-4109.
67. Krustok, J.; Raudoja, J.; Krunks, M.; Mändar, H.; Collan, H., Nature of the native deep localized defect recombination centers in the chalcopyrite and orthorhombic AgInS2. *Journal of Applied Physics* **2000,** *88* (1), 205-209.
68. Ogawa, T.; Kuzuya, T.; Hamanaka, Y.; Sumiyama, K., Synthesis of Ag-In binary sulfide nanoparticles-structural tuning and their photoluminescence properties. *Journal of Materials Chemistry* **2010,** *20* (11), 2226-2231.
69. Mao, B.; Chuang, C.-H.; Wang, J.; Burda, C., Synthesis and Photophysical Properties of Ternary I–III–VI AgInS2 Nanocrystals: Intrinsic versus Surface States. *The Journal of Physical Chemistry C* **2011,** *115* (18), 8945-8954.
70. Berends, A. C.; Rabouw, F. T.; Spoor, F. C. M.; Bladt, E.; Grozema, F. C.; Houtepen, A. J.; Siebbeles, L. D. A.; de Mello Donegá, C., Radiative and Nonradiative Recombination in CuInS2 Nanocrystals and CuInS2-Based Core/Shell Nanocrystals. *The Journal of Physical Chemistry Letters* **2016,** *7* (17), 3503-3509.

71. Chevallier, T.; Benayad, A.; Le Blevennec, G.; Chandezon, F., Method to determine radiative and non-radiative defects applied to AgInS2-ZnS luminescent nanocrystals. *Physical Chemistry Chemical Physics* **2017,** *19* (3), 2359-2363.
72. Mao, B.; Chuang, C.-H.; Lu, F.; Sang, L.; Zhu, J.; Burda, C., Study of the Partial Ag-to-Zn Cation Exchange in AgInS2/ZnS Nanocrystals. *The Journal of Physical Chemistry C* **2013,** *117* (1), 648-656.
73. Rao, M. J.; Shibata, T.; Chattopadhyay, S.; Nag, A., Origin of Photoluminescence and XAFS Study of (ZnS)1–x(AgInS2)x Nanocrystals. *The Journal of Physical Chemistry Letters* **2014,** *5* (1), 167-173.
74. Kadlag, K. P.; Patil, P.; Jagadeeswara Rao, M.; Datta, S.; Nag, A., Luminescence and solar cell from ligand-free colloidal AgInS2 nanocrystals. *CrystEngComm* **2014,** *16* (17), 3605-3612.
75. Hamanaka, Y.; Ogawa, T.; Tsuzuki, M.; Ozawa, K.; Kuzuya, T., Luminescence properties of chalcopyrite AgInS2 nanocrystals: Their origin and related electronic states. *Journal of Luminescence* **2013,** *133*, 121-124.
76. van der Stam, W.; Berends, A. C.; de Mello Donega, C., Prospects of Colloidal Copper Chalcogenide Nanocrystals. *ChemPhysChem* **2016,** *17* (5), 559-581.
77. Jara, D. H.; Stamplecoskie, K. G.; Kamat, P. V., Two Distinct Transitions in CuxInS2 Quantum Dots. Bandgap versus Sub-Bandgap Excitations in Copper-Deficient Structures. *The Journal of Physical Chemistry Letters* **2016,** *7* (8), 1452-1459.
78. Kim, Y.-K.; Ahn, S.-H.; Chung, K.; Cho, Y.-S.; Choi, C.-J., The photoluminescence of CuInS2 nanocrystals: effect of non-stoichiometry and surface modification. *Journal of Materials Chemistry* **2012,** *22* (4), 1516-1520.
79. Seo, J.; Raut, S.; Abdel-Fattah, M.; Rice, Q.; Tabibi, B.; Rich, R.; Fudala, R.; Gryczynski, I.; Gryczynski, Z.; Kim, W.-J.; Jung, S.; Hyun, R., Time-resolved and temperature-dependent photoluminescence of ternary and quaternary nanocrystals of CuInS2 with ZnS capping and cation exchange. *Journal of Applied Physics* **2013,** *114* (9), 094310.
80. Liu, X. H.; Dou, X. M.; Sugiyama, M., Photoluminescence studies in CuInS2 thin films grown by sulfurization using ditertiarybutylsulfide. *Journal of Applied Physics* **2012,** *112* (12), 123521.
81. Shi, A.; Wang, X.; Meng, X.; Liu, X.; Li, H.; Zhao, J., Temperature-dependent photoluminescence of CuInS2 quantum dots. *Journal of Luminescence* **2012,** *132* (7), 1819-1823.
82. Mer, V. K. L., Nucleation in Phase Transitions. *Industrial & Engineering Chemistry* **1952,** *44* (6), 1270-1277.
83. Thanh, N. T. K.; Maclean, N.; Mahiddine, S., Mechanisms of Nucleation and Growth of Nanoparticles in Solution. *Chemical Reviews* **2014,** *114* (15), 7610-7630.
84. Kumar, S.; Nann, T., Shape Control of II–VI Semiconductor Nanomaterials. *Small* **2006,** *2* (3), 316-329.
85. Peng, X.; Wickham, J.; Alivisatos, A. P., Kinetics of II-VI and III-V Colloidal Semiconductor Nanocrystal Growth: "Focusing" of Size Distributions. *Journal of the American Chemical Society* **1998,** *120* (21), 5343-5344.
86. Reiss, H., The Growth of Uniform Colloidal Dispersions. *The Journal of Chemical Physics* **1951,** *19* (4{Reiss, 1951 #195}), 482-487.
87. Talapin, D. V.; Rogach, A. L.; Haase, M.; Weller, H., Evolution of an Ensemble of Nanoparticles in a Colloidal Solution: Theoretical Study. *The Journal of Physical Chemistry B* **2001,** *105* (49), 12278-12285.
88. Shannon, R., Revised effective ionic radii and systematic studies of interatomic distances in halides and chalcogenides. *Acta Crystallographica Section A* **1976,** *32* (5), 751-767.
89. Yu, W. W.; Peng, X., Formation of High-Quality CdS and Other II–VI Semiconductor Nanocrystals in Noncoordinating Solvents: Tunable Reactivity of Monomers. *Angewandte Chemie International Edition* **2002,** *41* (13), 2368-2371.

90. Xie, R.; Rutherford, M.; Peng, X., Formation of High-Quality I–III–VI Semiconductor Nanocrystals by Tuning Relative Reactivity of Cationic Precursors. *Journal of the American Chemical Society* **2009,** *131* (15), 5691-5697.
91. Xie, R.; Battaglia, D.; Peng, X., Colloidal InP Nanocrystals as Efficient Emitters Covering Blue to Near-Infrared. *Journal of the American Chemical Society* **2007,** *129* (50), 15432-15433.
92. Dierick, R.; Van den Broeck, F.; De Nolf, K.; Zhao, Q.; Vantomme, A.; Martins, J. C.; Hens, Z., Surface Chemistry of CuInS2 Colloidal Nanocrystals, Tight Binding of L-Type Ligands. *Chemistry of Materials* **2014,** *26* (20), 5950-5957.
93. Moreels, I.; Justo, Y.; De Geyter, B.; Haustraete, K.; Martins, J. C.; Hens, Z., Size-Tunable, Bright, and Stable PbS Quantum Dots: A Surface Chemistry Study. *ACS Nano* **2011,** *5* (3), 2004-2012.
94. Fritzinger, B.; Capek, R. K.; Lambert, K.; Martins, J. C.; Hens, Z., Utilizing Self-Exchange To Address the Binding of Carboxylic Acid Ligands to CdSe Quantum Dots. *Journal of the American Chemical Society* **2010,** *132* (29), 10195-10201.
95. Amgoune, A.; Bourissou, D., [sigma]-Acceptor, Z-type ligands for transition metals. *Chemical Communications* **2011,** *47* (3), 859-871.
96. Carey, G. H.; Abdelhady, A. L.; Ning, Z.; Thon, S. M.; Bakr, O. M.; Sargent, E. H., Colloidal Quantum Dot Solar Cells. *Chemical Reviews* **2015,** *115* (23), 12732-12763.
97. Allen, P. M.; Bawendi, M. G., Ternary I–III–VI Quantum Dots Luminescent in the Red to Near-Infrared. *Journal of the American Chemical Society* **2008,** *130* (29), 9240-9241.
98. Cassette, E.; Pons, T.; Bouet, C.; Helle, M.; Bezdetnaya, L.; Marchal, F.; Dubertret, B., Synthesis and Characterization of Near-Infrared Cu–In–Se/ZnS Core/Shell Quantum Dots for In vivo Imaging. *Chemistry of Materials* **2010,** *22* (22), 6117-6124.
99. Zhang, J.; Xie, R.; Yang, W., A Simple Route for Highly Luminescent Quaternary Cu-Zn-In-S Nanocrystal Emitters. *Chemistry of Materials* **2011,** *23* (14), 3357-3361.
100. Peng, S.; Zhang, S.; Mhaisalkar, S. G.; Ramakrishna, S., Synthesis of AgInS2 nanocrystal ink and its photoelectrical application. *Physical Chemistry Chemical Physics* **2012,** *14* (24), 8523-8529.
101. Dai, M.; Ogawa, S.; Kameyama, T.; Okazaki, K.-i.; Kudo, A.; Kuwabata, S.; Tsuboi, Y.; Torimoto, T., Tunable photoluminescence from the visible to near-infrared wavelength region of non-stoichiometric AgInS2 nanoparticles. *Journal of Materials Chemistry* **2012,** *22* (25), 12851-12858.
102. Omata, T.; Nose, K.; Otsuka-Yao-Matsuo, S., Size dependent optical band gap of ternary I-III-VI2 semiconductor nanocrystals. *Journal of Applied Physics* **2009,** *105* (7), 073106.
103. Pan, Z.; Mora-Seró, I.; Shen, Q.; Zhang, H.; Li, Y.; Zhao, K.; Wang, J.; Zhong, X.; Bisquert, J., High-Efficiency "Green" Quantum Dot Solar Cells. *Journal of the American Chemical Society* **2014,** *136* (25), 9203-9210.
104. De Trizio, L.; Prato, M.; Genovese, A.; Casu, A.; Povia, M.; Simonutti, R.; Alcocer, M. J. P.; D'Andrea, C.; Tassone, F.; Manna, L., Strongly Fluorescent Quaternary Cu–In–Zn–S Nanocrystals Prepared from Cu1-xInS2 Nanocrystals by Partial Cation Exchange. *Chemistry of Materials* **2012,** *24* (12), 2400-2406.
105. Reiss, P.; Protière, M.; Li, L., Core/Shell Semiconductor Nanocrystals. *Small* **2009,** *5* (2), 154-168.
106. Xia, Y.; Zhu, C., Aqueous synthesis of type-II core/shell CdTe/CdSe quantum dots for near-infrared fluorescent sensing of copper(ii). *Analyst* **2008,** *133* (7), 928-932.
107. Reiss, P.; Bleuse, J.; Pron, A., Highly Luminescent CdSe/ZnSe Core/Shell Nanocrystals of Low Size Dispersion. *Nano Letters* **2002,** *2* (7), 781-784.
108. Park, J.; Kim, S.-W., CuInS2/ZnS core/shell quantum dots by cation exchange and their blue-shifted photoluminescence. *Journal of Materials Chemistry* **2011,** *21* (11), 3745-3750.

109. Choi, H. S.; Kim, Y.; Park, J. C.; Oh, M. H.; Jeon, D. Y.; Nam, Y. S., Highly luminescent, off-stoichiometric CuxInyS2/ZnS quantum dots for near-infrared fluorescence bio-imaging. *RSC Advances* **2015,** *5* (54), 43449-43455.
110. Nakamura, H.; Kato, W.; Uehara, M.; Nose, K.; Omata, T.; Otsuka-Yao-Matsuo, S.; Miyazaki, M.; Maeda, H., Tunable Photoluminescence Wavelength of Chalcopyrite CuInS2-Based Semiconductor Nanocrystals Synthesized in a Colloidal System. *Chemistry of Materials* **2006,** *18* (14), 3330-3335.
111. Torimoto, T.; Ogawa, S.; Adachi, T.; Kameyama, T.; Okazaki, K.-i.; Shibayama, T.; Kudo, A.; Kuwabata, S., Remarkable photoluminescence enhancement of ZnS-AgInS2 solid solution nanoparticles by post-synthesis treatment. *Chemical Communications* **2010,** *46* (12), 2082-2084.
112. Bae, W. K.; Joo, J.; Padilha, L. A.; Won, J.; Lee, D. C.; Lin, Q.; Koh, W.-k.; Luo, H.; Klimov, V. I.; Pietryga, J. M., Highly Effective Surface Passivation of PbSe Quantum Dots through Reaction with Molecular Chlorine. *Journal of the American Chemical Society* **2012,** *134* (49), 20160-20168.
113. Cademartiri, L.; Ozin, G. A., Emerging strategies for the synthesis of highly monodisperse colloidal nanostructures. *Philosophical Transactions of the Royal Society of London A: Mathematical, Physical and Engineering Sciences* **2010,** *368* (1927), 4229-4248.
114. Zhang, J.; Gao, J.; Miller, E. M.; Luther, J. M.; Beard, M. C., Diffusion-Controlled Synthesis of PbS and PbSe Quantum Dots with in Situ Halide Passivation for Quantum Dot Solar Cells. *ACS Nano* **2014,** *8* (1), 614-622.
115. Tang, J.; Kemp, K. W.; Hoogland, S.; Jeong, K. S.; Liu, H.; Levina, L.; Furukawa, M.; Wang, X.; Debnath, R.; Cha, D.; Chou, K. W.; Fischer, A.; Amassian, A.; Asbury, J. B.; Sargent, E. H., Colloidal-quantum-dot photovoltaics using atomic-ligand passivation. *Nat Mater* **2011,** *10* (10), 765-771.
116. Ning, Z.; Ren, Y.; Hoogland, S.; Voznyy, O.; Levina, L.; Stadler, P.; Lan, X.; Zhitomirsky, D.; Sargent, E. H., All-Inorganic Colloidal Quantum Dot Photovoltaics Employing Solution-Phase Halide Passivation. *Advanced Materials* **2012,** *24* (47), 6295-6299.
117. Zanella, M.; Maserati, L.; Pernia Leal, M.; Prato, M.; Lavieville, R.; Povia, M.; Krahne, R.; Manna, L., Atomic Ligand Passivation of Colloidal Nanocrystal Films via their Reaction with Propyltrichlorosilane. *Chemistry of Materials* **2013,** *25* (8), 1423-1429.
118. Tang, X.; Ho, W. B. A.; Xue, J. M., Synthesis of Zn-Doped AgInS2 Nanocrystals and Their Fluorescence Properties. *The Journal of Physical Chemistry C* **2012,** *116* (17), 9769-9773.
119. Draguta, S.; McDaniel, H.; Klimov, V. I., Tuning Carrier Mobilities and Polarity of Charge Transport in Films of CuInSexS2−x Quantum Dots. *Advanced Materials* **2015,** *27* (10), 1701-1705.
120. Yao, R.-Y.; Zhou, Z.-J.; Hou, Z.-L.; Wang, X.; Zhou, W.-H.; Wu, S.-X., Surfactant-Free CuInS2 Nanocrystals: An Alternative Counter-Electrode Material for Dye-Sensitized Solar Cells. *ACS Applied Materials & Interfaces* **2013,** *5* (8), 3143-3148.
121. Han, J.; Liu, Z.; Guo, K.; Ya, J.; Zhao, Y.; Zhang, X.; Hong, T.; Liu, J., High-Efficiency AgInS2-Modified ZnO Nanotube Array Photoelectrodes for All-Solid-State Hybrid Solar Cells. *ACS Applied Materials & Interfaces* **2014,** *6* (19), 17119-17125.
122. Jagadeeswararao, M.; Swarnkar, A.; Markad, G. B.; Nag, A., Defect-Mediated Electron–Hole Separation in Colloidal Ag2S–AgInS2 Hetero Dimer Nanocrystals Tailoring Luminescence and Solar Cell Properties. *The Journal of Physical Chemistry C* **2016,** *120* (34), 19461-19469.
123. Demir, H. V.; Nizamoglu, S.; Erdem, T.; Mutlugun, E.; Gaponik, N.; Eychmüller, A., Quantum dot integrated LEDs using photonic and excitonic color conversion. *Nano Today* **2011,** *6* (6), 632-647.
124. Shirasaki, Y.; Supran, G. J.; Bawendi, M. G.; Bulovic, V., Emergence of colloidal quantum-dot light-emitting technologies. *Nat Photon* **2013,** *7* (1), 13-23.
125. Song, W.-S.; Yang, H., Fabrication of white light-emitting diodes based on solvothermally synthesized copper indium sulfide quantum dots as color converters. *Applied Physics Letters* **2012,** *100* (18), 183104.

126. Omata, T.; Tani, Y.; Kobayashi, S.; Otsuka-Yao-Matsuo, S., Quantum dot phosphors and their application to inorganic electroluminescence device. *Thin Solid Films* **2012,** *520* (10), 3829-3834.
127. Tan, Z.; Zhang, Y.; Xie, C.; Su, H.; Liu, J.; Zhang, C.; Dellas, N.; Mohney, S. E.; Wang, Y.; Wang, J.; Xu, J., Near-Band-Edge Electroluminescence from Heavy-Metal-Free Colloidal Quantum Dots. *Advanced Materials* **2011,** *23* (31), 3553-3558.
128. Zhang, Y.; Xie, C.; Su, H.; Liu, J.; Pickering, S.; Wang, Y.; Yu, W. W.; Wang, J.; Wang, Y.; Hahm, J.-i.; Dellas, N.; Mohney, S. E.; Xu, J., Employing Heavy Metal-Free Colloidal Quantum Dots in Solution-Processed White Light-Emitting Diodes. *Nano Letters* **2011,** *11* (2), 329-332.
129. Song, W.-S.; Yang, H., Efficient White-Light-Emitting Diodes Fabricated from Highly Fluorescent Copper Indium Sulfide Core/Shell Quantum Dots. *Chemistry of Materials* **2012,** *24* (10), 1961-1967.
130. Li, J.; Zhu, J.-J., Quantum dots for fluorescent biosensing and bio-imaging applications. *Analyst* **2013,** *138* (9), 2506-2515.
131. Wegner, K. D.; Hildebrandt, N., Quantum dots: bright and versatile in vitro and in vivo fluorescence imaging biosensors. *Chemical Society Reviews* **2015,** *44* (14), 4792-4834.
132. Ma, G., Background-Free In vivo Time Domain Optical Molecular Imaging Using Colloidal Quantum Dots. *ACS Applied Materials & Interfaces* **2013,** *5* (8), 2835-2844.
133. Li, L.; Daou, T. J.; Texier, I.; Kim Chi, T. T.; Liem, N. Q.; Reiss, P., Highly Luminescent CuInS2/ZnS Core/Shell Nanocrystals: Cadmium-Free Quantum Dots for In Vivo Imaging. *Chemistry of Materials* **2009,** *21* (12), 2422-2429.
134. Bensebaa, F.; Durand, C.; Aouadou, A.; Scoles, L.; Du, X.; Wang, D.; Page, Y., A new green synthesis method of CuInS2 and CuInSe2 nanoparticles and their integration into thin films. *J Nanopart Res* **2009,** *12* (5), 1897-1903.
135. Pons, T.; Pic, E.; Lequeux, N.; Cassette, E.; Bezdetnaya, L.; Guillemin, F.; Marchal, F.; Dubertret, B., Cadmium-Free CuInS2/ZnS Quantum Dots for Sentinel Lymph Node Imaging with Reduced Toxicity. *ACS Nano* **2010,** *4* (5), 2531-2538.
136. Shamirian, A.; Appelbe, O.; Zhang, Q.; Ganesh, B.; Kron, S. J.; Snee, P. T., A toolkit for bioimaging using near-infrared AgInS2/ZnS quantum dots. *Journal of Materials Chemistry B* **2015,** *3* (41), 8188-8196.
137. Susumu, K.; Mei, B. C.; Mattoussi, H., Multifunctional ligands based on dihydrolipoic acid and polyethylene glycol to promote biocompatibility of quantum dots. *Nat. Protocols* **2009,** *4* (3), 424-436.
138. Ma, N.; Yang, J.; Stewart, K. M.; Kelley, S. O., DNA-Passivated CdS Nanocrystals: Luminescence, Bioimaging, and Toxicity Profiles. *Langmuir* **2007,** *23* (26), 12783-12787.
139. Atcha, K.; Ken-Tye, Y.; Rui, H.; Indrajit, R.; Hong, D.; Lisa, A. V.; Earl, J. B.; Paras, N. P., Biocompatible PEGylated gold nanorods as colored contrast agents for targeted in vivo cancer applications. *Nanotechnology* **2010,** *21* (31), 315101.
140. Park, J.; Dvoracek, C.; Lee, K. H.; Galloway, J. F.; Bhang, H.-e. C.; Pomper, M. G.; Searson, P. C., CuInSe/ZnS Core/Shell NIR Quantum Dots for Biomedical Imaging. *Small* **2011,** *7* (22), 3148-3152.
141. Goetzberger, A.; Greube, W., Solar energy conversion with fluorescent collectors. *Applied physics 14* (2), 123-139.
142. Benner, J.; Owens-Illinois, D. P. F., Luminescent Solar Concentrator. *MASTER* **1979**, 353.
143. Corrado, C.; Leow, S. W.; Osborn, M.; Chan, E.; Balaban, B.; Carter, S. A., Optimization of gain and energy conversion efficiency using front-facing photovoltaic cell luminescent solar concentratordesign. *Solar Energy Materials and Solar Cells* **2013,** *111*, 74-81.
144. Strümpel, C.; McCann, M.; Beaucarne, G.; Arkhipov, V.; Slaoui, A.; Švrček, V.; del Cañizo, C.; Tobias, I., Modifying the solar spectrum to enhance silicon solar cell efficiency—An overview of available materials. *Solar Energy Materials and Solar Cells* **2007,** *91* (4), 238-249.

145. Slooff, L. H.; Bende, E. E.; Burgers, A. R.; Budel, T.; Pravettoni, M.; Kenny, R. P.; Dunlop, E. D.; Büchtemann, A., A luminescent solar concentrator with 7.1% power conversion efficiency. *physica status solidi (RRL) – Rapid Research Letters* **2008,** *2* (6), 257-259.
146. Cheng, L.; Baojun, L., Multiple dyes containing luminescent solar concentrators with enhanced absorption and efficiency. *Journal of Optics* **2015,** *17* (2), 025901.
147. Meinardi, F.; Colombo, A.; Velizhanin, K. A.; Simonutti, R.; Lorenzon, M.; Beverina, L.; Viswanatha, R.; Klimov, V. I.; Brovelli, S., Large-area luminescent solar concentrators based on /`Stokes-shift-engineered/' nanocrystals in a mass-polymerized PMMA matrix. *Nat Photon* **2014,** *8* (5), 392-399.
148. Wilton, S. R.; Fetterman, M. R.; Low, J. J.; You, G.; Jiang, Z.; Xu, J., Monte Carlo study of PbSe quantum dots as the fluorescent material in luminescent solar concentrators. *Opt. Express* **2014,** *22* (S1), A35-A43.
149. Tummeltshammer, C.; Portnoi, M.; Mitchell, S. A.; Lee, A.-T.; Kenyon, A. J.; Tabor, A. B.; Papakonstantinou, I., On the ability of Förster resonance energy transfer to enhance luminescent solar concentrator efficiency. *Nano Energy* **2017,** *32*, 263-270.
150. Bose, R.; Gonzalez, M.; Jenkins, P.; Walters, R.; Morseman, J.; Moss, M.; McLain, C.; Linsert, P.; Büchtemann, A.; Chatten, A. J.; Barnham, K. W. J. In *Resonance energy transfer in luminescent solar concentrators*, 2010 35th IEEE Photovoltaic Specialists Conference, 20-25 June 2010; 2010; pp 000467-000470.
151. Komine, T.; Nakagawa, M., Fundamental analysis for visible-light communication system using LED lights. *IEEE Transactions on Consumer Electronics* **2004,** *50* (1), 100-107.
152. Tanaka, Y.; Komine, T.; Haruyama, S.; Nakagawa, M., Indoor Visible Light Data Transmission System Utilizing White LED Lights(Optical Wireless Communications). *IEICE transactions on communications* **2003,** *86* (8), 2440-2454.
153. http://www.eurocontrol.int/articles/spectrum-management-military.
154. Rahaim, M. B.; Vegni, A. M.; Little, T. D. C. In *A hybrid Radio Frequency and broadcast Visible Light Communication system*, GLOBECOM Workshops (GC Wkshps), 2011 IEEE, 5-9 Dec. 2011; 2011; pp 792-796.
155. Rajbhandari, S.; Chun, H.; Faulkner, G.; Cameron, K.; Jalajakumari, A. V. N.; Henderson, R.; Tsonev, D.; Ijaz, M.; Chen, Z.; Haas, H.; Xie, E.; McKendry, J. J. D.; Herrnsdorf, J.; Gu, E.; Dawson, M. D.; Brien, D. O., High-Speed Integrated Visible Light Communication System: Device Constraints and Design Considerations. *IEEE Journal on Selected Areas in Communications* **2015,** *33* (9), 1750-1757.
156. Collins, S.; O'Brien, D. C.; Watt, A., High gain, wide field of view concentrator for optical communications. *Opt. Lett.* **2014,** *39* (7), 1756-1759.
157. Strutt, J. W.; Strutt, J. W., *On the Scattering of Light by small Particles*

Scientific Papers. Cambridge University Press: 2009.
158. He, G. S.; Law, W.-C.; Liu, L.; Zhang, X.; Prasad, P. N., Stimulated Mie scattering in nanocrystals suspension. *Applied Physics Letters* **2012,** *101* (1), 011110.
159. He, T.; Wang, Y.; Tian, X.; Gao, Y.; Zhao, X.; Grimsdale, A. C.; Lin, X.; Sun, H., An organic dye with very large Stokes-shift and broad tunability of fluorescence: Potential two-photon probe for bioimaging and ultra-sensitive solid-state gas sensor. *Applied Physics Letters* **2016,** *108* (1), 011901.
160. Drexhage, K., Fluorescence efficiency of laser dyes. **1977**.
161. Schubert, E. F., *Light-Emitting Diodes*. Second ed.; Cambridge University Press: 2006.
162. Williams, A. T. R.; Winfield, S. A.; Miller, J. N., Relative fluorescence quantum yields using a computer-controlled luminescence spectrometer. *Analyst* **1983,** *108* (1290), 1067-1071.
163. Kubin, R. F.; Fletcher, A. N., Fluorescence quantum yields of some rhodamine dyes. *Journal of Luminescence* **1982,** *27* (4), 455-462.

164. Lee, J.-S.; Shevchenko, E. V.; Talapin, D. V., Au−PbS Core−Shell Nanocrystals: Plasmonic Absorption Enhancement and Electrical Doping via Intra-particle Charge Transfer. *Journal of the American Chemical Society* **2008,** *130* (30), 9673-9675.
165. Luther, J. M.; Gao, J.; Lloyd, M. T.; Semonin, O. E.; Beard, M. C.; Nozik, A. J., Stability Assessment on a 3% Bilayer PbS/ZnO Quantum Dot Heterojunction Solar Cell. *Advanced Materials* **2010,** *22* (33), 3704-3707.
166. Kershaw, S. V.; Susha, A. S.; Rogach, A. L., Narrow bandgap colloidal metal chalcogenide quantum dots: synthetic methods, heterostructures, assemblies, electronic and infrared optical properties. *Chemical Society Reviews* **2013,** *42* (7), 3033-3087.
167. Mourdikoudis, S.; Liz-Marzán, L. M., Oleylamine in Nanoparticle Synthesis. *Chemistry of Materials* **2013,** *25* (9), 1465-1476.
168. Son, D. H.; Hughes, S. M.; Yin, Y.; Paul Alivisatos, A., Cation Exchange Reactions in Ionic Nanocrystals. *Science* **2004,** *306* (5698), 1009-1012.
169. Wiedemeier, H.; Santandrea, R., Mass spectrometric studies of the Decomposition and the Heat of Formation of CuInS2(s). *Zeitschrift für anorganische und allgemeine Chemie* **1983,** *497* (2), 105-118.
170. Deore, S.; Navrotsky, A., Oxide melt solution calorimetry of sulfides: Enthalpy of formation of sphalerite, galena, greenockite, and hawleyite. *American Mineralogist* **2006,** *91* (2-3), 400-403.
171. Uehara, M.; Watanabe, K.; Tajiri, Y.; Nakamura, H.; Maeda, H., Synthesis of CuInS2 fluorescent nanocrystals and enhancement of fluorescence by controlling crystal defect. *The Journal of Chemical Physics* **2008,** *129* (13), 134709.
172. Thi Kim Chi, T.; Quang Phuong, L.; Quang Liem, N.; Liang, L.; Peter, R., Time-resolved photoluminescence study of CuInS 2 /ZnS nanocrystals. *Advances in Natural Sciences: Nanoscience and Nanotechnology* **2010,** *1* (2), 025007.
173. Nose, K.; Omata, T.; Otsuka-Yao-Matsuo, S., Colloidal Synthesis of Ternary Copper Indium Diselenide Quantum Dots and Their Optical Properties. *The Journal of Physical Chemistry C* **2009,** *113* (9), 3455-3460.
174. Yamamoto, T.; Luck, I. V.; Scheer, R.; Katayama-Yoshida, H., Differences in the electronic structure and compensation mechanism between n-type Zn- and Cd-doped CuInS2 crystals. *Physica B: Condensed Matter* **1999,** *273–274*, 927-929.
175. Zhong, H.; Wang, Z.; Bovero, E.; Lu, Z.; van Veggel, F. C. J. M.; Scholes, G. D., Colloidal CuInSe2 Nanocrystals in the Quantum Confinement Regime: Synthesis, Optical Properties, and Electroluminescence. *The Journal of Physical Chemistry C* **2011,** *115* (25), 12396-12402.
176. Chuang, P.-H.; Lin, C. C.; Liu, R.-S., Emission-Tunable CuInS2/ZnS Quantum Dots: Structure, Optical Properties, and Application in White Light-Emitting Diodes with High Color Rendering Index. *ACS Applied Materials & Interfaces* **2014,** *6* (17), 15379-15387.
177. Vahidshad, Y.; Tahir, M. N.; zad, A. I.; Mirkazemi, S. M.; Ghazemzadeh, R.; Tremel, W., Structural and optical properties of Fe and Zn substituted CuInS2 nanoparticles synthesized by a one-pot facile method. *Journal of Materials Chemistry C* **2015,** *3* (4), 889-898.
178. Ford, G. M.; Guo, Q.; Agrawal, R.; Hillhouse, H. W., CuIn(S,Se)2thin film solar cells from nanocrystal inks: Effect of nanocrystal precursors. *Thin Solid Films* **2011,** *520* (1), 523-528.
179. Zhong, H.; Lo, S. S.; Mirkovic, T.; Li, Y.; Ding, Y.; Li, Y.; Scholes, G. D., Noninjection Gram-Scale Synthesis of Monodisperse Pyramidal CuInS2 Nanocrystals and Their Size-Dependent Properties. *ACS Nano* **2010,** *4* (9), 5253-5262.
180. Ip, A. H.; Thon, S. M.; Hoogland, S.; Voznyy, O.; Zhitomirsky, D.; Debnath, R.; Levina, L.; Rollny, L. R.; Carey, G. H.; Fischer, A.; Kemp, K. W.; Kramer, I. J.; Ning, Z.; Labelle, A. J.; Chou, K. W.; Amassian, A.; Sargent, E. H., Hybrid passivated colloidal quantum dot solids. *Nat Nano* **2012,** *7* (9), 577-582.

181. Tessier, M. D.; Dupont, D.; De Nolf, K.; De Roo, J.; Hens, Z., Economic and Size-Tunable Synthesis of InP/ZnE (E = S, Se) Colloidal Quantum Dots. *Chemistry of Materials* **2015,** *27* (13), 4893-4898.
182. Solubilities of Inorganic and Metal Organic Compounds. Third edition (Seidell, A.). *Journal of Chemical Education* **1941,** *18* (8), 399.
183. R.D.Madan, D., *Modern Inorganic Chemistry*. Third ed.; S. Chand & Company LTD.: New Delhi, 1987.
184. Yarema, O.; Yarema, M.; Bozyigit, D.; Lin, W. M. M.; Wood, V., Independent Composition and Size Control for Highly Luminescent Indium-Rich Silver Indium Selenide Nanocrystals. *ACS Nano* **2015,** *9* (11), 11134-11142.
185. Bai, T.; Li, C.; Li, F.; Zhao, L.; Wang, Z.; Huang, H.; Chen, C.; Han, Y.; Shi, Z.; Feng, S., A simple solution-phase approach to synthesize high quality ternary AgInSe2 and band gap tunable quaternary AgIn(S1-xSex)2 nanocrystals. *Nanoscale* **2014,** *6* (12), 6782-6789.
186. Wang, X.; Xie, C.; Zhong, J.; Liang, X.; Xiang, W., Synthesis and temporal evolution of Zn-doped AgInS2 quantum dots. *Journal of Alloys and Compounds* **2015,** *648*, 127-133.
187. Regulacio, M. D.; Han, M.-Y., Multinary I-III-VI2 and I2-II-IV-VI4 Semiconductor Nanostructures for Photocatalytic Applications. *Accounts of Chemical Research* **2016,** *49* (3), 511-519.
188. Riha, S. C.; Johnson, D. C.; Prieto, A. L., Cu2Se Nanoparticles with Tunable Electronic Properties Due to a Controlled Solid-State Phase Transition Driven by Copper Oxidation and Cationic Conduction. *Journal of the American Chemical Society* **2011,** *133* (5), 1383-1390.
189. Torimoto, T.; Adachi, T.; Okazaki, K.-i.; Sakuraoka, M.; Shibayama, T.; Ohtani, B.; Kudo, A.; Kuwabata, S., Facile Synthesis of ZnS−AgInS2 Solid Solution Nanoparticles for a Color-Adjustable Luminophore. *Journal of the American Chemical Society* **2007,** *129* (41), 12388-12389.
190. Kadlag, K. P.; Rao, M. J.; Nag, A., Ligand-Free, Colloidal, and Luminescent Metal Sulfide Nanocrystals. *The Journal of Physical Chemistry Letters* **2013,** *4* (10), 1676-1681.
191. Chang, J.-Y.; Wang, G.-Q.; Cheng, C.-Y.; Lin, W.-X.; Hsu, J.-C., Strategies for photoluminescence enhancement of AgInS2 quantum dots and their application as bioimaging probes. *Journal of Materials Chemistry* **2012,** *22* (21), 10609-10618.
192. Cui, C.; Li, X.; Liu, J.; Hou, Y.; Zhao, Y.; Zhong, G., Synthesis and Functions of Ag(2)S Nanostructures. *Nanoscale Res Lett* **2015,** *10*, 431.
193. Langevin, M.-A.; Ritcey, A. M.; Allen, C. N., Air-Stable Near-Infrared AgInSe2 Nanocrystals. *ACS Nano* **2014,** *8* (4), 3476-3482.
194. Xiong, Y., Morphological changes in Ag nanocrystals triggered by citrate photoreduction and governed by oxidative etching. *Chemical Communications* **2011,** *47* (5), 1580-1582.
195. Mahapatra, S. S.; Karak, N., Silver nanoparticle in hyperbranched polyamine: Synthesis, characterization and antibacterial activity. *Materials Chemistry and Physics* **2008,** *112* (3), 1114-1119.
196. Seo, J.-S.; Jeon, J.-H.; Hwang, Y. H.; Park, H.; Ryu, M.; Park, S.-H. K.; Bae, B.-S., Solution-Processed Flexible Fluorine-doped Indium Zinc Oxide Thin-Film Transistors Fabricated on Plastic Film at Low Temperature. *Scientific Reports* **2013,** *3*, 2085.
197. Chirico, P.; Hector, A. L., Solvothermal Synthesis of Gallium and Indium Nitrides Using Lithium Amide. *Zeitschrift für Naturforschung B* **2010,** *65* (8), 1051-1057.
198. Zhu, G.; Xu, Z., Controllable Growth of Semiconductor Heterostructures Mediated by Bifunctional Ag2S Nanocrystals as Catalyst or Source-Host. *Journal of the American Chemical Society* **2011,** *133* (1), 148-157.
199. Torimoto, T.; Tada, M.; Dai, M.; Kameyama, T.; Suzuki, S.; Kuwabata, S., Tunable Photoelectrochemical Properties of Chalcopyrite AgInS2 Nanoparticles Size-Controlled with a Photoetching Technique. *The Journal of Physical Chemistry C* **2012,** *116* (41), 21895-21902.

200. Yao, D.; Liu, H.; Liu, Y.; Dong, C.; Zhang, K.; Sheng, Y.; Cui, J.; Zhang, H.; Yang, B., Phosphine-free synthesis of Ag-In-Se alloy nanocrystals with visible emissions. *Nanoscale* **2015,** *7* (44), 18570-18578.
201. Wang, D.; Xie, T.; Peng, Q.; Li, Y., Ag, Ag2S, and Ag2Se Nanocrystals: Synthesis, Assembly, and Construction of Mesoporous Structures. *Journal of the American Chemical Society* **2008,** *130* (12), 4016-4022.
202. Chung, W.; Jung, H.; Lee, C. H.; Kim, S. H., Extremely high color rendering white light from surface passivated carbon dots and Zn-doped AgInS2 nanocrystals. *Journal of Materials Chemistry C* **2014,** *2* (21), 4227-4232.
203. Ruan, C.; Zhang, Y.; Lu, M.; Ji, C.; Sun, C.; Chen, X.; Chen, H.; Colvin, V.; Yu, W., White Light-Emitting Diodes Based on AgInS2/ZnS Quantum Dots with Improved Bandwidth in Visible Light Communication. *Nanomaterials* **2016,** *6* (1), 13.
204. Wang, C.; Wang, Y.; Xu, L.; Zhang, D.; Liu, M.; Li, X.; Sun, H.; Lin, Q.; Yang, B., Facile Aqueous-Phase Synthesis of Biocompatible and Fluorescent Ag2S Nanoclusters for Bioimaging: Tunable Photoluminescence from Red to Near Infrared. *Small* **2012,** *8* (20), 3137-3142.
205. Chevallier, T.; Le Blevennec, G.; Chandezon, F., Photoluminescence properties of AgInS2-ZnS nanocrystals: the critical role of the surface. *Nanoscale* **2016,** *8* (14), 7612-7620.
206. Xiang, W.; Xie, C.; Wang, J.; Zhong, J.; Liang, X.; Yang, H.; Luo, L.; Chen, Z., Studies on highly luminescent AgInS2 and Ag–Zn–In–S quantum dots. *Journal of Alloys and Compounds* **2014,** *588*, 114-121.
207. Dienel, T.; Bauer, C.; Dolamic, I.; Brühwiler, D., Spectral-based analysis of thin film luminescent solar concentrators. *Solar Energy* **2010,** *84* (8), 1366-1369.
208. Romanowski, P. http://chemistscorner.com/cosmetic-formulation-basics-nail-polish/.
209. Kambour, R. P., A review of crazing and fracture in thermoplastics. *Journal of Polymer Science: Macromolecular Reviews* **1973,** *7* (1), 1-154.
210. Alkhayatt, A. H. O.; Al-Azzawi, A. H.; Alakayashi, Z., Rheological and optical characterization of Polyvinylpyrrolidone (PVP)-Polyethylene glycol (PEG) polymer blends.
211. Meinardi, F.; McDaniel, H.; Carulli, F.; Colombo, A.; Velizhanin, K. A.; Makarov, N. S.; Simonutti, R.; Klimov, V. I.; Brovelli, S., Highly efficient large-area colourless luminescent solar concentrators using heavy-metal-free colloidal quantum dots. *Nature nanotechnology* **2015**.